Brownian particle transport in periodic structures

Dissertation

vorgelegt von

Alexander Antonov

Eingereicht im Juni 2023
am Fachbereich Mathematik/Informatik/Physik
zur Erlangung des akademischen Grades
Doktor der Naturwissenschaften
– Dr. rer. nat. –

Gutachter: Prof. Dr. Philipp Maaß
Zweitgutachter: RNDr. Artem Ryabov, Ph.D.

Abstract

Particle transport in both natural and fabricated systems often takes place in confined geometries under single-file conditions. This means, that particles cannot pass each other, as, for example, when the particles move through membrane pores or microfluidic channels. A generic model describing particle dynamics in such systems is the Brownian asymmetric simple exclusion process (BASEP). It describes the driven Brownian particle motion of hard spheres through a periodic structure under a constant drag force. This model has been introduced as Brownian dynamics variant of the asymmetric simple exclusion process (ASEP), which is a discrete lattice model that has been established to study fundamental aspects of nonequilibrium physics.

Current-density relations in the BASEP are characterized by three effects: a barrier reduction effect, a blocking effect and a commensurability effect. These effects dominate the dynamics for certain range of particle diameters: the barrier reduction effect dominates when it is likely that a potential well is occupied by more than one particle. The blocking effect prevails when the particle diameter becomes large such that the multiple occupation of a potential well becomes unlikely due to steric reasons. The commensurability effect governs the dynamics when the particle diameter is close to the spatial period of the external structure.

One part of this thesis is devoted to the investigation to what extent and how these effects are modified when considering particles with a soft core that can partially penetrate or even pass each other. We develop an effective size method by which the system of soft particles is mapped to that of the BASEP. This effective size method is well suitable to describe the dynamics of partially penetrating particles.

In the main part of the thesis, particle transport in the BASEP is studied with a focus on crowding effects appearing at high densities. The investigation involves both analytical derivations and extensive Brownian dynamics simulations, including the development of novel algorithms.

One intriguing crowding effect is the of solitary cluster waves that propagate without dispersion. At low temperatures, these solitons generate measurable particle currents for certain particle diameters even if potential barriers are hundred times larger than

the thermal energy. In effectively frustrated systems, where the blocking effect typically inhibits particle motion, solitons can result in high particle currents. The presence of these theoretically predicted solitons has been experimentally verified recently in colloidal particle transport.

Zusammenfassung

Häufig findet Teilchentransport in natürlichen und künstlich hergestellten Systemen in begrenzten Geometrien unter Single-File-Bedingungen statt. Unter solchen Bedingungen können sich überholen, d.h. sie behalten ihre Reihenfolge wenn sie sich z. B. durch Membranporen oder mikrofluidische Kanäle bewegen. Ein generelles Modell, das die Teilchendynamik in solchen Systemen beschreibt, ist der "Brownian Asymmetric Simple Exclusion Process" (BASEP). Er beschreibt die getriebene Brownsche Teilchenbewegung harter Kugeln durch eine periodische Struktur unter einer konstanten Triebkraft. Dieses Modell wurde als Brownsche-Dynamik-Variante des "Asymmetric Simple Exclusion Process" (ASEP) eingeführt, wobei der ASEP ein diskretes Gittermodell ist, das zur Untersuchung grundlegender Aspekte der Nichtgleichgewichtsphysik entwickelt wurde.

Strom-Dichte-Relationen im BASEP werden durch drei Effekte charakterisiert: einem Barriererenreduktionseffekt, einem Blockierseffekt und einem Kommensurabilitätseffekt. Diese Effekte dominieren das dynamische Verhalten in bestimmten Bereichen von Teilchendurchmessern. Der Barriererenreduktionseffekt ist vorherrschend, wenn es wahrscheinlich ist, dass ein Potentialtopf von mehr als einem Teilchen besetzt ist, der Blockierseffekt dominiert, wenn der Teilchendurchmesser die Mehrfachbesetzung eines Potentialtopfes aus sterischen Gründen behindert, und der Kommensurabilitätseffekt ist entscheidend, wenn der Teilchendurchmesser vergleichbar mit der Wellenlänge der periodischen Struktur wird.

Ein Teil dieser Arbeit ist der Untersuchung gewidmet, in welchem Maße diese Effekte auftreten bzw. modifiziert werden, wenn weiche Teilchen betrachtet werden, die sich teilweise durchdringen oder sich sogar überholen können. Durch Entwicklung eines neuen Verfahren, der Methode effektiver Teilchengröße, lässt sich das System weicher Teilchen auf den BASEP abbilden. Diese Methode effektiver Teilchengröße ist sehr gut geeignet, um die Dynamik sich teilweise durchdringender Teilchen zu beschreiben.

Im Hauptteil dieser Arbeit wird der Teilchentransport im BASEP untersucht, wobei der Schwerpunkt auf Vielteilcheneffekten liegt, die bei sehr hohen Teilchendichten auftreten. Diese Untersuchungen beinhalten sowohl analytische Herleitungen als auch umfangreiche Brownsche-Dynamik-Simulationen, einschließlich der Entwicklung neuer Algorithmen.

Ein faszinierender Effekt ist die Bildung von Wellen aus Teilchenclustern, die sich ohne Dispersion ausbreiten. Bei niedrigen Temperaturen induzieren diese Solitonen messbare Teilchenströme bei bestimmten Teilchendurchmessern selbst dann, wenn die Potentialbarrieren hundert Mal größer sind als die thermische Energie. In frustrierten Systemen, in denen der Blockierseffekt die Teilchenbewegung im Allgemeinen hemmt, können Solitonen zu erheblichen Teilchenströmen führen. Das Auftreten von Solitonen wurde vor kurzem beim Transports kolloidaler Teilchen experimentell nachgewiesen.

Contents

List of frequently used symbols and abbreviations

Symbol	Meaning	Important relations
x	position	
v	velocity	
j	current	
t	time	
f	force	
μ	particle mobility	
$k_\mathrm{B}T$	thermal energy	
β	inverse thermal energy	$\beta = \dfrac{1}{k_\mathrm{B}T}$
D	diffusion coefficient	$D = \mu k_\mathrm{B}T$
λ	wavelength	
U_0	potential barrier	
$U(x)$	external potential	$U(x) = \dfrac{U_0}{2}\cos\left(\dfrac{2\pi x}{\lambda}\right)$
$f - U'(x)$	external force	
v_0	velocity of independent particles	
j_st	stationary current in the steady-state	
L	system length	$L = m\lambda,\ m \in \mathbb{N}$
N	particle number	$N - \dfrac{L}{\lambda}$ is system overcrowding
ς	particle size	
σ	normalized particle size	$\sigma = \varsigma/\lambda$
$\varrho(x)$	particle density	$\displaystyle\int_0^\lambda \mathrm{d}y\varrho(y) = N/L$
$\bar{\varrho}$	mean particle number density	$\bar{\varrho} = N/L$
$\rho(x)$	normalized particle density	$\rho(x) = \lambda\varrho(x)$
$\bar{\rho}$	filling factor	$\bar{\rho} = \bar{\varrho}\lambda$
$\eta(x)$		$\eta(x) = \displaystyle\int_{x-\varsigma}^{x} \mathrm{d}y\varrho(y)$

Symbol	Meaning	Important relations
$\varrho^{(2)}(x,y)$	two particle density	
ρ	cluster density	
$f^{\mathrm{int}}(x)$	mean interaction force at position x	
r	particles distance	
ε	dimensionless softness parameter	
V_0	amplitude of the interaction potential	
$V(r)$	interaction potential of soft particles	$\frac{V_0}{\varepsilon[1+\mathrm{erf}(\varsigma/\sqrt{2}\lambda\varepsilon)]}\,\mathrm{erfc}\left(\frac{r-\varsigma}{\sqrt{2}\lambda\varepsilon}\right)$
f_i^{int}	total interaction force acting on particle i	
n	cluster/soliton size	
k	order of transition state for thermally activated cluster	$k=\lfloor n/2 \rfloor$

Abbreviation	Meaning
ASEP	**A**symmetric **S**imple **E**xclusion **P**rocess
BASEP	**B**rownian **A**symmetric **S**imple **E**xclusion **P**rocess
AZMIF	**A**pproximation of the **Z**ero **M**ean **I**nteraction **F**orce
DDFT	**D**ynamic **D**ensity **F**unctional **T**heory

1 Introduction

1.1 Driven transport in narrow channels

Brownian motion, named after Scottish botanist Robert Brown who first described the phenomenon in 1827, is the random motion of particles suspended in a fluid (a liquid or a gas). It results from their collision with the fast-moving atoms or molecules in the fluid. The theory of Brownian motion has substantial practical significance in many areas of modern physics. In real systems, such motion is often spatially confined, while the nature of the confining environment, such as the walls of the channel or an external magnetic field, can be of a different kind. As some of many examples, Brownian motion is used in describing various aspects of DNA (deoxyribonucleic acid) dynamics [1–3], dynamics of colloidal suspensions [4, 5], or association of proteins [6, 7]. Brownian motion is also applied in economics, for describing financial markets [8] or in game theory [9–11], in biology, for various models of biological aggregation [12, 13], and in many other disciplines.

In this thesis we focus on Brownian motion of particles in narrow channels, where the channel has a diameter almost equal to the particle size, so that particles cannot pass each other (*single-file diffusion*). Describing properties of the Brownian transport inside such channels is not only a fundamental scientific problem, but also a challenge in various applications which were particularly motivated by the recent advances in nanotechnology, like diffusion in zeolites (that is important for catalysis) [14–16], inside nanotubes [17], and ion diffusion [18]. Other interesting examples of single-file transport include motion of motor proteins along microtubules or actin tracks [19, 20], and protein synthesis by ribosomes [21]. Single-file motion has been reported in conjection with bioadsorption and biocatalysis in mesoporous materials [22, 23], in carbon nanotubes with relevance to biotechnological and biomedical applications [24], in nanofluidic devices [25], which can be utilized for water ultrafiltration or osmotic energy conversion. Transport in narrow channels can be relevant also for industrial problems, like filtration and desalting [26], pedestrian and car traffic [27, 28].

For the study of collective single-file particle dynamics, there is a prominent reference lattice model, the asymmetric simple exclusion process (ASEP). In this model, particles

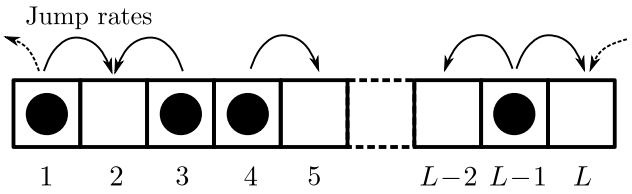

Figure 1.1: Illustration of the ASEP. The arrows indicate directions in which the particle jumps can occur. These jumps occur between nearest-neighbor lattice sites with certain rates. Jumps to occupied lattice sites are forbidden, i.e. a lattice site can be occupied by at most one particle. The bias in the system is set by the difference between the jumps rates to the left and right. Dashed arrows between sites 0 and L correspond to a jump between these sites in case of periodic boundary condition. They correspond to adding or removing particles in case of an open system.

with exclusion interaction are considered to jump between neighboring sites of a one-dimensional lattice with a bias in one direction, see illustration in Fig. 1.1.

Several significant findings have been reported in relation to the ASEP. The model itself was first designed to describe protein production by ribosomes [21]. Subsequently, the field of applications of the ASEP was substantially expanded, including the modeling of biological traffic [29, 30], studies of molecular motor motion [31–33], and analysis of multiplex networks [34]. In terms of theoretical advances, exact results for microstate distributions in nonequilibrium steady states were obtained [35]. Furthermore, investigations into systems with random hopping rates revealed condensation transitions [36, 37]. The ASEP also exhibited phase transitions in the bulk density for systems with open boundaries [38, 39]. Additionally, rate functions were found to possess singular points characterizing large deviations of fluctuations in time-averaged currents [40–42]. Studying variants of the ASEP in the hydrodynamic limit led to the discovery of new universality classes of nonlinear hydrodynamics [43]. Moreover, concrete microscopic models were used to validate predictions of nonlinear fluctuating hydrodynamics [44].

1.2 The Brownian asymmetric simple exclusion process (BASEP)

Despite the aforementioned successes, the ASEP and its coarse-grained modifications are not deprived of disadvantages, the most fundamental one being its discreteness when applied to processes in continuum space. An extension of the ASEP, the Brownian asymmetric simple exclusion process, or BASEP, was suggested as a reference model to study

the properties of the single-file transport in continuum space. In this process, hard spheres are driven through a periodic potential by a constant drag force. The motivation for periodicity of potential is that the confining environment in single-file diffusion usually has a periodic structure, which in a theoretical modeling is most easily accounted for by an external periodic potential. The periodicity of the confining environment can be of steric reasons, e.g. due to variation in a pore cross section [45–47], or of energetic nature, e.g. when associated with the periodic structure of binding sites along a membrane channel [48–50].

Over the last decade, microfluidics and optical and/or magnetic micromanipulation techniques, pioneered significantly by Ashkin and his colleagues [51–55], were intensively developed [56–63]. These techniques are actively used e.g. in rheology [64, 65] to perform measurements, in neuroscience for studying molecular or neuronian dynamics [66, 67], or in biology to stretch DNA [68, 69]. The manipulation capabilities include the ability to trap multiple particles [70] or soft particles at interfaces [71, 72] and to drag them [73]. These abilities of manipulation techniques make it possible to study the BASEP [74, 75] and similar setups of collective motion of colloidal particles in spatial confinement experimentally [76–78].

As for applications, the BASEP is relevant, e.g. for the description of transport through channels with binding sites in biology [79–81] for transport of colloidal particles [82], and in thermodynamics of microscopic heat engines [83, 84].

Previously, various key aspects of the BASEP were thoroughly studied in Refs. [85–87]. Many effects that emerge in the BASEP have no counterparts in corresponding discrete systems. For illustration of these effects the current-density relations, also known as "fundamental diagrams" [29], are used. Different current regimes occurring in an open system that is coupled to particle reservoirs, and in a closed system that is not coupled to particle reservoirs, have also been discovered and described in detail. While the BASEP focuses on investigating hardcore interactions, it is important to note that real-world systems encompass a broader range of interaction types that extend beyond this limit. Nevertheless, it is reasonable to anticipate that significant qualitative changes would arise only from the interaction of soft particles that can partially penetrate or even pass each other, or from sticky particle interactions that could result in particle clustering. Regarding stickiness, ongoing studies of Baxter's model of adhesive particles [88] have yielded promising results, including the development of algorithm for Brownian dynamics simulations [89], as well as the formulation of a scaling theory for the time-dependent mean squared displacement of a tagged particle [90]. The dynamics of soft particles has been investigated in [91], and it is also highlighted and developed in the present thesis.

This thesis holds its main merit in investigating particle transport in the BASEP, with a particular emphasis on the impact of crowding effects that arise at high densities. In biology, these crowding effects have a significant influence, impacting various aspects such as protein folding and aggregation [92, 93], protein stability [94–96], enzyme activity [97–99], DNA and DNA-protein interactions [100, 101], polymer [102] and DNA [103] translocation. In the discrete ASEP, the phenomenon of crowding is examined by introducing local inhomogeneities or defects [104, 105], typically arising from specific particle interactions [106, 107]. However, in the proposed continuous BASEP framework, the crowding setup is more inherent. Notably, the BASEP has theoretically predicted the existence of *Brownian solitons*, which have subsequently been confirmed in experiments involving colloidal particles controlled by optical tweezers [108]. The approaches developed in this work are applicable to a broad range of problems in theoretical physics, such as Kramers problem [109] or density functional theory [110].

1.3 Thesis organization

This thesis consists of two parts and is organized as follows. The first part is dedicated to analyzing theoretical and numerical results. In Chapter 2 we formally introduce the BASEP and derive its main properties. This chapter is an introductory overview revealing the basic essence of the fundamental issues discussed in the following chapters. In Chapter 3 we introduce a term *Brownian soliton*, representing a novel theoretical prediction. It stands for a collective phenomenon when particles in the BASEP propagate as *clusters*, with a propagation velocity much higher than the velocity of independent particles even in a flat potential. These solitons can occur either due to thermal fluctuations (Sec. 3.2) or due to system overpopulation (Sec. 3.3). In Chapter 4 we investigate how the ability of particles to penetrate and pass each other affects the collective transport properties considered in Chapter 2 for the BASEP. In order to model such system, we modify the hardcore interaction potential, thereby making mutual penetration and crossing of particles possible.

The second part of the thesis is devoted to computational methods. In Chapter 5 we present a review of approaches for Brownian dynamics simulations and describe algorithms implemented in this thesis. A brief summarizing Chapter 6 concludes the thesis.

The values of quantities presented in the figures of this thesis are expressed in dimensionless units. In the Appendix, we provide the units of the quantities.

The parameters of computer simulations used in a particular chapter/section are set at its beginning, unless otherwise specified. A brief conclusion for each chapter and a

short discussion of open scientific problems related to the topic of the chapter are given in summary notes.

2 Basics of the BASEP

This chapter presents a description of the BASEP and its general results which provides a theoretical basis for the further developments in the present thesis. The chapter is based on the first studies of the BASEP [85, 86]. It contains also additional information about previously unrevealed aspects as well as a detailed description of certain aspects of the original studies.

2.1 Model

The BASEP is a Brownian motion of N particles with particle diameter ς that interact via hardcore exclusion. In what follows, we refer to the particle diameter as the *particle size*, and to particles interacting via hardcore exclusion interaction as *hard rods* or *hard particles*. In this thesis, we focus on a closed BASEP, where periodic boundary conditions are applied and the particle number remains the same. The details of open systems, where particles can be added or removed via particle reservoirs, were investigated in Refs. [85, 86].

The Brownian motion is described by a set of Langevin equations,

$$\frac{\mathrm{d}x_i}{\mathrm{d}t} = \mu\left(f - U'(x_i)\right) + \sqrt{2D}\xi_i(t),\ i = 1, \ldots, N, \tag{2.1}$$

where μ is the particle mobility, f is the constant drag force, $D = k_\mathrm{B}T\mu$ is the diffusion coefficient with $k_\mathrm{B}T$ the thermal energy, $\xi_i(t)$ are Gaussian white noise processes with zero mean and correlations $\langle \xi_i(t)\xi_j(t')\rangle = \delta_{ij}\delta(t-t')$. The system length L is an integer multiple of λ and periodic boundary conditions are applied. To address these conditions, we introduce two mirror particles associated with the last particle ($i = N$) and the first particle ($i = 1$) in the system. These mirror particles are assigned indices 0 and $(N+1)$, respectively, and have coordinates:

$$x_0 = x_N - L, \tag{2.2a}$$

$$x_{N+1} = x_1 + L. \tag{2.2b}$$

The particle interactions are taken into account by a hardcore exclusion constraint between neighboring particles,

$$|x_{i+1} - x_i| \geq \varsigma, \tag{2.3}$$

and

$$U(x) = \frac{U_0}{2} \cos\left(\frac{2\pi x}{\lambda}\right) \tag{2.4}$$

is the external periodic potential with potential barriers U_0 between neighboring wells separated by the wavelength λ. In the study [87] it was shown that results obtained for this specific potential are generic with respect to the current-density characteristics, so in what follows we focus on considering the external potential (2.4). In Eq. (2.1), $U'(.)$ denotes the space derivative of the external potential, so that $f - U'(x)$ is the external force that is implied on a particle at the position x. A visual illustration of the introduced process is given in Fig. 2.1. In the present thesis we focus on the undercritical regime, i.e. the tilted potential $U(x) - fx$ has extrema points. That implies the condition that the equation

$$f - U'(x) = f - \frac{\pi U_0}{\lambda} \sin\left(\frac{2\pi x}{\lambda}\right) = 0, \; x \in \mathbb{R}, \tag{2.5}$$

has a solution, leading to the following requirement for the drag force:

$$f \leq \frac{\pi U_0}{\lambda}. \tag{2.6}$$

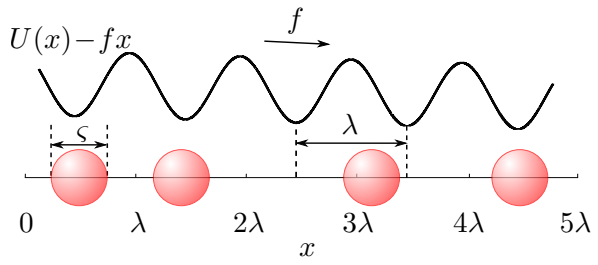

Figure 2.1: Illustration of the BASEP. Hardcore interacting particles of size ς are driven by a constant drag force f through a periodic potential $U(x)$ with amplitude $U_0 \gg k_B T$ and periodicity λ. The average slope of the tilted potential $U(x) - fx$ corresponds to the magnitude of the drag force f.

In the following, we always consider the drag force f to be directed from left to right, in the direction of the coordinate axis x.

2.2 General results

Since the number of particles remains constant, the corresponding conservation law can be taken into account via the continuity equation [111]

$$\frac{\partial \varrho(x,t)}{\partial t} + \frac{\partial j(x,t)}{\partial x} = 0, \tag{2.7}$$

where $j(x,t)$ is the particle current, and

$$\varrho(x,t) = \left\langle \sum_{i=1}^{N} \delta(x - x_i(t)) \right\rangle \tag{2.8}$$

is the local density, $\langle \ldots \rangle$ is the ensemble average, which corresponds to the mean value of the measured quantity according to the distribution of the system on its microstates in the ensemble [112]. This average is evaluated at time instant t for a given initial condition. The ensemble is represented by a density function $\varrho(x,t)$ which evolves in time according to the Langevin equations (2.1) and the given initial conditions. A practical application of Eq. (2.8) assuming the ergodic hypothesis, which states that the average of a process parameter over time is equal to the average over the statistical ensemble [113], is given in Chapter 5.

The Langevin equations (2.1) combined with the continuity equation can be written as the many-body Smoluchowski equation, which directly describes the time evolution of the density function [85, 114]:

$$\frac{\partial \varrho(x,t)}{\partial t} = -\frac{\partial j(x,t)}{\partial x},$$

with

$$j(x,t) = \mu \left(f - U'(x) + f^{\mathrm{int}}(x,t) \right) \varrho(x,t) - D \frac{\partial \varrho(x,t)}{\partial x}, \tag{2.9a}$$

where $f^{\mathrm{int}}(x,t)$ is the mean interaction force due to hardcore interactions at position x at time t. It can be written via the two-particle density

$$\varrho^{(2)}(x,y,t) = \left\langle \sum_{i=1}^{N} \sum_{j=1}^{N} \delta(x - x_i(t)) \delta(y - y_j(t)) \right\rangle, \tag{2.10}$$

as

$$f^{\mathrm{int}}(x,t) = \frac{1}{\varrho(x,t)} \int_0^L \mathrm{d}y\, f^{(2)}(x,y)\varrho^{(2)}(x,y,t), \tag{2.11}$$

where $f^{(2)}(x,y)$ is the pair interaction force of particle at position y on particle at position x. For the system of hard rods, the mean interaction force reads [85]

$$f^{\mathrm{int}}(x,t) = k_{\mathrm{B}}T \frac{\varrho^{(2)}(x,x-\varsigma,t) - \varrho^{(2)}(x,x+\varsigma,t)}{\varrho(x,t)}. \tag{2.12}$$

Relation (2.12) can be derived from the following heuristic considerations: for hard-interacting particles, the interaction force is infinite when the distance r between them approaches ς from below (which effectively means that particles cannot penetrate each other, so that hardcore exclusion constraint (2.3) is satisfied), and zero otherwise. Thus, we can present the pair interaction force in the following way:

$$\begin{aligned} f^{(2)}(x,y) &= \lim_{r\to\varsigma^-} \Big(k_{\mathrm{B}}T[\delta(y-(x-r)) - \delta(y-(x+r))] \Big) \\ &= k_{\mathrm{B}}T[\delta(y-(x-\varsigma)) - \delta(y-(x+\varsigma))], \end{aligned} \tag{2.13}$$

with $k_{\mathrm{B}}T$ as the only relevant energy scale due to dimensional reasons. By substituting it into (2.11), we obtain the relation (2.12).

2.2.1 Equilibrium properties

Before describing the nonequilibrium dynamics ($f \neq 0$), we first derive the equilibrium properties ($f = 0$). For hard rods in one dimension the exact functional of the density profile was derived by Percus [115],

$$\Omega[\varrho(x)] = \int_0^\lambda \mathrm{d}x \varrho(x) \left\{ U(x) - \mu_{\mathrm{ch}} - k_{\mathrm{B}}T \left(1 - \ln \left[\frac{\varrho(x)}{1-\eta(x)} \right] \right) \right\}, \tag{2.14}$$

where μ_{ch} is the chemical potential and

$$\eta(x) = \int_{x-\varsigma}^{x} \mathrm{d}y\, \varrho(y). \tag{2.15}$$

Equation (2.14) is given for the grand canonical ensemble which is not the case in the BASEP, where the ensemble is canonical. However, these two ensembles are equivalent in the thermodynamic limit, and the differences between their density profiles are usually

negligible for $N \gtrsim 100$ [116]. The specific conditions when we cannot assume the density profiles of these ensembles to be equivalent are given in the summary notes in Sec. 2.4 of this chapter.

To get the equilibrium density profile, we minimize the functional (2.14):

$$\frac{\delta\Omega[\varrho]}{\delta\varrho}\Big|_{\varrho=\varrho_{\mathrm{eq}}} = 0. \tag{2.16}$$

To calculate the functional derivative, we use product and chain rules [117]:

$$\begin{aligned}\frac{\delta\Omega[\varrho(x)]}{\delta\varrho(y)} \quad &= \\ = \; U(y) - \mu_{\mathrm{ch}} - k_{\mathrm{B}}T\left(1 - \ln\left[\frac{\varrho(y)}{1-\eta(y)}\right]\right) &+ k_{\mathrm{B}}T\left(1 + \int_0^\lambda \mathrm{d}x \frac{\delta\eta[\varrho(x)]}{\delta\varrho(y)}\frac{\varrho(x)}{1-\eta(x)}\right).\end{aligned} \tag{2.17}$$

Direct calculation gives us

$$\begin{aligned}\int_0^\lambda \mathrm{d}x \frac{\delta\eta[\varrho(x)]}{\delta\varrho(y)}\frac{\varrho(x)}{1-\eta(x)} &= \int_0^\lambda \mathrm{d}x \frac{\varrho(x)}{1-\eta(x)}\int_{x-\varsigma}^{x}\mathrm{d}z\delta(y-z) \\ &= \int_0^\lambda \mathrm{d}x \frac{\varrho(x)}{1-\eta(x)}\Theta\left([y-x][\varsigma+x-y]\right) = \int_y^{y+\varsigma}\mathrm{d}x\frac{\varrho(x)}{1-\eta(x)}.\end{aligned} \tag{2.18}$$

Combining (2.16), (2.17), (2.18) and taking $y = x$, we obtain the relation determining equation for the equilibrium density profile:

$$\frac{\delta\Omega[\varrho]}{\delta\varrho}\Big|_{\varrho=\varrho_{\mathrm{eq}}} = U(x) - \mu_{\mathrm{ch}} + k_{\mathrm{B}}T\left(\ln\left[\frac{\varrho_{\mathrm{eq}}(x)}{1-\eta_{\mathrm{eq}}(x)}\right] + \int_x^{x+\varsigma}\mathrm{d}y\frac{\varrho_{\mathrm{eq}}(y)}{1-\eta_{\mathrm{eq}}(y)}\right) = 0. \tag{2.19}$$

Here the chemical potential μ_{ch} is set implicitly by the normalization condition

$$\frac{1}{\lambda}\int_0^\lambda \varrho(x)\mathrm{d}x = \bar{\varrho}, \tag{2.20}$$

with the density $\bar{\varrho}$ defined as the mean particle number density, $\bar{\varrho} = N/L$.

For numerical calculation of ϱ_{eq}, we use the evolution equation for density profile in dynamical density functional theory. For one-dimensional system it reads [118, 119]:

$$\frac{\partial\varrho(x,t)}{\partial t} = \mu\frac{\partial}{\partial x}\left(\varrho(x,t)\frac{\partial}{\partial x}\frac{\delta\Omega[\varrho(x,t)]}{\delta\varrho(x,t)}\right). \tag{2.21}$$

Equation (2.21) can be used for a minimization procedure of the static density functional (2.14), since its stationary solution satisfies the minimization condition (2.16) in correspondence with the normalization condition (2.20) [120, 121]. Thus, evolving an initial density profile with Eq. (2.21) until the stationary one is obtained provides us with the equilibrium density profile. We have taken the Boltzmann distribution $\varrho(x) \propto \exp(-U(x)/k_\mathrm{B}T)$ with a normalization condition (2.20) as the initial profile.

In addition, the evolution equation also allows us to obtain an expression for the two-particle density at contact. Inserting (2.19) into (2.21) gives

$$\begin{aligned}\frac{\partial\varrho(x,t)}{\partial t} &= \mu\frac{\partial}{\partial x}\Big(\varrho(x,t)\Big[U'(x) + k_\mathrm{B}T\Big(\frac{\partial\varrho(x,t)}{\partial x}\frac{1}{\varrho(x,t)} - \frac{\varrho(x,t)-\varrho(x-\varsigma,t)}{1-\eta(x,t)} \\ &\qquad + \frac{\varrho(x+\varsigma,t)}{1-\eta(x+\varsigma,t)} - \frac{\varrho(x,t)}{1-\eta(x,t)}\Big)\Big]\Big) \\ &= \frac{\partial}{\partial x}\Big[\mu\Big(U'(x) + \frac{k_\mathrm{B}T}{\varrho(x,t)}\Big\{\frac{\varrho(x+\varsigma,t)}{1-\eta(x+\varsigma,t)} - \frac{\varrho(x-\varsigma,t)}{1-\eta(x,t)}\Big\}\Big)\varrho(x,t) + D\frac{\partial\varrho(x,t)}{\partial x}\Big],\end{aligned} \tag{2.22}$$

and inserting (2.12) into (2.9a) for the equilibrium case gives

$$\begin{aligned}&\frac{\partial\varrho(x,t)}{\partial t} = \\ &\quad = \frac{\partial}{\partial x}\Big[\mu\Big(U'(x) + k_\mathrm{B}T\frac{\varrho^{(2)}(x,x-\varsigma,t) - \varrho^{(2)}(x,x+\varsigma,t)}{\varrho(x,t)}\Big)\varrho(x,t) + D\frac{\partial\varrho(x,t)}{\partial x}\Big].\end{aligned} \tag{2.23}$$

Comparing Eqs. (2.22) and (2.23), we would get an expression for the two-particle density at contact:

$$\varrho^{(2)}(x,x+\varsigma) = \frac{\varrho(x)\varrho(x+\varsigma)}{1-\eta(x+\varsigma)}. \tag{2.24}$$

The expression (2.24) has been proven exactly in Ref. [122].

2.2.2 Collective dynamics

Now we consider the case $f \neq 0$, so that the system is out of equilibrium. In the stationary (steady) state, the density profile and the mean interaction force are time-independent, $\varrho(x,t) = \varrho(x)$, $f^\mathrm{int}(x,t) = f^\mathrm{int}(x)$, and the current is both time-independent and homogeneous, $j(x,t) = j_\mathrm{st}$. Eq. (2.9a) then reads

$$j_{\mathrm{st}} = \mu(f - U'(x) + f^{\mathrm{int}}(x))\varrho(x) - D\frac{\partial \varrho(x)}{\partial x}. \tag{2.25}$$

To describe the collective properties of the BASEP, we present a comprehensive analysis of the current dependence on both particle size and mean density. Since these parameters are in units of length and inverse length, respectively, for convenience we introduce their dimensionless analogues:

$$\sigma = \varsigma/\lambda, \tag{2.26a}$$

$$\bar{\rho} = \bar{\varrho}\lambda, \tag{2.26b}$$

$$\rho(x) = \varrho(x)\lambda. \tag{2.26c}$$

The parameter $\bar{\rho} = N\lambda/L$ is thus the filling factor, i.e. the mean number of particles per potential well.

We start the investigation of collective dynamics from the analysis of non-interacting particles ($f^{\mathrm{int}} = 0$). In such a system, the current does not depend on particle size and increases linearly with $\bar{\varrho}$ [111],

$$j_{\mathrm{st}} = v_0\bar{\varrho} = \frac{v_0\bar{\rho}}{\lambda}. \tag{2.27}$$

The mean velocity of a single particle v_0 can be calculated analytically by analyzing the stationary equation (2.25) for a single particle without interaction forces in one period $[0; \lambda]$,

$$v_0 = \mu\left(f - U'(x)\right)\rho(x) - D\frac{\partial \rho(x)}{\partial x}. \tag{2.28}$$

Multiplying it by $e^{-\beta(fx-U(x))}$, with $\beta = 1/(k_{\mathrm{B}}T)$,

$$\begin{aligned} v_0 e^{-\beta(fx-U(x))} &= \mu\rho(x)\left(f - U'(x)\right)e^{-\beta(fx-U(x))} - D\frac{\partial \rho(x)}{\partial x}e^{-\beta(fx-U(x))} \\ &= -D\frac{\partial}{\partial x}\left[\rho(x)e^{-\beta(fx-U(x))}\right], \end{aligned} \tag{2.29}$$

and integrating both sides of the equation (2.29) from 0 to y,

$$v_0\int_0^y e^{-\beta(fx-U(x))}\mathrm{d}x = -D\rho(y)e^{-\beta(fy-U(y))} + D\rho(0)e^{\beta U(0)}, \tag{2.30}$$

we obtain the solution for $\rho(x)$:

$$\rho(x) = \left[-\frac{v_0}{D}\mathcal{G}(x) + \rho(0)e^{\beta U(0)} \right] e^{\beta(fx - U(x))}, \tag{2.31}$$

where we have introduced the function $\mathcal{G}(x) = \int_0^x e^{-\beta(fy-U(y))}\mathrm{d}y$. The term $\rho(0)$ is set by the normalization condition (2.20), with $\bar{\rho} = 1$ for a single particle,

$$\lambda = -\frac{v_0}{D}\int_0^\lambda \mathcal{G}(x)e^{\beta(fx-U(x))}\mathrm{d}x + \rho(0)e^{\beta U(0)}\int_0^\lambda e^{\beta(fx-U(x))}\mathrm{d}x \tag{2.32}$$

The λ-periodicity of the external force $f - U'(x)$ implies that the stationary solution of Eq. (2.25) is λ-periodic as well. By applying this periodic boundary condition to Eq. (2.32),

$$\begin{aligned} \rho(0) &= \rho(\lambda) = \left[-\frac{v_0}{D}\mathcal{G}(\lambda) + \rho(0)e^{\beta U(0)} \right] e^{\beta(f\lambda - U(\lambda))} \\ &= \frac{v_0\mathcal{G}(\lambda)e^{\beta(f\lambda-U(\lambda))}}{D\left(e^{\beta f\lambda} - 1\right)} = \frac{\lambda + \frac{v_0}{D}\int_0^\lambda \mathcal{G}(x)e^{\beta(fx-U(x))}\mathrm{d}x}{e^{\beta U(0)}\int_0^\lambda e^{\beta(fx-U(x))}\mathrm{d}x}, \end{aligned} \tag{2.33}$$

we get an expression for the mean velocity of a single particle:

$$v_0 = \frac{D\lambda\left(1 - e^{-\beta f\lambda}\right)}{\mathcal{G}(\lambda)\int_0^\lambda e^{\beta(fx-U(x))}\mathrm{d}x - \left(1 - e^{-\beta f\lambda}\right)\int_0^\lambda \mathcal{G}(x)e^{\beta(fx-U(x))}\mathrm{d}x}. \tag{2.34}$$

Let us simplify it:

$$\begin{aligned} \mathcal{G}(\lambda) &- \mathcal{G}(x)(1 - e^{-\beta f\lambda}) \\ &= \int_0^\lambda e^{-\beta(fy-U(y))}\mathrm{d}y - \int_0^x e^{-\beta(fy-U(y))}\mathrm{d}y + e^{-\beta f\lambda}\int_0^x e^{-\beta(fy-U(y))}\mathrm{d}y \\ &= \int_x^\lambda e^{-\beta(fy-U(y))}\mathrm{d}y + \int_0^x e^{-\beta(f(y+\lambda)-U(y+\lambda))}\mathrm{d}y \\ &= \int_x^\lambda e^{-\beta(fy-U(y))}\mathrm{d}y + \int_\lambda^{x+\lambda} e^{-\beta(f(y)-U(y))}\mathrm{d}y = \int_x^{x+\lambda} e^{-\beta(fy-U(y))}\mathrm{d}y \end{aligned} \tag{2.35}$$

After substituting (2.35) into (2.34), we obtain the final expression:

$$v_0 = \frac{D\lambda\left(1 - e^{-\beta f\lambda}\right)}{\int_0^\lambda \mathrm{d}x\, e^{\beta(fx-U(x))} \int_x^{x+\lambda} \mathrm{d}y\, e^{-\beta(fy-U(y))}}. \tag{2.36}$$

In what follows, we use it to normalize the simulation currents. We note that point particles ($\sigma = 0$) can also be treated as independent in the collective dynamics [123].

Since an exact calculation of the current for nonzero particle size is a rather complicated task, we perform Brownian dynamics simulations in order to investigate the effects occurring in the BASEP. The details of the implemented algorithm are described in Chapter 5.

Current-density relations for the BASEP are presented in Fig. 2.2 for the parameters $U_0/k_\mathrm{B}T = 6$, $f\lambda/k_\mathrm{B}T = 0.2$ corresponding to the undercritical regime (see Sec. 2.1). For small particle size $0 \lesssim \sigma \lesssim 0.4$, the stationary current j_st is monotonically increasing with $\bar{\rho}$ and is always larger than the current of independent particles $v_0\bar{\rho}/\lambda$ due to a *barrier reduction effect* caused by a high probability of multiple particles to occupy one potential well. Since such particles are pushing each other to subsequent potential wells, the effective barrier is reduced. With increasing σ, the multiple occupation probability becomes smaller for steric reasons, and a *blocking effect* starts to prevail. This effect is well known in discrete systems such as the *asymmetric simple exclusion process* (ASEP) [124] and is explained by the fact that when particles move from one well to another, there is a

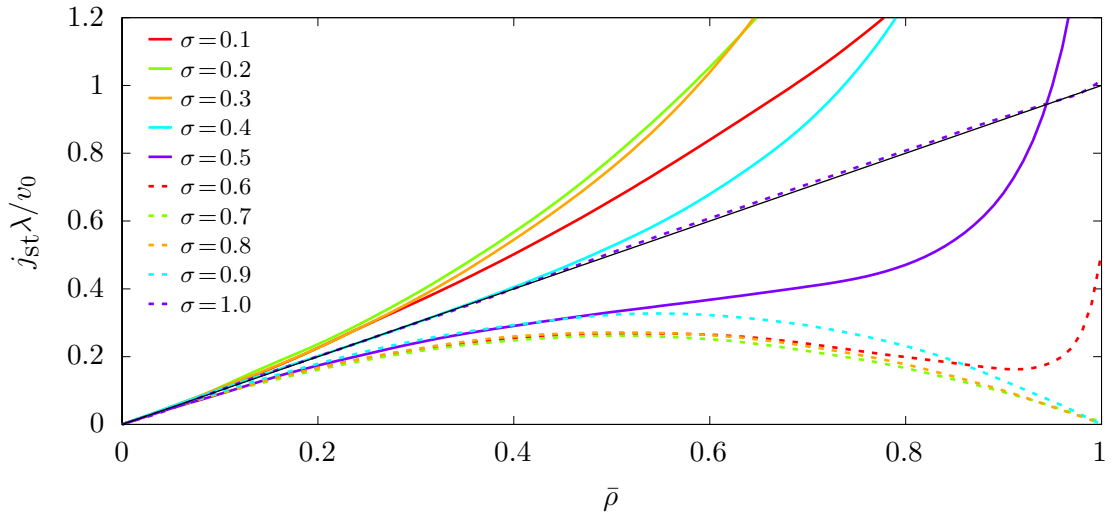

Figure 2.2: Current-density relation for hard particles at various particle sizes. The current is normalized to the mean velocity of non-interacting particle v_0. The black solid line with slope one represents the behavior of independent or point particles. The figure is reproduced from [91] with the permission of AIP Publishing.

high probability that a neighboring potential well is already occupied by another particle. For intermediate particle sizes $0.4 \lesssim \sigma \lesssim 0.6$, these two effects compete with each other. On one side, this causes a significant reduction in current compared to that of independent particles for $0 \lesssim \bar{\rho} \lesssim 0.8$ due to the blocking effect. On the other side, the current sharply increases at higher filling factors $0.8 \lesssim \bar{\rho} \lesssim 1.0$, since the probability of double occupation by particles of the same potential well again increases, so that the barrier reduction effect starts to prevail. For large particle sizes, $0.6 \lesssim \sigma \lesssim 1$, the blocking effect dominates the current behavior, and current-density curves approaches the parabolic ASEP curve $j_{\mathrm{st}} = v_0\bar{\rho}(1-\bar{\rho})/\lambda$ [124, 125]. For $\sigma \geq 1$, particle currents and density profiles can be rescaled to those at $0 \leq \sigma < 1$ by using the relation [85, 86]:

$$j_{\mathrm{st}}(\sigma, \bar{\rho}) = (1 - m\bar{\rho})\, j_{\mathrm{st}}\left(\sigma - m, \frac{\bar{\rho}}{1 - m\bar{\rho}}\right), \tag{2.37a}$$

$$\rho(x; \sigma, \bar{\rho}) = (1 - m\bar{\rho})\, \rho\left(x; \sigma - m, \frac{\bar{\rho}}{1 - m\bar{\rho}}\right), \quad m = \mathrm{int}(\sigma), \tag{2.37b}$$

or alternatively,

$$j_{\mathrm{st}}(\sigma + m, \bar{\rho}) = (1 + m\bar{\rho})\, j_{\mathrm{st}}\left(\sigma, \frac{\bar{\rho}}{1 + m\bar{\rho}}\right), \tag{2.38a}$$

$$\rho(x; \sigma + m, \bar{\rho}) = (1 + m\bar{\rho})\, \rho\left(x; \sigma, \frac{\bar{\rho}}{1 + m\bar{\rho}}\right), \quad m = 1, 2, \ldots. \tag{2.38b}$$

In what follows, we refer to this scaling behavior of current as the *exchange symmetry effect*. This effect in particular means, that the particle current for $\sigma = 1$ is equal to the one for $\sigma = 0$, i.e. the current of independent particles described by Eq. (2.27), see also the violet dashed line in Fig. 2.2 corresponding to this particle size.

The interplay of the barrier reduction, blocking, and exchange-symmetry effect, governs the dynamics of the BASEP [85]. Understanding the nature of these effects is the key for interpreting other, more complex features occurring in the BASEP described in Chapter 3.

2.3 Analytical treatment: approximation of the zero mean interaction force (AZMIF)

As noted in Sec. 2.2, the analytical calculation of the particle current is a challenging problem. The reason for that is the lack of information about the mean interaction force

in the nonequilibrium system. In this section, we present a method based on neglecting the impact of period-averaged mean interaction force.

Taking the exact expression for the steady-state current (2.25), dividing it by $\varrho(x)$, and integrating from 0 to λ results in:

$$j_{\mathrm{st}} = \mu \frac{f + \overline{f^{\mathrm{int}}}}{\frac{1}{\lambda}\int_0^\lambda \frac{\mathrm{d}x}{\varrho(x)}}, \tag{2.39a}$$

$$\overline{f^{\mathrm{int}}} = \frac{1}{\lambda}\int_0^\lambda f^{\mathrm{int}}(x)dx. \tag{2.39b}$$

In the linear response regime for small drag force f, Eq. (2.39a) reads

$$j_{\mathrm{st}} = \frac{1+\alpha}{\frac{1}{\lambda}\int_0^\lambda \frac{\mathrm{d}x}{\varrho_{\mathrm{eq}}(x)}}\mu f, \tag{2.40a}$$

$$\alpha = \left.\frac{\partial \overline{f^{\mathrm{int}}}}{\partial f}\right|_{f=0} \tag{2.40b}$$

where ϱ_{eq} is the equilibrium density profile ($f = 0$).

The current is thereby influenced by the mean interaction force. By neglecting the impact of the period-averaged mean interaction force ($\alpha = 0$), we obtain an approximation for the steady-state current. In what follows we refer to this approach as to the *approximation of zero mean interaction force* (AZMIF).

Results for Brownian dynamics simulations and the AZMIF are presented in Fig. 2.3 for $U_0/k_{\mathrm{B}}T = 6$ and small drag force $f\lambda/k_{\mathrm{B}}T = 0.2$. We see that the AZMIF captures the qualitative features of the current-density relations and has a good agreement with Brownian dynamics simulations for $\sigma = 0.2$ (green curve) and $\sigma = 0.8$ (violet curve). However, for $\sigma = 0.5$ there is a significant difference due to the fact that the AZMIF underestimates the contribution of the term $\overline{f^{\mathrm{int}}}$ in Eq. (2.39a). Thus, we can conclude that the contribution of the mean interaction force to the particle current is negligible if one of the effects dominates over another, and significant if these effects compete with each other.

To keep α nonzero, we need to determine the mean interaction force in Eqs. (2.39b), (2.40b). The direct calculation from Eq. (2.11) requires the explicit expression for the two-particle density $\varrho^{(2)}(x, y)$. Its determination is a very challenging task which is a core problem for a successful application of e.g. the DDFT mentioned in Sec. 2.2.1 or other related approaches that are usually applied in stochastic processes.

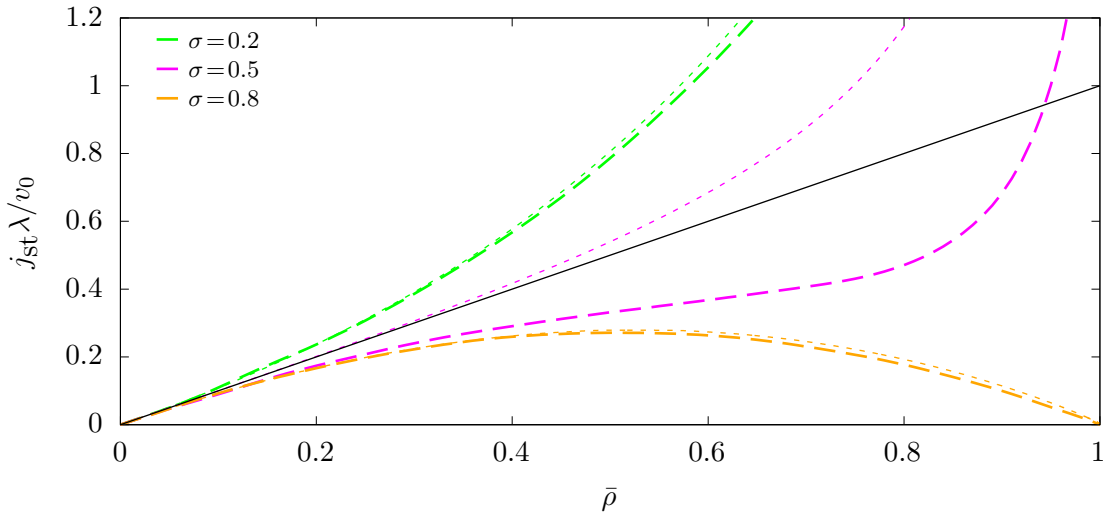

Figure 2.3: Current-density curves for three representative cases: $\sigma = 0.2$ (barrier reduction effect is dominant, green), $\sigma = 0.5$ (barrier reduction and blocking effects are competing, violet), and $\sigma = 0.8$ (blocking effect is dominant, orange). Thin-dashed curves correspond to the AZMIF, and thick-dashed curves to Brownian dynamics simulations. The AZMIF is able to capture the qualitative behavior of current-density curves and gives a good description for cases when one effect dominates the other ($\sigma = 0.2$ and $\sigma = 0.8$). It is quantitatively different from the simulation results when effects are competing with each other ($\sigma = 0.5$, where the blocking effect is significantly underestimated by the AZMIF).

2.4 Summary notes

In this chapter, we have introduced the BASEP as a framework for investigating the crowding effects at high densities. Here we briefly summarize the main features of the BASEP.

The current in the BASEP for the constant external potential and drag force is influenced by the particle size σ and the filling factor $\bar{\rho}$. Depending on these parameters, the BASEP can exhibit the following three effects: barrier reduction, blocking, and exchange-symmetry effect. A competition between these effects determines the shape of current-density curves. The curves were obtained both from simulations and by analytical means.

The implemented analytical approach (AZMIF) is based on the reference equilibrium system, where the main properties are known for the grand canonical ensemble. The impact of the period-averaged mean interaction force, the analytical determination of which remains an open and rather complicated problem, is neglected. This approach gives us a qualitative understanding of transport properties in the BASEP.

We also briefly discuss other analytical approaches that we have implemented to determine mean interaction forces. However, these methods do not lead to significant improvements compared to the AZMIF.

2.4.1 Dynamic density functional theory (DDFT)

The dynamic density functional theory, or DDFT, is a powerful tool which is employed in various fields, including hydrodynamics, materials science, chemistry, biology, and plasma physics [121]. In our system, we utilize DDFT based on the equilibrium theory (2.21) [118, 119, 122], which enables us to relate the two-particle density at contact to the single-particle density via Eq. (2.24). By combining it with Eqs. (2.9a) and (2.12), we can derive an equation for the evolution of the density profile, which is as follows:

$$\begin{aligned}\frac{\partial \varrho(x,t)}{\partial t} &= -\frac{\partial}{\partial x}\Bigg\{\mu\left(f - U'(x)\right)\varrho(x,t) \\ &+ D\varrho(x,t)\left[\frac{\varrho(x-\varsigma,t)}{1-\eta(x,t)} - \frac{\varrho(x+\varsigma,t)}{1-\eta(x+\varsigma,t)}\right] - D\frac{\partial \varrho(x,t)}{\partial x}\Bigg\}. \end{aligned} \tag{2.41}$$

The interaction force in the stationary state then reads:

$$f^{\mathrm{int}}(x) = k_{\mathrm{B}}T\left[\frac{\varrho(x-\varsigma)}{1-\eta(x)} - \frac{\varrho(x+\varsigma)}{1-\eta(x+\varsigma)}\right]. \tag{2.42}$$

However, in the stationary state the resulting interaction force $f^{\mathrm{int}}(x)$ is symmetric with respect to $x = 0.5\lambda$, as shown in the example in Fig. 2.4, and therefore also does not contribute to the current in the Eq. (2.39a). Indeed, as is shown in [86], DDFT and AZMIF give overall similar results.

The contribution of the mean interaction force that cannot be described by adiabatic assumptions that are based on equilibrium system properties, is called beyond-adiabatic [126], or *superadiabatic* contribution to the system dynamics [127]. To account for these corrections, a modification of the DDFT is necessary. Recent methods include the *force-DDFT*, which proposes an evolution equation for the particle density by making an adiabatic approximation to the two-particle density [128], and the *superadiabatic-DDFT*, which involves treating the dynamics of inhomogeneous two-particle correlation functions [129]. The potential power of these methods has been demonstrated through investigations of density profiles for a model of three-dimensional spheres subjected to an external time-dependent potential in Refs. [130] and [131], respectively.

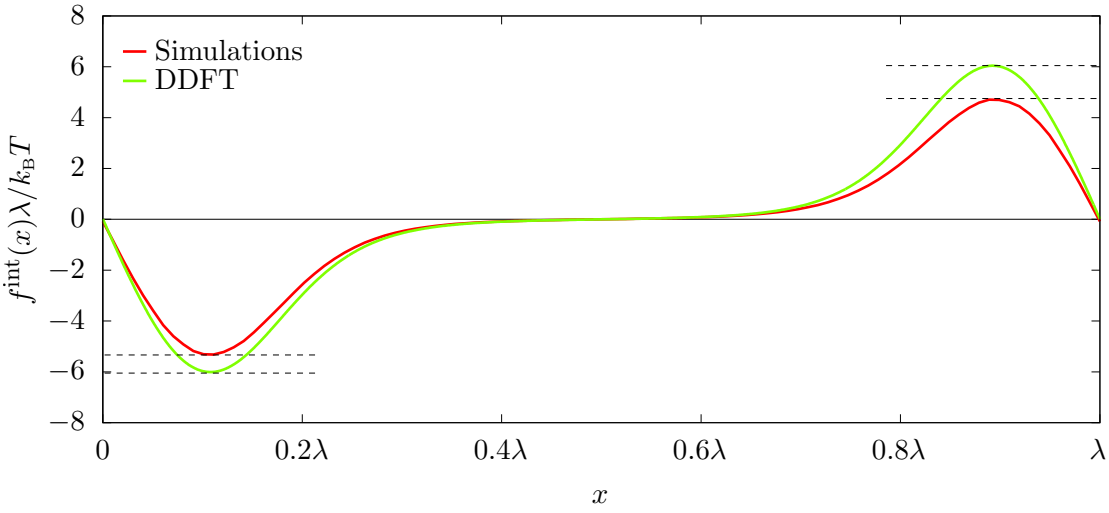

Figure 2.4: Comparison of simulated interaction force f^{int} (red line) with the result of DDFT given by Eq. (2.42) (green line) for parameters $\sigma = 0.5$, $\bar{\rho} = 0.9$. Both results lead to similar force profiles. However, while DDFT being symmetric with respect to $x = 0.5\lambda$, in simulation the left wing for $x < 0.5\lambda$ has bigger amplitude than that for the right wing, $x > 0.5\lambda$. This results in a negative period-averaged mean interaction force in simulations. Peak amplitudes are represented by the dashed lines.

The superadiabatic contribution resulting from the asymmetry of the mean interaction force profile can be understood from another perspective: on average, collisions occurring on the right (drag force) side, which decelerate the particle, exhibit greater effect compared to collisions on the left side, which contribute to its acceleration. This phenomenon can be attributed to a violation of the action-reaction principle, induced by the nonequilibrium nature of the considered system [132–134]. To account for this violation, we introduce a perturbation function in Eq. (2.13):

$$f^{(2)}(x,y) = k_{\mathrm{B}}T\left\{\delta(y-(x-\varsigma))[1+\vartheta(x)] - \delta(y-(x+\varsigma))[1-\vartheta(x)]\right\}, \tag{2.43}$$

where $\vartheta(.)$ is a perturbation function. The interaction force is then modified in the following way:

$$f^{\mathrm{int}}(x) = k_{\mathrm{B}}T\left[\frac{\varrho(x-\varsigma)[1-\vartheta(x)]}{1-\eta(x)} - \frac{\varrho(x+\varsigma)[1+\vartheta(x)]}{1-\eta(x+\varsigma)}\right], \tag{2.44}$$

where the perturbation function can be expressed as

$$\vartheta(x) = \frac{\dfrac{\varrho(x-\varsigma)}{1-\eta(x)} - \dfrac{\varrho(x+\varsigma)}{1-\eta(x+\varsigma)} - f^{\mathrm{int}}(x)}{\dfrac{1}{1-\eta(x)} - \dfrac{1}{1-\eta(x+\varsigma)}} \tag{2.45}$$

$$= \frac{\varrho(x-\varsigma)[1-\eta(x+\varsigma)] - \varrho(x+\varsigma)[1-\eta(x)] - f^{\mathrm{int}}(x)[1-\eta(x+\varsigma)][1-\eta(x)]}{\eta(x)-\eta(x+\varsigma)}.$$

By substituting the simulation results for $f^{\mathrm{int}}(x)$ and $\varrho(x)$ into Eq. (2.45), we can observe the behavior of the perturbation function, as shown in Fig. 2.5. As is evident from this figure, the shape of the perturbation function is strongly dependent on the particle size, indicating the nontrivial nature of particle collisions in the nonequilibrium state.

2.4.2 Potential of mean force

The idea of this approach is to calculate the current of independent particles in the external potential of mean force $w(x)$, set through particle distribution in the equilibrium steady-state:

$$\varrho_{\mathrm{eq}}(x) \propto e^{-\beta w(x)}. \tag{2.46}$$

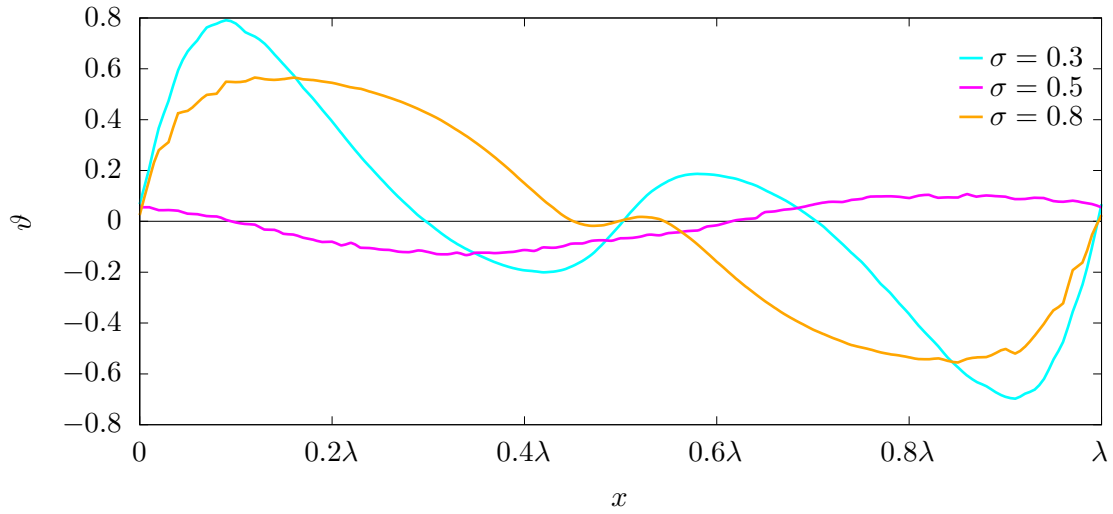

Figure 2.5: Perturbation function $\vartheta(x)$ for $\bar{\rho} = 0.5$ and particle sizes $\sigma = 0.3$ (cyan), $\sigma = 0.5$ (violet), $\sigma = 0.8$ (orange).

Equation (2.9a) then reads:

$$\frac{\partial \varrho(x,t)}{\partial t} = -\frac{\partial}{\partial x}\left[\mu\left(f - w'(x)\right)\varrho(x,t) - D\frac{\partial \varrho(x,t)}{\partial x}\right]. \tag{2.47}$$

From Eq. (2.19), we obtain the potential of mean force $w(x)$:

$$w(x) = C - \ln \varrho_{\mathrm{eq}}(x) = U(x) - k_{\mathrm{B}}T\left(\ln[1-\eta_{\mathrm{eq}}(x)] + \int_x^{x+\varsigma} \mathrm{d}y \frac{\varrho_{\mathrm{eq}}(y)}{1-\eta_{\mathrm{eq}}(y)}\right) + C. \tag{2.48}$$

Substituting Eq. (2.48) into Eq. (2.47) gives us the following evolution equation:

$$\begin{aligned}\frac{\partial \varrho(x,t)}{\partial t} &= -\frac{\partial}{\partial x}\Bigg\{\mu\left(f - U'(x)\right)\varrho(x,t) \\ &+ D\varrho(x,t)\left[\frac{\varrho_{\mathrm{eq}}(x-\varsigma)}{1-\eta_{\mathrm{eq}}(x)} - \frac{\varrho_{\mathrm{eq}}(x+\varsigma)}{1-\eta_{\mathrm{eq}}(x+\varsigma)}\right] - D\frac{\partial \varrho(x,t)}{\partial x}\Bigg\},\end{aligned} \tag{2.49}$$

which is structurally identical to DDFT evolution equation given by Eq. (2.41).

The formula for the current of independent particles in the potential of mean force can be derived by combining Eqs. (2.27) and (2.36):

$$j_{\mathrm{st}} = \frac{D\bar{\rho}\left(1 - e^{-\beta f \lambda}\right)}{\displaystyle\int_0^{\lambda} \mathrm{d}x\, e^{\beta f x}\varrho_{\mathrm{eq}}(x)\int_x^{x+\lambda} \mathrm{d}y\, e^{-\beta f y}\varrho_{\mathrm{eq}}^{-1}(y)}. \tag{2.50}$$

The obtained result is depicted in Fig. 2.6. Similar to the conceptually analogous DDFT, this method yields outcomes comparable to the AZMIF.

2.4.3 Fick-Jacobs approximation

The problem of determining the mean interaction force is challenging even for the case of two particles in a system. To illustrate this point, we employ the Fick-Jacobs equation [135, 136]:

$$\frac{\partial \varrho(x,t)}{\partial t} = -\frac{\partial}{\partial x}\left[\mu\left(f - U'(x) + \frac{A'(x)}{A(x)}\right)\varrho(x,t) - D\frac{\partial \varrho(x,t)}{\partial x}\right], \tag{2.51}$$

where the function $A(x)$ would be determined by the ansatz that the conditional probability $\varrho(y|x) = \varrho^{(2)}(x,y)/\varrho(x)$ has the equilibrium distribution in the domain of y. This domain is set between $x + \varsigma$ and $x + L - \varsigma$ due to the hardcore constraint and periodic

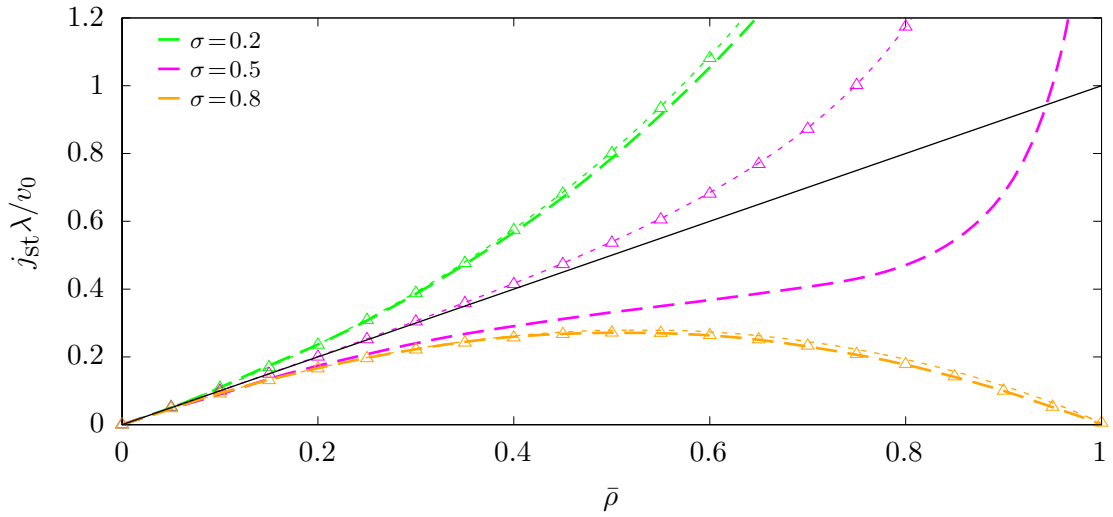

Figure 2.6: Comparison of current-density relations obtained from Eq. (2.50) with current-density relations presented in Fig. 2.3. The results obtained by using the potential of mean force are shown by triangles and are identical to the AZMIF indicated by thin dashed lines, and are different from results of Brownian dynamics simulations indicated by thick dashed lines.

boundary condition. We choose this ansatz based on the similarity with the assumption made in DDFT, where we assume that the interaction processes in the system have an equilibrium nature.

For a single particle, the conditional probability $\varrho(y|x)$ follows the Boltzmann distribution:

$$\varrho(y|x) = \frac{e^{-\beta U(y)}}{A(x)}, \tag{2.52a}$$

where $A(x)$ is the normalization function given by:

$$A(x) = \int_{x+\varsigma}^{x+L-\varsigma} e^{-\beta U(y)} \mathrm{d}y. \tag{2.52b}$$

The two-particle density takes the form:

$$\varrho^{(2)}(x,y) = \frac{e^{-\beta U(y)}\varrho(x)}{A(x)}, \tag{2.53}$$

and integrating it over the y-domain gives the one-particle density:

$$\varrho(x) = \int_{x+\varsigma}^{x+L-\varsigma} \varrho^{(2)}(x,y)\mathrm{d}y. \tag{2.54}$$

The corresponding Smoluchowski equation for the two-particle density is:

$$\begin{aligned}\frac{\partial \varrho^{(2)}(x,y,t)}{\partial t} &= -\frac{\partial}{\partial x}\left[\mu(f-U'(x))\varrho^{(2)}(x,y,t) - D\frac{\partial \varrho^{(2)}(x,y,t)}{\partial x}\right] \\ &- \frac{\partial}{\partial y}\left[\mu(f-U'(y))\varrho^{(2)}(x,y,t) - D\frac{\partial \varrho^{(2)}(x,y,t)}{\partial y}\right],\end{aligned} \tag{2.55}$$

By integrating it over the y-domain from $x+\varsigma$ to $x+L-\varsigma$, and taking into account the non-crossing boundary conditions for the current [123],

$$0 = [j_y(x,y) - j_x(x,y)]\Big|_{y=x+\varsigma}^{y=x+L-\varsigma} \tag{2.56a}$$

where

$$\begin{aligned} j_x(x,y) &= \mu(f-U'(x))\varrho^{(2)}(x,y,t) - D\frac{\partial \varrho^{(2)}(x,y,t)}{\partial x}, \\ j_y(x,y) &= \mu(f-U'(x))\varrho^{(2)}(x,y,t) - D\frac{\partial \varrho^{(2)}(x,y,t)}{\partial y}, \end{aligned} \tag{2.56b}$$

we obtain the Fick-Jacobs equation (2.51) with $A(x)$ given by the Eq. (2.52b). Another way to interpret this equation is that it describes the diffusion of particles in a narrow two-dimensional channel with a width $A(x)$ [136, 137].

For the Equation (2.51), the steady-state current has the form

$$j_{\mathrm{st}} = \mu\left(f - U'(x) + \frac{A'(x)}{A(x)}\right)\varrho(x) - D\frac{\partial \varrho(x)}{\partial x}. \tag{2.57}$$

Equation (2.57) can be solved analogously to the means we have implemented for the Eq. (2.28), with the adjusted potential $U(x) \to (U(x) - \log A(x))$. The modified solution reads:

$$j_{\mathrm{st}} = \frac{D\bar{\rho}\left(1 - e^{-\beta f \lambda}\right)}{\displaystyle\int_0^{\lambda} \mathrm{d}x\, e^{\beta(fx - U(x) + \log A(x))} \int_x^{x+\lambda} \mathrm{d}y\, e^{-\beta(fy - U(y) + \log A(y))}}. \tag{2.58}$$

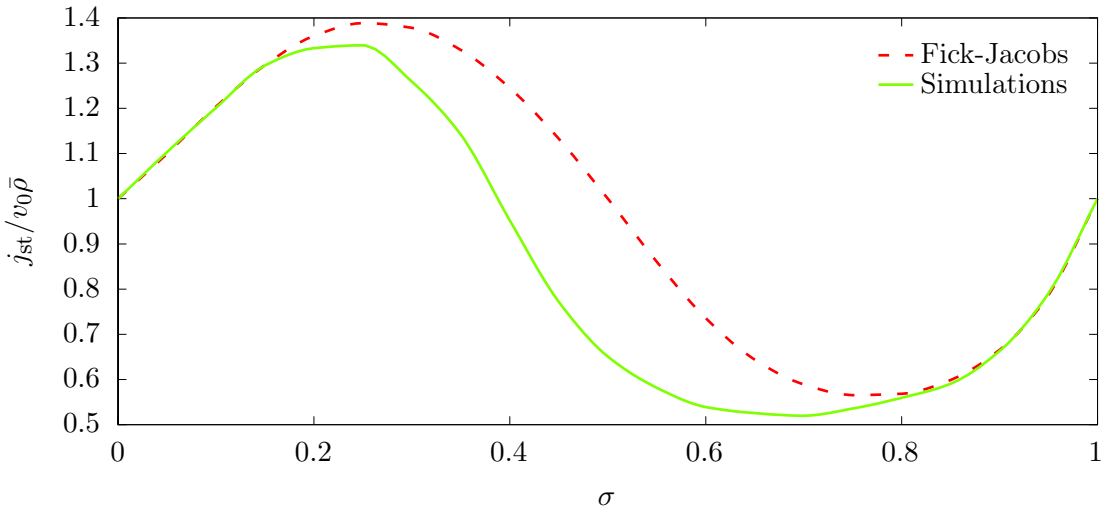

Figure 2.7: The current of two particles in a system of length $L = 3\lambda$ represented by the Fick-Jacobs equation (dashed red) and by numerical simulations (solid green), as a function of σ.

The results for the current of two particles in a system of length $L = 3\lambda$ are presented in Fig. 2.7. As with the AZMIF in a many-body system, the approximate solution provided by the Fick-Jacobs equation shows good agreement with simulation results for small and large particle sizes, but there is a significant difference for intermediate particle sizes.

3 Brownian solitons

3.1 Introduction

As we have revealed in Chapter 2, the blocking effect dominates in the BASEP with high volume fraction. Thus, the current in such systems should tend to zero for $\bar{\rho} \to 1$, and its value could be qualitatively predicted by the AZMIF for systems close to the thermodynamic limit. However, the situation for systems with finite length is different, as can be seen in Fig. 3.1(a). In this figure, we present simulated results for particle currents for the filling factor $\bar{\rho} = 1$, i.e. when the number of particles is equal to the number of

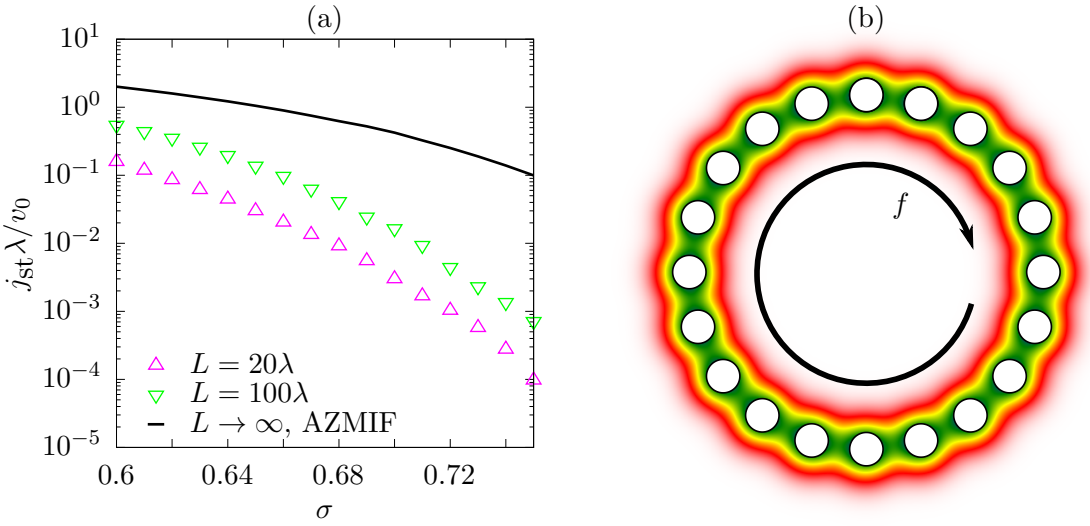

Figure 3.1: (a) Simulated steady-state currents for the filling factor $\bar{\rho} = 1$ as a function of particle size σ for system length $L = 20\lambda$ (magenta triangles) and $L = 100\lambda$ (green triangles), compared to the steady-state current in the thermodynamic limit ($L \to \infty$) predicted by the AZMIF (solid line). (b) An experimental realization of the model for $L = 20\lambda$: a ring of 20 optical Gaussian traps filled with the same number of hard spheres of size $\sigma = 0.6$ in a fluid environment [108]. Color map represents optical traps, with green areas corresponding to potential minima and red areas corresponding to potential maxima. The drag force f drives hard spheres in the clockwise direction.

potential wells, see also the sketch of possible experimental realization in Fig. 3.1(b). We compare the currents simulated for system length $L = 20\lambda$ and $L = 100\lambda$ with currents in the thermodynamic limit predicted by the AZMIF. This comparison allows us to analyze the impact of system length on transport behavior. In this chapter, we consider the same potential amplitude and drag force values used in the Chapter 2 ($U_0/k_\mathrm{B}T = 6$, $f\lambda/k_\mathrm{B}T = 0.2$, respectively), unless specified otherwise.

Two questions now arise from observations of Fig. 3.1(a): (i) why does the predicted limit strongly deviate from the simulated data by many orders of magnitude, and (ii) why is the particle current present for large ($\sigma \gtrsim 0.6$) particle sizes, despite the highly improbable occurrence of double occupancies of potential wells and the consequent dominance of the blocking effect within this range due to steric reasons?

The answer to the first question is that the considered systems are out of the thermodynamic limit. As a result, the current behavior is strongly affected by the finite system size. In fact, the current decrease with increasing particle size is much stronger for finite systems ($L = 20\lambda$ and $L = 100\lambda$) than for the system in the thermodynamic limit, see Fig. 3.1(a). In addition, the current amplitude at the same particle size is several orders of magnitude smaller for finite-size systems compared to that in the thermodynamic limit. However, for the larger system length $L = 100\lambda$, the simulation results are significantly closer to the ones by the AZMIF than those for $L = 20\lambda$. While increasing the system length leads to a better agreement between the simulation data and the AZMIF, it also requires a significant increase in computational time due to the higher frequency of collisions between hard particles [138].

The reason why there is a particle current present for large particle sizes is attributed to the possibility of particle motion becoming feasible when multiple particles escape a

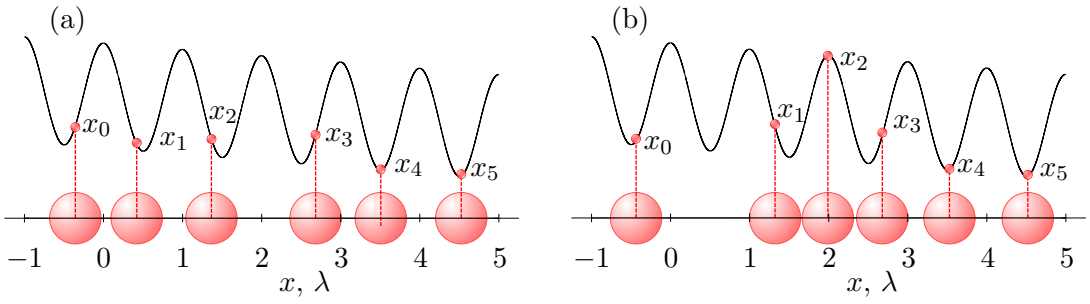

Figure 3.2: (a) An example of steady-state crystalline-like structure, with all particles located in the vicinity of the position of stable mechanical equilibria. (b) After some time, a collective excitation of particles at positions x_1 and x_2 leads to the cluster generation. The particle size in both figures is $\sigma = 0.65$.

potential well within a short period of time, as illustrated in Fig. 3.2. We refer to such events as collective excitations [139], which, albeit rarely, must occur in any crowded system due to entropic reasons. In corresponding discrete systems, e.g. in the ASEP, these collective excitations are not observed, since for $\sigma > 0.5$ *all* particles need to escape from their lattice sites at the same moment in order for the particle current to take place. This is practically impossible to occur in a large system.

When particles have escaped from their potential minima, they are in contact or almost in contact with each other, forming *clusters*. An n-cluster, consisting of n particles, occupies $n-1$ potential wells. Such a cluster could be stable only in crowded ($\bar{\rho} = 1$) systems, as it would recombine if there is a free potential well where one of cluster's particles might escape to locally equilibrate the system, i.e. when each of the n particles would be localized in the vicinity of a potential minimum. Clusters can also occur in a "natural" way when number of particles exceeds the number of potential wells. The system behavior in crowded systems with large particle sizes ($\bar{\rho} = 1$, $\sigma \gtrsim 0.6$) and overcrowded ($\bar{\rho} > 1$) systems is governed by the dynamics of these clusters.

This chapter is devoted to the analysis of such clusters, and organized as follows. In Sec. 3.2, we consider *thermally activated* clusters and derive their main properties. We also show that these clusters have the same origin as *crowding-induced* ones that take place in overcrowded systems. These crowding-induced clusters are investigated in Sec. 3.3.

3.2 Thermally activated clusters

3.2.1 Generation rate

In a fully occupied system with the filling factor $\bar{\rho} = 1$ energetically preferable structure is the crystalline-like one, see Fig. 3.2(a): particles are localized near the position of stable mechanical equilibria of the tilted potential $U(x) - fx$. The equilibria positions are determined by the zero external force $f - U'(x)$:

$$f + \frac{\pi U_0}{\lambda} \sin\left(\frac{2\pi x}{\lambda}\right) = 0 \tag{3.1}$$

Accordingly, the equilibria positions are as follows:

$$x_m^{\min} = (m - 1/2 + \chi)\lambda, \quad m = 1, 2, \ldots, N, \tag{3.2a}$$

$$x_m^{\max} = (m - \chi)\lambda, \quad m = 1, 2, \ldots, N, \tag{3.2b}$$

$$\chi = \frac{1}{2\pi} \arcsin\left(\frac{f\lambda}{\pi U_0}\right), \tag{3.2c}$$

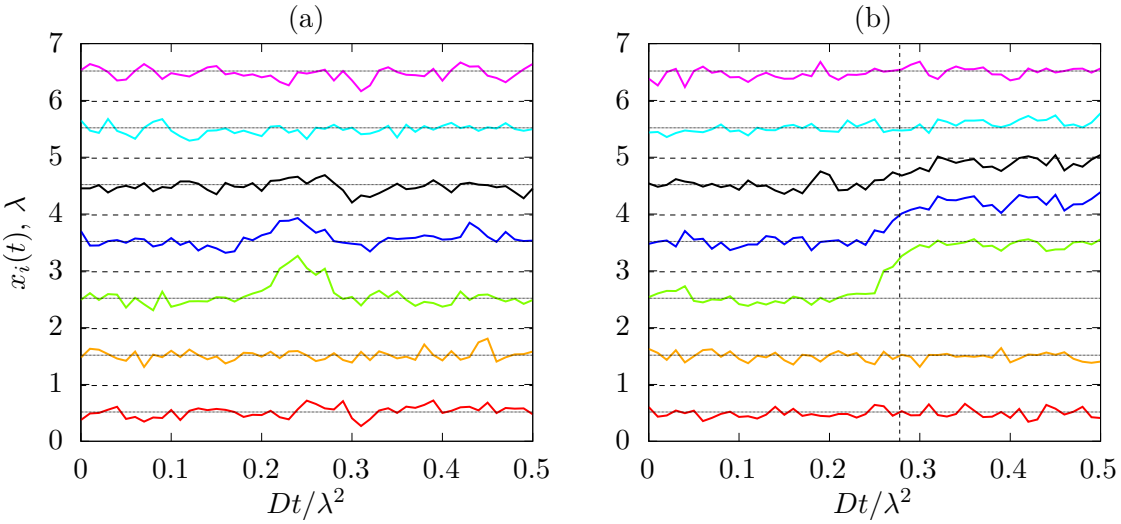

Figure 3.3: Simulated particle trajectories for $\sigma = 0.65$. In both panels, the particle whose trajectory is marked green passes the potential barrier. In (a) no cluster is formed since this particle returns back shortly after the passage of barrier. In (b), there is a cluster formation at the moment when the transition state is reached (marked with a vertical line at $Dt_\times/\lambda^2 \approx 0.28$).

where $x^{\min}$ correspond to stable equlibria positions (potential minima), and $x^{\max}$ correspond to unstable equilibria positions (potential maxima, i.e. tops of potential barrier). For the given parameters $U_0/k_\mathrm{B}T = 6$ and $f\lambda/k_\mathrm{B}T = 0.2$, $\chi \cong 0.017$.

The generation of a cluster is accompanied by the formation of an empty potential well behind it, see Fig. 3.2(b). This cluster can then disappear after a short time, if the particle that has escaped from the potential well, leaving it empty, returns back, see the particle trajectory marked in green in Fig. 3.3(a). Alternatively, it can start to propagate in the drag force direction, see Fig. 3.3(b). The empty potential well in this case slowly moves in the opposite direction with the mean velocity v_0, as particles leak across the barrier due to thermal noise, occupying the previously vacated potential well.

Since the collective excitation has two different types of behavior, it is obvious that there is a *transition state* between these two regimes, which corresponds to an equal probability of a cluster to recombine and propagate. If we consider a single particle as a 1-cluster, then for smooth potentials the transition state is in the position of unstable equilibrium. Let us specify the transition state for an n-cluster with the cluster particles numbered from 1 to n in ascending order in the drag force direction, as follows: ***if n-cluster's particles 1,2,. . . ,k, with***

$$k = \lfloor n/2 \rfloor, \tag{3.3}$$

have passed one potential barrier (one top of potential barrier) in the drag force direction, and the (k+1)-th particle is in the potential maximum next to the k-th particle, then this particle configuration is in transition state. Thus, depending on the direction in which the $(k{+}1)$-th particle moves from the top of potential barrier, we have either more than half of the cluster's particles that have passed the potential barrier or less than half, which shifts the balance toward cluster propagation or recombination, respectively. If more than half of the cluster's particles have passed the potential barriers, they push the subsequent particles through, thus contributing to their propagation toward the next potential well. Otherwise, particles remaining in their potentials oppose this pushing, preventing particles that have crossed the potential barrier from propagating forward and eventually forcing them back to their initial potential wells.

The illustration of transition state is given in Fig. 3.2(b): a 3-cluster consisting of particles at positions x_1, x_2 and x_3 has $k = \lfloor 3/2 \rfloor = 1$ particle that has passed one potential barrier (at position x_1), and the next particle (at position x_2) is in the subsequent potential maximum.

Obviously, the transition state strictly defined until the clear definition of a cluster is given. However, the number of particles in contact with each other may vary over time due to thermal fluctuations in the system, see e.g. particles at position x_0 and x_1 in Fig. 3.2(a), which come close to each other in spite of the fact that they are in different potential wells in the steady-state system and thereby do not form a cluster. Thus, it is more practical to calculate the number of particles k that are required to pass one potential barrier to generate a cluster. In order to do this, we calculate k based on energetic reasons. To calculate the free energy $F_k^{\ddagger}(\sigma)$ of the transition state and the free energy $F_k^0(\sigma)$ of a corresponding reference (standard) state, we fix two boundary particles at positions of stable mechanical equilibrium, with the left boundary particle at position $x_{\mathrm{b}}^- = x_1^{\min}$ and the right boundary particle at position $x_{\mathrm{b}}^+ = x_{2k+2}^{\min}$. This means that we place these boundary particles at a distance of $(2k+1)$ wavelengths, which allows $2k$ particles to occupy $2k$ different potential wells in the reference state and form clusters of size $(2k+1)$ in the transition state, including one of the boundary particles. Thus, this choice of distance between two boundary particles allows the formation of clusters that satisfy the condition (3.3).

The particle k is then fixed at the position $x_k^\dagger = x_k^{\max}$ in the transition state. Therefore, it should be also fixed in the reference state, but at the position of stable mechanical equilibrium at $x_k^0 = x_k^{\min}$. The partition sum of the reference state reads

$$\begin{aligned} Z_k^0 &= \exp[-\beta(U(x_k^0) - f x_k^0)] \int\limits_{x_k^0+\varsigma}^{x_\mathrm{b}^+-k\varsigma} \mathrm{d}x_{k+1} \int\limits_{x_{k+1}+\varsigma}^{x_\mathrm{b}^+-(k-1)\varsigma} \mathrm{d}x_{k+2} \ldots \int\limits_{x_{2k-1}+\varsigma}^{x_\mathrm{b}^+-\varsigma} \mathrm{d}x_{2k} \\ &\times \int\limits_{x_\mathrm{b}^-+(k-1)\varsigma}^{x_k^0-\varsigma} \mathrm{d}x_{k-1} \int\limits_{x_\mathrm{b}^-+(k-2)\varsigma}^{x_{k-1}-\varsigma} \mathrm{d}x_{k-2} \ldots \int\limits_{x_\mathrm{b}^-+2\varsigma}^{x_3-\varsigma} \mathrm{d}x_2 \int\limits_{x_\mathrm{b}^-+\varsigma}^{x_2-\varsigma} \mathrm{d}x_1 \exp\Bigg\{ - \sum_{j=1, j\neq k}^{2k} \beta[U(x_j) - f x_j] \Bigg\}. \end{aligned} \tag{3.4}$$

In the transition state, we have an additional requirement that particles $x_1, \ldots, x_{k-1}$ have passed one potential barrier which needs to be taken into account in corresponding integration limits. The partition sum of this transition state then reads as follows:

$$\begin{aligned} Z_k^\ddagger &= \exp[-\beta(U(x_k^\ddagger) + f x_k^\ddagger)] \int\limits_{x_k^\dagger+\varsigma}^{x_\mathrm{b}^+-k\varsigma} \mathrm{d}x_{k+1} \int\limits_{x_{k+1}+\varsigma}^{x_\mathrm{b}^+-(k-1)\varsigma} \mathrm{d}x_{k+2} \ldots \int\limits_{x_{2k-1}+\varsigma}^{x_\mathrm{b}^+-\varsigma} \mathrm{d}x_{2k} \\ &\times \int\limits_{x_{k-1}^{\max}}^{x_k^\dagger-\varsigma} \mathrm{d}x_{k-1} \int\limits_{x_{k-2}^{\max}}^{x_{k-1}-\varsigma} \mathrm{d}x_{k-2} \ldots \int\limits_{x_2^{\max}}^{x_3-\varsigma} \mathrm{d}x_2 \int\limits_{x_1^{\max}}^{x_2-\varsigma} \mathrm{d}x_1 \exp\Bigg\{ - \sum_{j=1, j\neq k}^{2k} \beta[U(x_j) - f x_j] \Bigg\}. \end{aligned} \tag{3.5}$$

The generation rate of a propagating cluster which resulted via k-particle transition state $\varpi_k(\sigma)$ can then be expressed through the free energy barrier between the transition and reference states. Since $F = -k_\mathrm{B}T \log Z$, we obtain

$$\varpi_k(\sigma) = \nu \exp[-\beta(F_k^\ddagger(\sigma) - F_k^0(\sigma))] = \nu \frac{Z_n^\ddagger(\sigma)}{Z_n^0(\sigma)}, \tag{3.6}$$

where ν is the bare rate constant. For the given parameters $U_0/k_\mathrm{B}T = 6$, $f\lambda/k_\mathrm{B}T = 0.2$, and $D = \mu k_\mathrm{B}T = 1$, the bare rate is $\nu \cong D/\lambda^2$ [138].

The further arising question is how to determine the transition state, i.e. how to find the k value that is sufficient for a generated cluster to start propagating. In order to do this, let us appeal to Fig. 3.4, which shows the propagating clusters for different values of σ. We note that in order for the k-particle transition state to be created, first all $1, 2, \ldots, (k-1)$-particle transition states need to take place. On the other hand, while propagating and before hole refilling, the cluster also passes through $(k+1), (k+2), \ldots, (N-1)$-particle

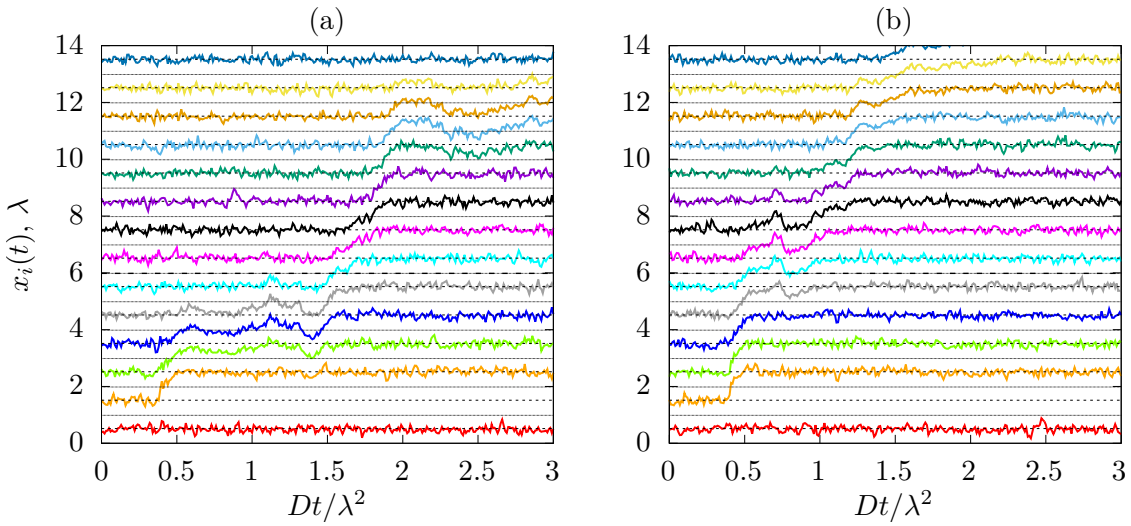

Figure 3.4: Propagating clusters for (a) $\sigma = 0.65$ and (b) $\sigma = 0.75$. The figure is adapted from [138], in accordance with the Creative Commons Attribution (CC BY) license (https://creativecommons.org/licenses/by/4.0/).

transition states. Thus, for the cluster to start propagating, the energy must be sufficient to pass the transition state with the *maximum* free energy barrier $\Delta F_n^{\ddagger}(\sigma) = [F_n^{\ddagger}(\sigma) - F_n^0(\sigma)]$. The transition state $k^{\ddagger}$ is thereby defined via the maximization principle,

$$k^{\ddagger}(\sigma) = \underset{k}{\operatorname{argmax}}\{\Delta F_k^{\ddagger}(\sigma)\}\,, \tag{3.7}$$

and the generation rate is then $\varpi_{\mathrm{gen}} = \varpi_{k^{\ddagger}}$.

The theoretical prediction is in a good agreement with the simulation data, see Fig. 3.5(a). The staircase-like increase of $k^{\ddagger}$ with particle size σ is shown in Fig. 3.5(b). This also gives us insights into different behavior of clusters shown in Fig. 3.3: since $k^{\ddagger} = 2$ for the considered $\sigma = 0.65$ according to Fig. 3.5(b), the corresponding transition state is reached in Fig. 3.3(b) at time $t_{\times} \approx 0.28\lambda^2/D$, followed by the propagation of a cluster, while in Fig. 3.3(a) only a 1-particle transition state is reached, and the cluster recombines shortly after its generation.

It also becomes evident that the strong decrease in current with increasing particle size, as demonstrated in Fig. 3.1, is associated with a corresponding drastic decrease of ϖ_{gen} shown in Fig. 3.5. To complete the picture of cluster behavior, we also need to understand the origin of cluster propagation and dependence of its velocity on the particle size.

3.2.2 Cluster velocity. The concept of a soliton

In order to calculate the cluster velocity v_{cl}, we are tracking it in the time interval $[t_a, t_b]$. To avoid inaccuracies of the velocity calculation associated with the effect of a cluster generation and recombination on the velocity of its propagation, we exclude from the consideration the time interval D/λ^2 after cluster generation and the same time interval before its recombination. The position of a cluster is defined as the position of the double occupied potential well. Taking the cluster positions x_a, x_b at the beginning and at the end of the considered time interval, respectively, we obtain the following expression for the cluster velocity:

$$v_{\mathrm{cl}} = \left\langle \frac{x_b^i - x_a^i}{t_b^i - t_a^i} \right\rangle_i , \tag{3.8}$$

where $\langle \ldots \rangle_i$ denotes averaging over the series of time intervals $[t_a^i, t_b^i]$. Since the cluster generation is a rare event, especially for large particles sizes, one can consider a cluster created in a "natural" way (see Sec. 3.1) by inserting an additional particle into the fully occupied system with the filling factor $\bar{\rho} = 1$. Such crowding-induced cluster has the

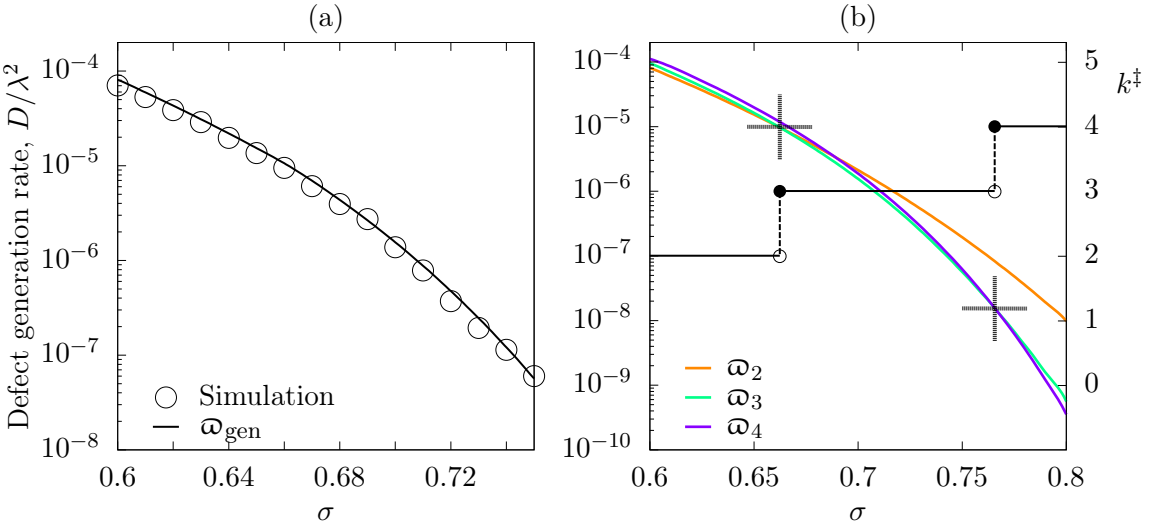

Figure 3.5: (a) Cluster generation rate for different particle sizes, theoretically predicted by Eqs. (3.6), (3.7) (solid line), in comparison with simulation data (circles). (b) Generation rates for various transition states, given by Eq. (3.6) (left axis). The number of particles involved in the transition state $k^\ddagger$ (right axis) increases with σ in a staircase-manner. The corresponding steps are determined by Eq. (3.7) and occur at particle sizes where lines for different generation rates ϖ_k intersect (marked by crosses).

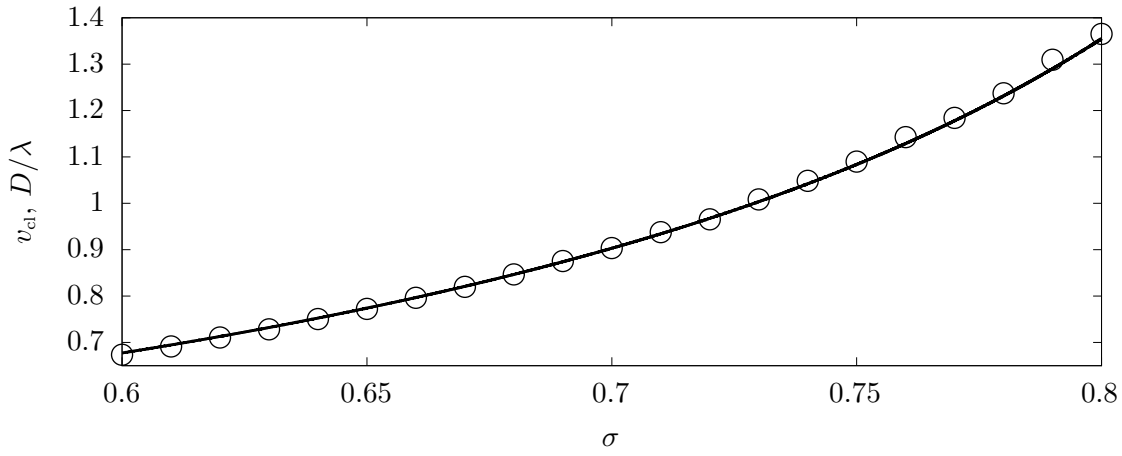

Figure 3.6: Velocity of propagating clusters for different particle sizes, obtained by simulations (circles) and predicted by Eq. (3.9) with $\alpha = 1.35$ (solid line).

same structure as the thermally activated one (n particles occupy $(n-1)$ potential wells and propagate in a crystalline-like structure), and the cluster velocity is identical for both cluster types [138]. In what follows, we consider crowding-induced clusters to determine the cluster velocity.

Results for v_{cl}, depending on σ, are presented in Fig. 3.6. On the contrary to cluster generation rate, the dependence of v_{cl} on particle size is much weaker, increasing by only a factor of about 1.5 compared to the decrease in ϖ_{gen} by more than three orders of magnitude, as the particle size changes from $\sigma = 0.6$ to 0.75. The corresponding increase in cluster velocity with particle size can also be observed in Fig. 3.4.

Another remarkable feature is that the magnitude of v_{cl} is much larger than the velocity of independent particles, which is $v_0 \cong 8.4 \times 10^{-3} D/\lambda$ for the given parameters U_0 and f, see Eq. (2.36). Moreover, it is also much larger even than the velocity of independent particles in flat potential, $\mu f = 0.2 D/\lambda$.

To estimate the velocity of n-cluster analytically, we consider a state with the first, i.e. leftmost particle at the stable mechanical equilibrium as an initial position. When the second particle reaches a point of stable mechanical equilibrium during the propagation, we can state that the cluster is shifted by one wavelength, since the second particle is now taking the role of the first one in the initial position.

As particles in the cluster propagate nearly in contact with each other, see Fig. 3.2(b), its center follows a Brownian motion in a tilted cosine potential with the same wavelength λ

and drag force f, but with the reduced amplitude $(U_0/n)\sin(n\pi\sigma)/\sin(\pi\sigma)$ of the external potential [140]. The mathematical justification for this factor will be provided in Sec. 3.3.1. For the considered particle sizes, the number of particles in a cluster is $n \geq 3$, see Fig. 3.5(b) and Eq. (3.3), so the amplitude of the reduced potential is an order of $k_\mathrm{B}T$. The forces due to this potential can thus be neglected, since they alternate in sign, and the mean velocity of a single particle in a cluster is then estimated as $\alpha\mu f$, where α is a dimensionless coefficient of order unity resulting from the neglect of the potential.

While the cluster covers the distance of one wavelength, a particle in the cluster shifts by only $\lambda - \varsigma$. The mean time of a particle to cover this distance is $(\lambda - \varsigma)/(\alpha\mu f)$, and we hence obtain

$$v_\mathrm{cl} = \lambda \left(\frac{\lambda - \varsigma}{\alpha\mu f} \right)^{-1} = \frac{\alpha\mu f}{1 - \sigma}. \tag{3.9}$$

This formula with $\alpha = 1.35$ gives almost perfect agreement with the simulation data, see Fig. 3.6.

The concept of a soliton

Since the moving clusters are essentially density waves whose propagation occurs without dispersion, in what follows we refer to propagating clusters as *Brownian solitons*. The occurrence of these solitons is a rather unexpected effect. Solitons are commonly known in systems with inertia as waves that propagate without dispersion due to nonlinear effects, e.g. in the classical Frenkel-Kontorova model [141]. In the BASEP neither inertia nor nonlinearity are presented.

To avoid further confusion, we want to note separately that Brownian solitons and clusters in BASEP are two different designations for the same phenomenon, and the application of these terms depends on the context. Therefore, when referring to the clustering of particles, we use the term “cluster”, whereas when discussing its propagation, we apply the term “soliton”.

3.2.3 Soliton-mediated current

Let us now consider the thermodynamic limit $L \to \infty$, where the thermally activated clusters are constantly being generated and recombined. Recombination of a cluster occurs when it encounters an empty potential well on the way of its propagation. The mean lifetime of a cluster τ is thereby $\tau = d_\mathrm{e}/v_\mathrm{cl}$, where d_e is the mean distance between empty potential wells. It can be defined via number density of empty potential wells ρ as

$d_e = 1/\rho$. Taking into account that the number of potential wells is equal to the number of clusters, we can write a differential equation describing the behavior of ρ over time,

$$\frac{d\rho}{dt} = \frac{\varpi_{gen}}{\lambda} - \frac{\rho}{\tau}. \tag{3.10}$$

Its stationary solution gives $\rho_{st} = \varpi_{gen}\tau/\lambda = \varpi_{gen}/\lambda\rho_{st}v_{cl}$, so that $\rho_{st} = \sqrt{\varpi_{gen}/\lambda v_{cl}}$. Since during the cluster lifetime each particle located between the positions of cluster generation and recombination shifts by one wavelength, the stationary current in the system equals $j_{st}^{\infty} = 1/\tau_{st}$, where ∞ in the upper index corresponds to the thermodynamic limit. In terms of ϖ_{gen} and v_{cl}, it reads

$$j_{st}^{\infty} = \rho_{st}v_{cl} = \sqrt{\frac{\varpi_{gen}v_{cl}}{\lambda}}. \tag{3.11}$$

These results for the thermodynamic limit, included in Fig. 3.1(a), are shown in Fig. 3.7. As we can observe, the shape of current-density curve matches the initial AZMIF prediction. Thus, the decrease of current by several orders of magnitude, observed for $L = 20\lambda$ and $L = 100\lambda$ in Figs. 3.1(a) and 3.7, is indeed a finite size effect.

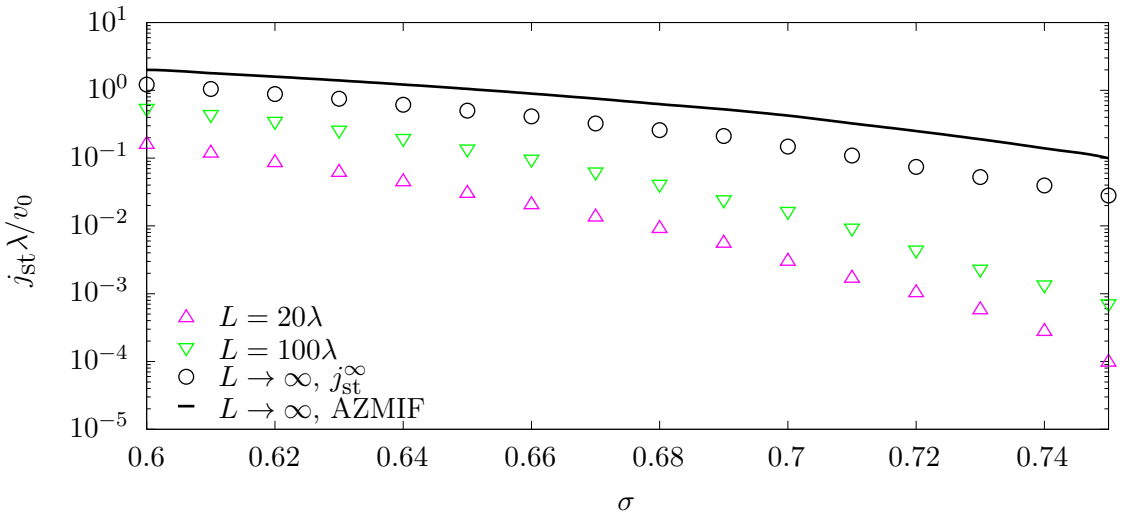

Figure 3.7: The data of Fig. 3.1 with the inclusion of theoretical results from Eq. (3.11) (black circles) with ϖ_{gen} and v_{cl} from the simulation results. Even though the initial prediction of current in the thermodynamic limit by the AZMIF appeared to be not exactly precise, it nonetheless provides the correct magnitude order and shape of the current-density curve.

As was mentioned in the introduction of the present chapter (Sec. 3.1), for large system length L it is problematic to perform the Brownian dynamics simulations due to large computational time. To overcome this problem, we introduce a course-grained model of the cluster dynamics. In this model, we have two types of objects: particles which correspond to thermally activated clusters in the BASEP, and holes corresponding to empty potential wells. Either particle or hole can occupy a lattice site, and the double occupancy is prohibited. A lattice site can also remain unoccupied. Holes are considered to be stationary since their velocity, equivalent to that of non-interacting particles v_0, is much less than the velocity of clusters v_{cl}. The latter, normalized to the wavelength, denotes the rate v_{cl}/λ with which a particle can jump (propagate) to a right-neighboring lattice site. If this lattice site is already occupied by a hole, the particle and hole recombine, leaving the site unoccupied. Holes and particles are generated in pairs with the rate ϖ_{gen} at nearest-neighbor unoccupied sites. The illustration of all possible processes in this model is given in Fig. 3.8. Such model can be considered as a version of the two-species totally asymmetric simple exclusion process [142, 143], with particle-hole generation and recombination as specific features of the considered model.

To calculate the current in the course-grained model, we count the number of particle jumps per time. Thus, both length and current are given in wavelength units. These results are in a good agreement with the corresponding BASEP results for $L \leq 10^3\lambda$, as is

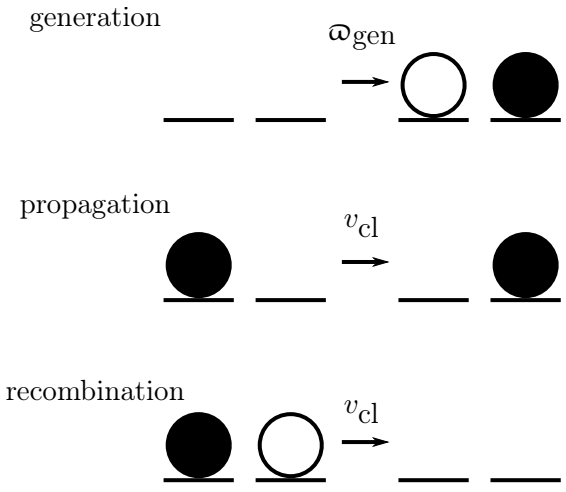

Figure 3.8: All possible elementary processes taking place in the considered model.

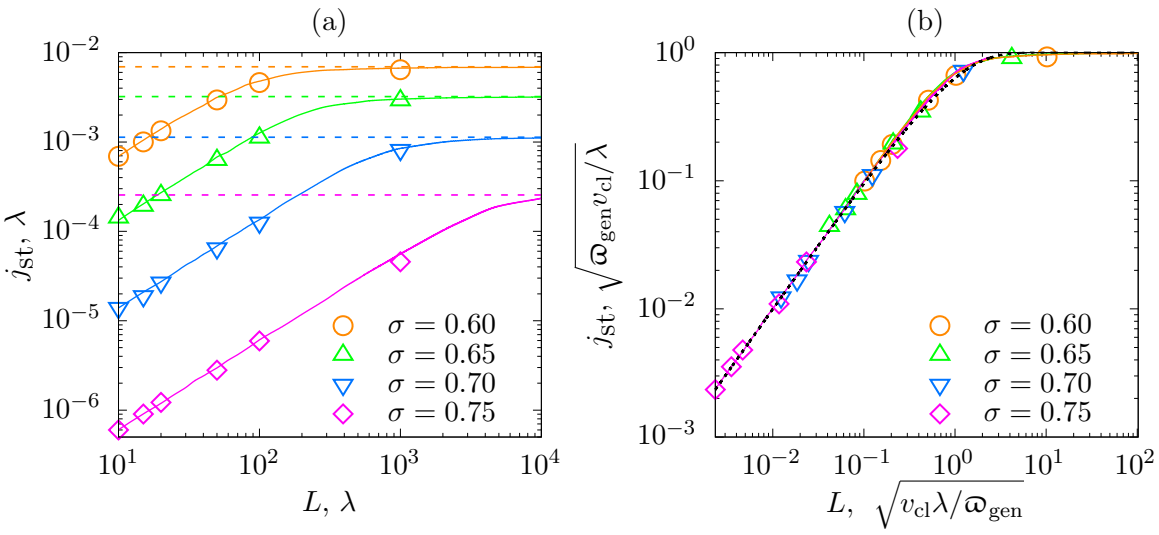

Figure 3.9: (a) Dependence of the current j_{st} on the system size L for particle sizes $\sigma = 0.6,\ 0.65,\ 0.7,\ 0.75$. The results of Brownian dynamics simulations (symbols) are in a good agreement with ones from kinetic Monte Carlo simulations of the introduced coarse-grained model (solid lines). For large system size current approaches the theoretically predicted value j_{st}^{∞} given by Eq. (3.11) (dashed horizontal lines). In panel (b) we scale both current and system size to demonstrate that the data collapse onto a general master curve $G(.)$ given by Eq. (3.13) (dashed line).

shown in Fig. 3.9(a)[1]. Thus, the course-grained model allows us to reveal the dependence of current on the system length L. For $L \lesssim 1/\rho_{st}$, the current is proportional to the system length, $j_{st} \simeq \varpi_{gen} L/\lambda$, since the overall cluster generation rate is low. Herewith, the characteristic length $1/\rho_{st}$ has the following meaning: for a system of this size, the time-averaged number of clusters in the system is one. For $L \gg 1/\rho_{st}$, the current approaches the thermodynamic limit value j_{st}^{∞}, determined in Eq. (3.11).

The scaling behavior of particle currents can be seen in Fig. 3.9(b), with the following scaling form introduced:

$$j_{st}(\sigma, L) = \sqrt{\frac{\varpi_{gen} v_{cl}}{\lambda}}\, G\left(\sqrt{\frac{\varpi_{gen}}{v_{cl}\lambda}} L\right), \tag{3.12}$$

where $v_{cl}\lambda/\varpi_{gen} = 1/\rho_{st}$. The scaled curves in Fig. 3.9(b) converge to the master curve $G(x)$, which must have $G(x) \to x$ for $x \to 0$ as the current j_{st} is linear on the system

[1]The system length limit is chosen due to large computational time already for $L = 10^3\lambda$. For example, the CPU time to obtain a single value j_{st} for $\sigma = 0.75$ is about 3000 hours on a 16-core Intel Xeon Nehalem 2.66 GHz processor.

length for small L, and $G(x) \to 1$ for $x \to \infty$, thereby reaching the thermodynamic limit value. A simple exponential form of the scaling function

$$G(x) = 1 - e^{-x}, \tag{3.13}$$

satisfying both these conditions and having a good agreement with the simulation results, is shown in Fig. 3.9(b) as the dashed line.

3.3 Solitons (clusters) in the overcrowded systems

To study the dynamics of crowding-induced clusters occurring in overcrowded systems, we use the same setup that we introduced for calculating cluster velocity in Sec. 3.2.2, namely: N particles occupy $N-1$ potential wells, where N should be small enough to neglect the impact of thermally activated clusters. For calculations, in this section we set $N = 21$ and system length $L = 20\lambda$.

Crowding-induced clusters have two features that distinguish them from thermally activated ones. First, since the presence of such cluster is not accompanied by the appearance of an empty potential well, it has no recombination mechanism, hence its motion in the system is permanent. Secondly, crowding-induced clusters can also exist at low temperatures, where collective excitations leading to the formation of thermally activated clusters are practically impossible. For the small drag force $f\lambda/U_0 \ll 1$, when a single particle would rarely traverse a potential barrier, the measurable particle current induced by crowding-induced clusters is present around particle sizes

$$\sigma_n = \frac{n-1}{n},\ n = 2, 3, \ldots, \tag{3.14}$$

and has peaks at these values even at low temperature. The temperature can also be interpreted as the strength of the thermal noise, where low temperatures correspond to weak noise and high temperatures correspond to strong noise.

Particle currents for the weak noise $k_\mathrm{B}T/U_0 = 0.01$ and small drag force $f\lambda/U_0 = 0.05$ are shown in Fig. 3.10(a), and the initial conditions used in the numerical simulations are shown in Fig. 3.10(b). The particles in this setup are equidistant which is motivated by the possible experimental realization of the overcrowded system: first, we consider the same number of particles and potential wells, see Fig. 3.1(b). Then we change the wavelength of the external potential in order to remove one optical trap from the system, thereby creating overcrowding.

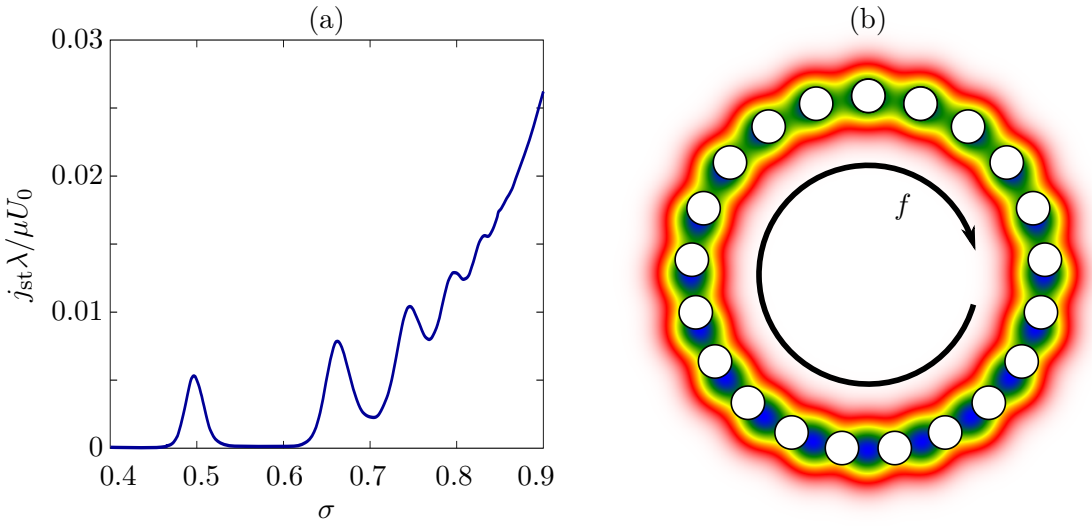

Figure 3.10: (a) Stationary current as a function of σ for small drag force $f\lambda/U_0 = 0.05$ and weak noise strength $k_{\mathrm{B}}T/U_0 = 0.01$. Even in the weak noise limit and small drag force, the soliton-induced current (propagating state) in the system is present in the form of peaks at values $\sigma_n = (n-1)/n,\ n = 2, 3, \ldots$. (b) An experimental realization of the model [74, 108] for $N = 21$, $L = 20\lambda$ and $\sigma = 0.6\lambda$: rings of 20 optical traps filled with 21 hard spheres in a fluid environment. Color map is identical to one in Fig. 3.1, and the drag force f drives hard spheres in the clockwise direction.

Observation of Fig. 3.10(a) leads to the following questions: (i) how does the formation of clusters and their behavior depend on the particle size and drag force, and (ii) what is the physical meaning of those σ_n values. To address these questions, in the following subsection we consider a reference model of the zero-noise limit ($k_{\mathrm{B}}T = 0$).

3.3.1 Reference model: zero-noise limit

The advantage of such model is the determinacy of particle motion and, consequently, the possibility of its analytical description. For independent particles, the time evolution (2.1) takes the form

$$\frac{\mathrm{d}x_i}{\mathrm{d}t} = \dot{x}_i = u(x_i), \tag{3.15a}$$

where

$$u(x) = \mu\left(f - U'(x)\right). \tag{3.15b}$$

To describe the interaction between hard particles, we operate with the term “cluster” as is presented in Sec. 3.1, which in the zero-noise limit has also a clear definition: an n-cluster

is a set of n particles mutually being in contact and propagating as one entity[2]. Therefore, at given time all particles in a cluster should have the same velocity $\dot{x}_1 = \ldots \dot{x}_n = \bar{u}_n$.

The conditions for cluster merging and fragmentation are determined by the hardcore interactions and rely on Newton's third law of motion, i.e. action-reaction principle [144], applied for the pair interaction force $f^{(2)}(x_i, x_{i+1}) = f^{(2)}_{i,i+1}$:

$$f^{(2)}_{i,i+1} = -f^{(2)}_{i+1,i}. \tag{3.16}$$

The presence of interaction between particles is given by the condition of positive pair interaction force between all particle pairs in n-cluster,

$$f^{(2)}_{i,i+1} > 0. \tag{3.17a}$$

with the following equations of motion

$$\begin{aligned}
\bar{u}_n &= u_1 - \mu f^{(2)}_{12}, && (3.17b)\\
\bar{u}_n &= u_i - \mu f^{(2)}_{i,i+1} + \mu f^{(2)}_{i-1,i}, \quad i = 2, \ldots, n-1, && (3.17c)\\
\bar{u}_n &= u_n + \mu f^{(2)}_{n-1,n}. && (3.17d)
\end{aligned}$$

where $u(x_i) = u_i$. System of equations (3.17b)-(3.17d) is exactly determined and consistent (n linear equations for determining $(n-1)$ pair interaction forces and cluster velocity u), so it has the unique solution:

$$\begin{aligned}
f^{(2)}_{i,i+1} &= \frac{n-i}{\mu n}\sum_{j=1}^{i} u_j - \frac{i}{\mu n}\sum_{j=i+1}^{n} u_j, \quad i = 1, \ldots, n-1, && (3.18a)\\
\bar{u}_n &= \frac{1}{n}\sum_{i=1}^{n} u_i. && (3.18b)
\end{aligned}$$

This solution, together with the condition (3.17a) is necessary and sufficient for n particles being mutually in contact to form a cluster. If the solution (3.18a) violates the condition (3.17a), it means that the considered particles propagate further not as one entity, but as independent n_1-,$\ldots, n_s$-clusters, with $\sum_{i=1}^{s} n_i = n$ and clusters are numbered from left to right in ascending index order. The condition of independence implies that each cluster n_i must have a lower velocity than the right-neighboring cluster n_{i+1}, but higher than the left-neighboring cluster n_{i-1}. For n_1-cluster and n_s-cluster, there is no

[2] A single particle is considered as 1-cluster.

condition with respect to a neighboring cluster to the left and right, respectively. The condition for independent propagation of particles being in contact as n_1-, ..., n_s-clusters can thus be written as

$$\bar{u}_{n_1} < \bar{u}_{n_2} < \ldots < \bar{u}_{n_s}, \tag{3.19}$$

with clusters' velocities $\bar{u}_{n_1}, \ldots, \bar{u}_{n_s}$ are determined for each cluster independently from Eq. (3.18b).

For the particular cosine potential (2.4), pair interaction forces have the following form:

$$\begin{aligned} f^{(2)}_{i,i+1} &= \frac{n-i}{n} \sum_{j=1}^{i} \left(f + \frac{\pi U_0}{\lambda} \sin[2\pi x_j/\lambda] \right) - \frac{i}{n} \sum_{j=i+1}^{n} \left(f + \frac{\pi U_0}{\lambda} \sin[2\pi x_j/\lambda] \right) \\ &= \frac{\pi U_0}{n\lambda} \left((n-i) \sum_{j=0}^{i-1} \sin[2\pi(x_1 + j\varsigma)/\lambda] - i \sum_{j=i}^{n-1} \sin[2\pi(x_1 + j\varsigma)/\lambda] \right). \end{aligned} \tag{3.20}$$

Thus, we have the following condition for an n-cluster to be stable:

$$\inf_{i=1,\ldots,n-1} \left[(n-i) \sum_{j=0}^{i-1} \sin[2\pi(x + j\varsigma)/\lambda] - i \sum_{j=i}^{n-1} \sin[2\pi(x + j\varsigma)/\lambda] \right] > 0, \tag{3.21a}$$

where x is the position of leftmost particle in the cluster. According to Eqs. (3.18b) and (3.15b), the cluster has the velocity

$$\bar{u}_n(x) = \mu \left[f + \frac{\pi U_0}{\lambda} \frac{\sin(\pi n\sigma)}{n \sin(\pi\sigma)} \sin\left(\frac{2\pi x}{\lambda} + \pi(n-1)\sigma \right) \right]. \tag{3.21b}$$

Presence of the reduction factor $(U_0/n)\sin(n\pi\sigma)/\sin(\pi\sigma)$ in the sinusoidal term, which we have already specified in Sec. 3.2.2, allows particles in the cluster to propagate even in the zero-noise limit, while individual particles cannot surmount the potential barrier[3]. For particle sizes σ_n given by Eq. (3.14), the potential barrier vanishes, which explains the presence of peaks observed in Fig. 3.10(a).

Since we have fully described the principles of system evolution, we can analytically evaluate its main parameters in the propagating state. In order to do this, we introduce an event-driven scheme, in which we describe state of the system only at the moment of cluster merging or fragmentation. Here we use the fact that for an independent cluster, i.e. for a cluster that does not merge with others and does not undergo fragmentation at

[3]In fact, the derivation of this formula is nothing else but a mathematical justification for the barrier reduction effect described in Chapter 2.

the considered period of time $[t_a; t_b]$, its position x_b at time t_b depends only on its position x_a at time t_a. By integrating the equation of motion (3.15a) with the cluster velocity given by Eq. (3.21b), we thus obtain:

$$t_b - t_a = \int_{x_a}^{x_b} \frac{\mathrm{d}x}{\bar{u}_n(x)} \tag{3.22a}$$

$$= \begin{cases} \dfrac{\lambda \mathcal{A}_n}{\mu\pi} \left\{ \arctan\left[\mathcal{A}_n \left(\dfrac{\pi U_0 \sin(\pi n\sigma)}{\lambda n \sin(\pi\sigma)} + f \tan\left[\dfrac{\pi x}{\lambda} + \dfrac{\pi(n-1)\sigma}{2} \right] \right) \right] \right\} \Bigg|_{x_a}^{x_b}, \\ \qquad\qquad f^2\lambda^2 n^2 \sin^2(\pi\sigma) > \pi^2 U_0^2 \sin^2(\pi n\sigma); \\ -\dfrac{\lambda \mathcal{A}_n}{\mu\pi} \left\{ \operatorname{artanh}\left[\mathcal{A}_n \left(\dfrac{\pi U_0 \sin(\pi n\sigma)}{\lambda n \sin(\pi\sigma)} + f \tan\left[\dfrac{\pi x}{\lambda} + \dfrac{\pi(n-1)\sigma}{2} \right] \right) \right] \right\} \Bigg|_{x_a}^{x_b}, \\ \qquad\qquad f^2\lambda^2 n^2 \sin^2(\pi\sigma) < \pi^2 U_0^2 \sin^2(\pi n\sigma); \\ \dfrac{\lambda}{f\pi\mu \left[1 + \cot(\frac{\pi x}{\lambda} + \frac{\pi(n-1)\sigma}{2}) \right]} \Bigg|_{x_a}^{x_b}, \qquad f^2\lambda^2 n^2 \sin^2(\pi\sigma) = \pi^2 U_0^2 \sin^2(\pi n\sigma), \end{cases}$$

where $\mathcal{A}_n$ is

$$\mathcal{A}_n = \sqrt{\frac{\lambda^2 n^2 \sin^2(\pi\sigma)}{\left| f^2\lambda^2 n^2 \sin^2(\pi\sigma) - \pi^2 U_0^2 \sin^2(\pi n\sigma) \right|}}\,. \tag{3.22b}$$

For the considered undercritical regime, if there is no further cluster fragmentation or merging, the system is in a jammed state, i.e. it does not imply any motion.

In the initial system setup, all potential wells but one are occupied by single particles, and the remaining one is occupied by two particles. This setup is natural for description of real systems [108], and satisfies the cluster overcrowding condition that an n-cluster occupies $(n-1)$ potential wells. All single particles quickly relax near the stable equilibria positions, hence the presence of dynamics in the system depends on fact whether the two particles in the same potential well can initiate the soliton propagation in the system.

In case of propagating state, after a short transient time the system establishes a periodic sequence of solitons. The phase diagram of these propagating sequences in (f, σ) plane is shown in Fig. 3.11. As it can be seen, only two types of solitons are possible: type $(n+1)$-n, where the size of a propagating cluster periodically changes from $(n+1)$ to n, and type $(n+1)$-n-$(n+1)$-$(n+2)$ where the propagating cluster has size changes $(n+1) \to n \to (n+1) \to (n+2)$ within one period. The soliton periodicity is the same as that for the

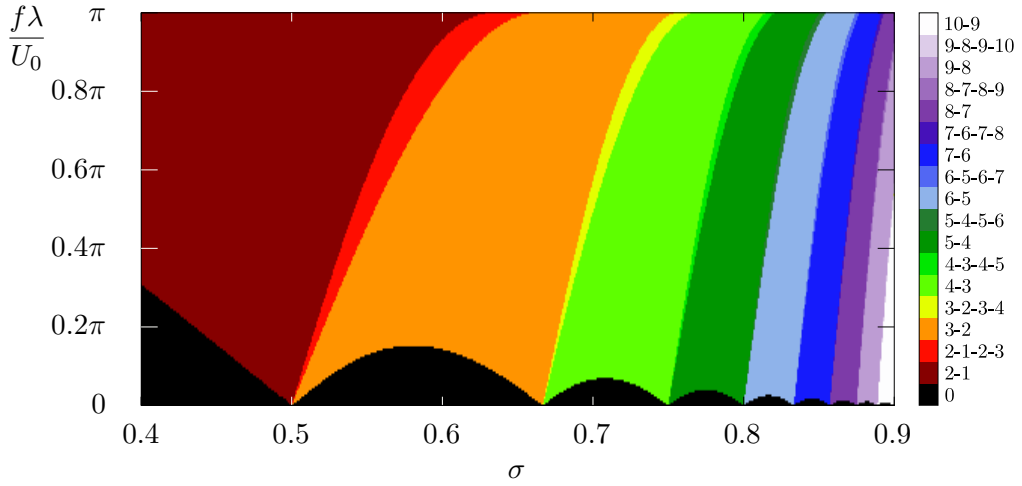

Figure 3.11: Phase diagram of possible soliton types in the plane (f, σ). Drag force is normalized, so that $f\lambda/U_0 = \pi$ corresponds to the critical tilting force. The soliton type 0 (black) corresponds to the jammed state without any dynamics in the system.

external potential, and $n \geq 1$ is defined as a soliton core size [108, 145]. In what follows we refer to them as solitons of type A and B, respectively.

For both types of solitons, only two kinds of events occur: (i) collision between soliton and a single particle, and (ii) detachment of the leftmost particle from the soliton. Knowing these events and their sequence within a period, we can solve the event-driven dynamics analytically. In what follows, we denote these events with the coordinate x_α^k of the leftmost particle in a soliton. Subscript $\alpha = \{\mathrm{A}; \mathrm{B}\}$ denotes a soliton type, and superscript k denotes an event number in the period, where $k = \{1; 2\}$ for solitons of type A, and $k = \{1; 2; 3; 4\}$ for solitons of type B).

As a first event we consider detachment of the leftmost particle from the $(n+1)$-soliton, which is the case for both types of solitons. At the detachment moment, particles of a the soliton have coordinates $x_\alpha^1, x_\alpha^1 + \varsigma, \ldots, x_\alpha^1 + n\varsigma$. Condition $f_{12} = 0$ for the detachment of the leftmost particle in Eq. (3.20) then reads:

$$\begin{aligned} f + \frac{\pi U_0}{\lambda} \sin\left(\frac{2\pi x_\alpha^1}{\lambda}\right) &= f + \frac{\pi U_0}{\lambda n} \sum_{k=1}^{n} \sin\left(\frac{2\pi(x_\alpha^1 + k\varsigma)}{\lambda}\right) \\ &= f + \frac{\pi U_0 \sin(\pi n\sigma)}{\lambda n \sin(\pi\sigma)} \sin\left[\frac{2\pi x_\alpha^1}{\lambda} + \pi(n+1)\sigma\right]. \end{aligned} \tag{3.23}$$

Solution of this equation yields:

$$x_\alpha^1 = -\frac{\lambda}{2} + \frac{\lambda}{2\pi}\operatorname{arccot}\left[\frac{n\sin(\pi\sigma)}{\sin(\pi n\sigma)\sin(\pi(n+1)\sigma)} - \cot(\pi(n+1)\sigma)\right] + m\lambda, \qquad m = 1,\dots,N, \tag{3.24}$$

where $\operatorname{arccot}(z) \in]0,\pi/2]$ for $z \geq 0$ and $\operatorname{arccot}(z) \in]-\pi/2,0[$ for $z < 0$.

Without limiting generality we take the coordinate origin so that $m = 1$:

$$x_\mathrm{A}^1 = x_\mathrm{B}^1 = \frac{\lambda}{2} + \frac{\lambda}{2\pi}\operatorname{arccot}\left[\frac{n\sin(\pi\sigma)}{\sin(\pi n\sigma)\sin(\pi(n+1)\sigma)} - \cot(\pi(n+1)\sigma)\right]. \tag{3.25}$$

The second event is also identical for both types of solitons: the n-soliton attaches to the next particle at position in the direction of the soliton propagation. We consider this particle as resting in the position of stable equilibrium $x_p^{\min}$, but in fact in overdamped dynamics a particle is never exactly at this position, but only relaxes towards it at an exponential rate [10]. The proposed assumption of our analytical approach is valid for situations where the characteristic relaxation time towards the stable equilibrium position is much shorter than the time L/v_sol of the soliton propagation through the system. This condition is satisfied when the drag force is small ($f \ll \pi U_0/\lambda$) and/or when the system size is much larger than the cluster size ($L \gg n\lambda$).

The choice of p of the stable equilibrium position $x_p^{\min}$ is conditioned by the requirement that the resting particle must be the leftmost one, satisfying the condition of not belonging to an n-soliton at the moment of the first event:

$$p = \underset{p'}{\operatorname{argmin}}\left\{x_{p'}^{\min} > x_\mathrm{A}^1 + (n+1)\varsigma\right\} = n+1. \tag{3.26}$$

with $p' = (n+1)$ as the only solution satisfying the cluster overcrowding condition that an n-cluster occupies $(n-1)$ potential wells. In case $p' > (n+1)$, an n-cluster could not reach the next particle, because its particles are localized near the positions $x_1^{\min}, x_2^{\min}, \dots, x_n^{\min}$. In case $p' \leq n$, we would locally violate the cluster overcrowding condition, since in such case we have $(n+1)$ particles in $(p'-1) \leq (n-1)$ potential wells.

By utilizing condition (3.26) and using the fact that n uniquely depends on the parameters f and σ, we obtain the condition determining soliton core size:

$$n = \underset{p'}{\operatorname{argmin}}\left\{x_{p'+1}^{\min} > x_\mathrm{A}^1(p') + (p'+1)\varsigma\right\}. \tag{3.27}$$

Accordingly, in the second event we have the leftmost particle at position

$$x_{\mathrm{A}}^2 = x_{\mathrm{B}}^2 = x_{n+1}^{\min} - n\varsigma. \tag{3.28}$$

Further, the soliton behavior for each type starts to be different. The reason for this difference is as follows: the position of the first event x_{A}^1 is located on the left to the stable mechanical equilibrium $x_1^{\min}$ within the same potential well. Consequently, a particle that becomes separated after the first event continues to move. As the n-soliton slows down its motion after contact with a resting particle (second event), this may allow the previously separated particle to reunite with the main soliton. Depending on the occurrence of this event, we obtain either type A soliton (the particle does not reunite with the main soliton) or type B soliton (the particle reunites with the main soliton). In type A soliton, following the second event, the $(n+1)$-soliton initiates its motion until the subsequent event, which involves the detachment of the leftmost particle positioned at $x_{\mathrm{A}}^1 + \lambda$. This detachment event completes the main sequence of soliton type A propagation. Times of motion as n- and $(n+1)$-solitons for type A then are

$$\tau_n^{\mathrm{A}} = \int_{x_{\mathrm{A}}^1+\varsigma}^{x_{\mathrm{A}}^2} \frac{\mathrm{d}x}{\bar{u}_n(x)}, \tag{3.29a}$$

$$\tau_{n+1}^{\mathrm{A}} = \int_{x_{\mathrm{A}}^2}^{x_{\mathrm{A}}^1+\lambda} \frac{\mathrm{d}x}{\bar{u}_{n+1}(x)}. \tag{3.29b}$$

In Equations (3.29a) and (3.29b) we have taken into account, that when a particle is detached (joined) from the left, the position of the leftmost particle in the soliton increases (decreases) by ς.

For type B, the third event involves the catchup of the $(n+1)$-soliton by the previously detached particle. This event is determined by a condition that the detached particle and the main soliton cover an equal distance during the time span between the first and third events:

$$\int_{x_{\mathrm{B}}^1+\varsigma}^{x_{\mathrm{B}}^2} \frac{\mathrm{d}x}{\bar{u}_n(x)} + \int_{x_{\mathrm{B}}^2}^{x_{\mathrm{B}}^3} \frac{\mathrm{d}x}{\bar{u}_{n+1}(x)} = \int_{x_{\mathrm{B}}^1}^{x_{\mathrm{B}}^3-\varsigma} \frac{\mathrm{d}x}{\bar{u}_1(x)}. \tag{3.30}$$

Since this event does not occur for soliton type A, the existence of a solution in Eq. (3.30) thus specifies the type of soliton.

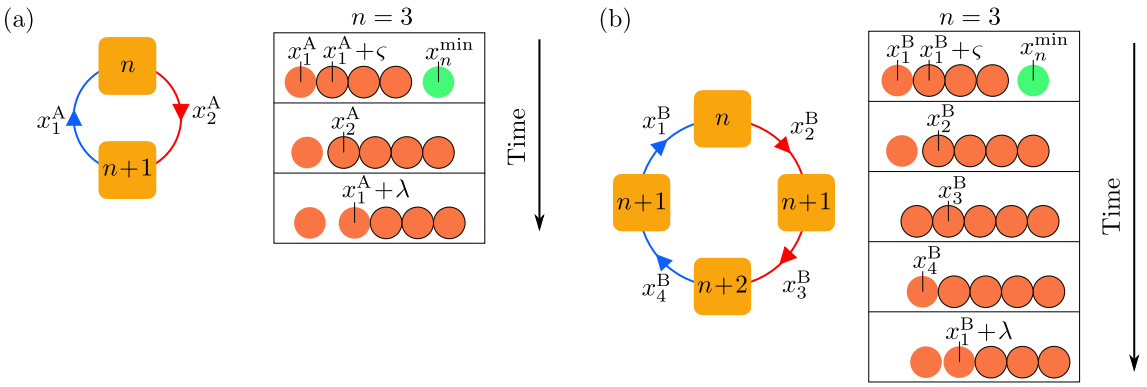

Figure 3.12: Illustration of events for soliton types, with (a) for soliton type A, and (b) for soliton type B. Red arrows in the soliton sequence (shown as a circle) represent particle attachment, and blue arrows represent particle detachment. In the frame, particles in soliton are circled in black, and the resting particle is highlighted in green.

Shortly after creation of $(n+2)$-soliton, the leftmost particle detaches again, this time for good. Condition for this event is analogous to Eq. (3.25) with the adjusted soliton size:

$$x_{\mathrm{B}}^4 = \frac{\lambda}{2} + \frac{\lambda}{2\pi} \operatorname{arccot}\left[\frac{(n+1)\sin(\pi\sigma)}{\sin(\pi(n+1)\sigma)\sin(\pi(n+2)\sigma)} - \cot(\pi(n+2)\sigma)\right]. \tag{3.31}$$

Times of motion as n-, $(n+1)$- and $(n+2)$-solitons for type B then are given by the formulas:

$$\tau_n^{\mathrm{B}} = \int_{x_{\mathrm{B}}^1+\varsigma}^{x_{\mathrm{B}}^2} \frac{\mathrm{d}x}{\bar{u}_n(x)}, \tag{3.32a}$$

$$\tau_{n+1}^{\mathrm{B}} = \int_{x_{\mathrm{B}}^2}^{x_{\mathrm{B}}^3} \frac{\mathrm{d}x}{\bar{u}_{n+1}(x)} + \int_{x_{\mathrm{B}}^4+\varsigma}^{x_{\mathrm{B}}^1+\lambda} \frac{\mathrm{d}x}{\bar{u}_{n+1}(x)}, \tag{3.32b}$$

$$\tau_{n+2}^{\mathrm{B}} = \int_{x_{\mathrm{B}}^3-\varsigma}^{x_{\mathrm{B}}^4} \frac{\mathrm{d}x}{\bar{u}_{n+2}(x)}. \tag{3.32c}$$

A visual representation of the sequence of all events for both soliton types is presented in Fig. 3.12. Knowing the time intervals between these events, we can calculate the mean velocity of solitons:

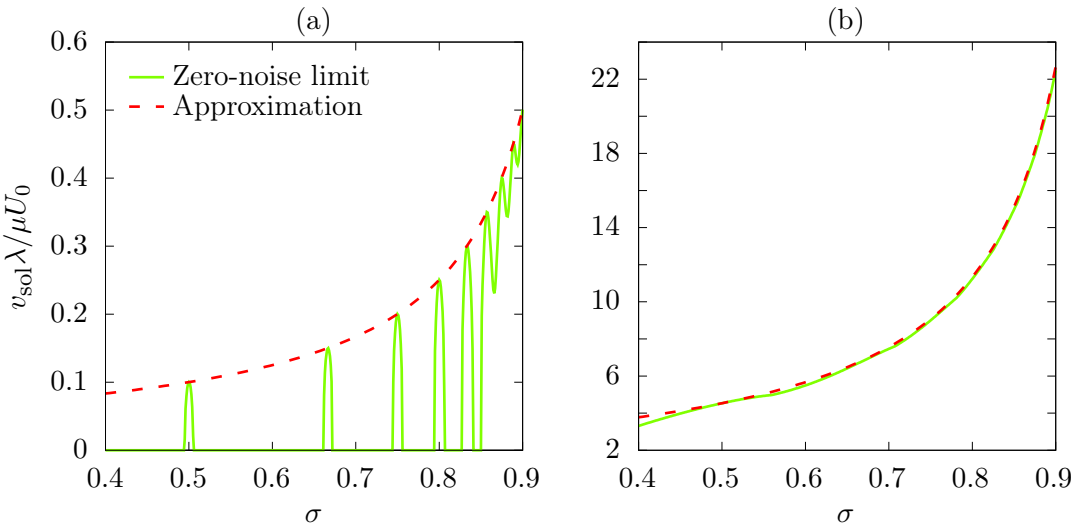

Figure 3.13: Soliton velocity in the zero-noise limit in dependence of σ for (a) $f\lambda/U_0 = 0.05$ and (b) $f\lambda/U_0 = 2.1$ (green solid lines). The approximation (dashed-red lines) is given by Eq. (3.9) with $\alpha = 1$ for (a) and $\alpha = 1.08$ for (b).

$$v_{\rm sol}^{\rm A} = \frac{\lambda}{\tau_n^{\rm A} + \tau_{n+1}^{\rm A}}, \tag{3.33a}$$

$$v_{\rm sol}^{\rm B} = \frac{\lambda}{\tau_n^{\rm B} + \tau_{n+1}^{\rm B} + \tau_{n+2}^{\rm B}}. \tag{3.33b}$$

Corresponding results for small drag force, $f\lambda/U_0 = 0.05$ and big drag force, $f\lambda/U_0 = 2.1$ are shown in Fig. 3.13. Remarkably, in the case of strong drag force, the soliton velocity can be approximated by Eq. (3.9) intuitively derived in the Sec. 3.2.2, while for the weak driving force this approximation works for the velocity peaks.

Since each soliton passage of the system corresponds to a shift of all particles by one potential well in the direction of the drag force, the particle current reads:

$$j_{\rm st} = \frac{v_{\rm sol}}{L}. \tag{3.34}$$

In the next section, we use these analytical results for the zero-noise limit when considering the system in the presence of noise.

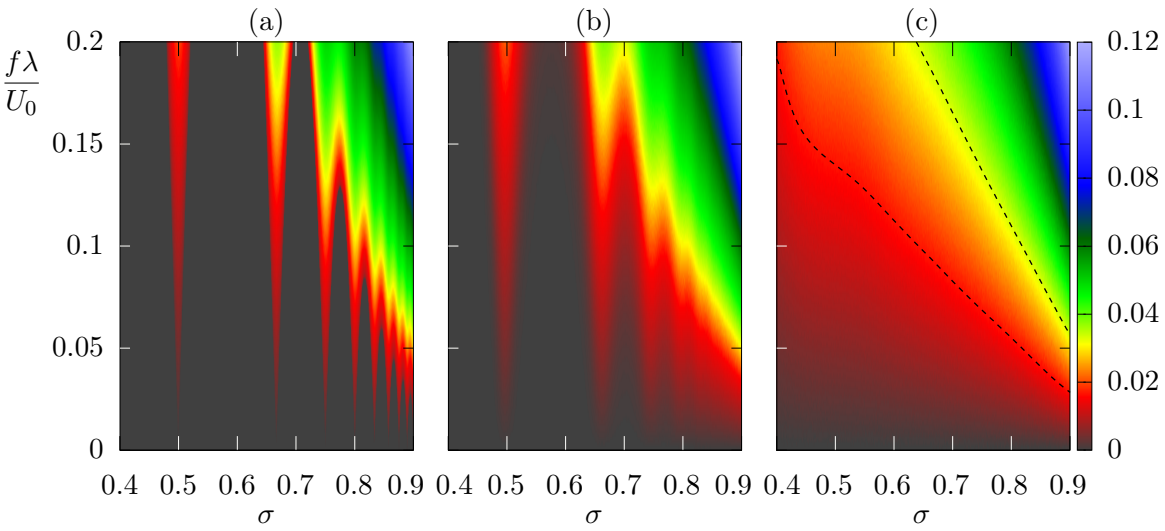

Figure 3.14: Current j_{st} as a function of particle size σ and drag force f in a color-coded representation for different noise strengths: (a) $k_{\mathrm{B}}T = 0$ (zero noise), (b) $k_{\mathrm{B}}T = 0.01U_0$ (weak noise) and (c) $k_{\mathrm{B}}T = 0.1U_0$ (strong noise). Current values in colorbox are given in units of $\mu U_0/\lambda^2$, and dashed lines in panel (c) are isolines of constant currents for $j_{\mathrm{st}} = 0.1\lambda^2/\mu U_0$ and $j_{\mathrm{st}} = 0.2\lambda^2/\mu U_0$.

3.3.2 Systems with thermal noise

Current diagrams as function of (f, σ) for three representative cases, $k_{\mathrm{B}}T = 0$ (zero noise), $k_{\mathrm{B}}T = 0.01U_0$ (weak noise) and $k_{\mathrm{B}}T = 0.1U_0$ (strong noise) are shown in Fig. 3.14. These diagrams show how the system changes between jammed (dark-grey) and running (color) states in dependence of particle size and drag force.

The key point for the explanation of current diagrams is the effective potential for propagating clusters, $(U_0/n)\sin(n\pi\sigma)/\sin(\pi\sigma)$. For the zero-noise limit and small drag force, particle currents can occur only near sizes σ_n given by Eq. (3.14), which is the reason for current peaks in Fig. 3.13(a) and for running states in Fig. 3.14(a). As the noise and drag force increases, these peaks and running states become broader, since thermal activation is sufficient for the cluster to start moving even when the potential does not vanish but is only reduced by the cluster motion and the drag force. The corresponding broadening of peaks and running zones is shown in Figs. 3.10(a) and 3.14(b), respectively. The width of these zones expands as a result of the reduced effective external potential $(U_0/n)\sin(n\pi\sigma)/\sin(\pi\sigma)$, and/or the further reduction of this potential by the drag force f. This reduction enables particle flow even in the presence of weak noise, where the

occurrence of a Kramers escape of a single particle over the potential barrier would still be an extremely rare event.

At large values of the external force or noise, these peaks are smeared out in Figs. 3.6, 3.13(b) and 3.14(c) with the soliton velocity governed by Eq. (3.9). Together with Eq. (3.34), it reads

$$j_{\mathrm{st}} = \frac{\alpha\mu f}{L(1-\sigma)}. \tag{3.35}$$

The isolines of constant currents in Fig. 3.14(c) follow closely this equation, which in the (f, σ)-plane corresponds to the line set $f/(1-\sigma) = \text{const}$.

3.4 Summary notes

In this chapter, we have considered the crowded BASEP systems with equal number of particles and potential wells, $N = L/\lambda$, and overcrowded BASEP systems with one particle more than the number of potential wells, $N = L/\lambda + 1$. We have shown that the dynamics in such systems is governed by the solitons that manifest themselves as sequences of different particles which propagate even in the limit where the transport of single particles is irrelevant. We have developed the theory to describe generation and propagation of the solitons. We can expect that solitons play an important role in similar setups in colloidal and microfluidic transport, or in biological systems, like transport by kinesin molecular motors [146, 147]. Since a common experimental setup involves systems without inertia, i.e. underdamped dynamics, where polymers and colloids can exhibit a nature of interaction other than hardcore, as well as varying orders of size ranging from nano- to micrometers, it is also intriguing to investigate whether solitons can exist in underdamped dynamics beyond hardcore interaction potentials. It is also of practical interest to determine whether solitons would occur in higher dimensions, such as 2D or 3D. This inquiry is particularly relevant as experimental particles cannot be confined to exact one-dimensional spatial arrangements.

Another interesting question for the model under consideration is whether more than one soliton can occur in the system. In [108] it is shown that the number of solitons is equal to the number of overcrowding. Interestingly, these solitons have an effective repulsive interaction. Here we briefly provide the quantitative explanation of this effect.

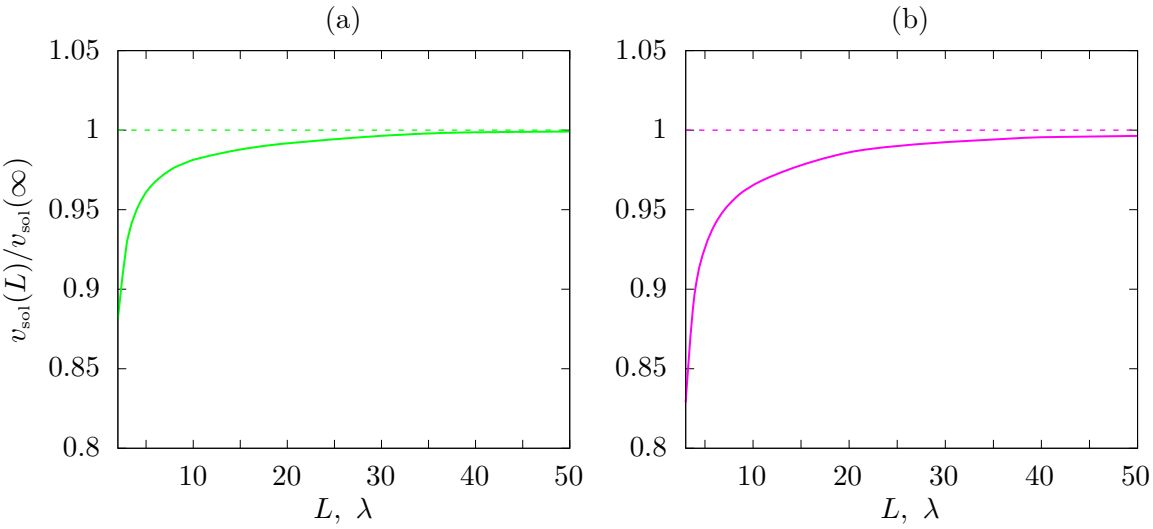

Figure 3.15: Normalized soliton velocity $v_{\rm sol}$ as a function of system length L in the zero-noise limit for the drag force $f\lambda/U_0 = 3.14$ and particle sizes $\sigma = 0.63$ (panel (a), green solid line) and $\sigma = 0.75$ (panel (b), magenta solid line). As a normalization factor, we use soliton velocity in the infinite length limit determined by Eq. (3.33a). In both figures, the soliton velocity in the infinite length is represented as a dashed lined of corresponding color.

3.4.1 Soliton repulsive interaction

As we have mentioned earlier, single particles are never *exactly* in positions of stable equilibrium but only relax toward them at an exponential rate. For a single soliton we have considered the limit where the characteristic relaxation time is much shorter than the time period of the soliton passage of the system. This is the limit of *fast relaxation*. Now we consider the limit of *slow relaxation* where the relaxation time is longer than the time period of the soliton passage, which is the case either for short systems or at big drag force, see the discussion in Sec. 3.3.1.

When the soliton attaches to a particle before it has relaxed to the position of stable equilibrium, its velocity is reduced, as can been seen in Fig. 3.15. The reason for this effect is that each collision with a single particle slows the soliton down, and for the case of slow relaxation, this slowing down starts earlier than in the fast relaxation limit, see Fig. 3.16. We refer to this effect as the *slowing-down mechanism*. While this effect may seem negligible within a single period in Fig. 3.16, it gradually accumulates throughout the propagation process of the soliton, leading to a notable impact on the resulting dynamics.

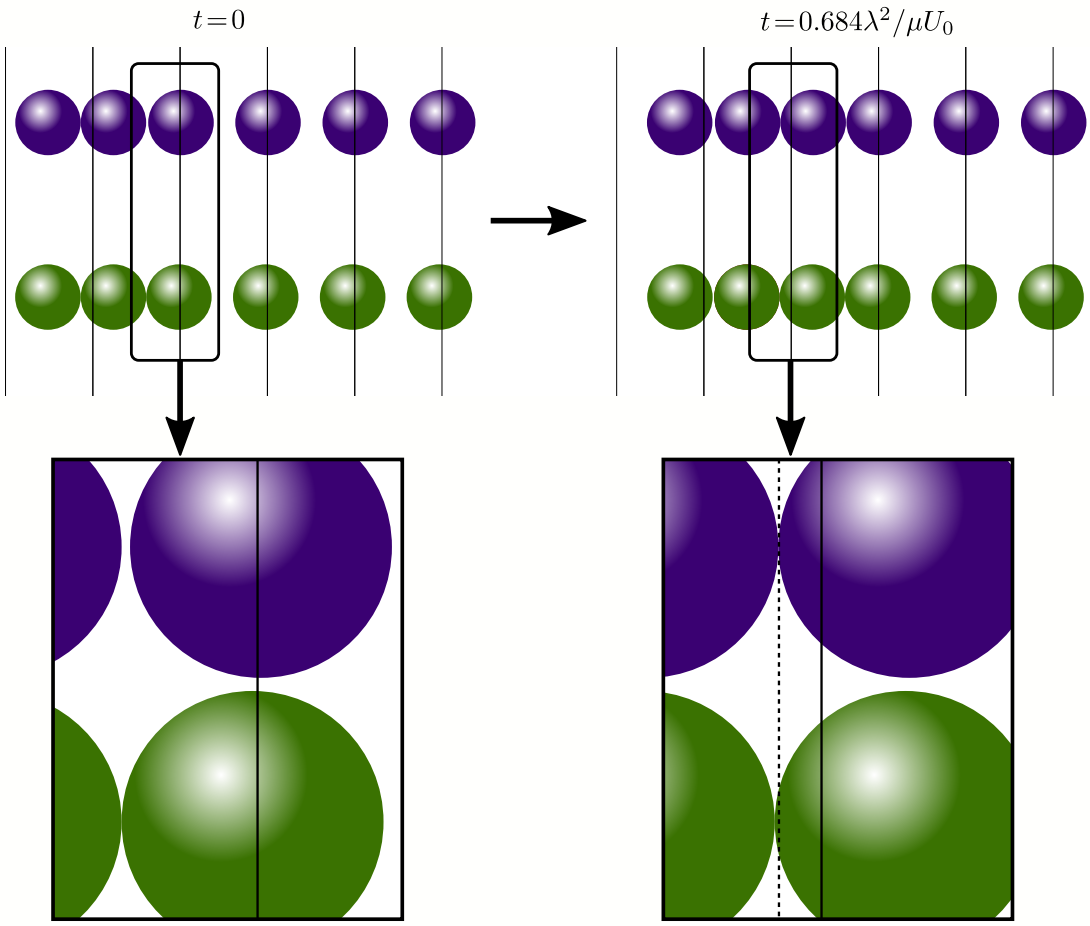

Figure 3.16: An example of soliton propagation in the zero-noise limit for parameters $f\lambda/U_0 = 3.14$ and $\sigma = 0.75$ for $L = 10\lambda$ (green particles, slow relaxation limit) and $L = 50\lambda$ (violet particles, fast relaxation limit). Vertical grid lines correspond to the minima of the tilted potential $U(x) - fx$ and are guides for the eye. In the initial time instant $t = 0$ (left part of the figure), the first two particles have identical positions in both systems. In the system with fast relaxation, particles from third to sixth have already reached their relaxed positions, while in the system with slow relaxation, those particles are still in the process of relaxing. As a result, apart from the first two particles, the green particles are slightly shifted to the left compared to the corresponding relaxed violet particles. This can be observed by comparing the glare on the third particles in the zoomed-in view. Additionally, in the system with slow relaxation, the first two particles have already attached to the third particle, whereas in the system with fast relaxation, the second particle has not yet reached the third particle. At time instant $t = 0.684\lambda^2/\mu U_0$ (right part of the figure), the soliton has passed one wavelength for a system length of $L = 10\lambda$ and is slightly behind the soliton for $L = 50\lambda$. This is particularly noticeable when considering the position of the third particle with respect to the dotted line in the zoomed-in view.

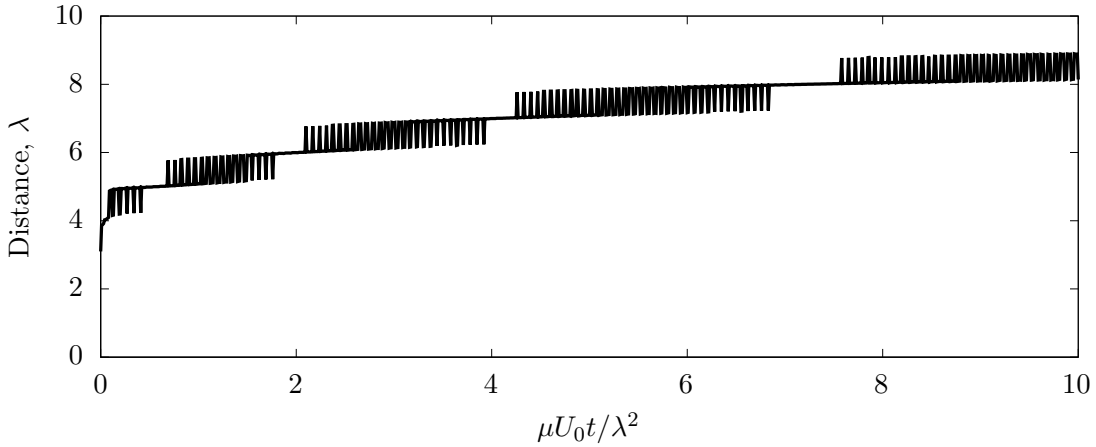

Figure 3.17: Distance between two solitons ($N = L/\lambda + 2$) as a function of time in the zero-noise limit for the system length $L = 20\lambda$ and drag force $f\lambda/U_0 = 3.14$. Initially, the solitons are placed at a close distance, but due to the slowing down mechanism, the second soliton slowly moves away to a distance corresponding to half of the system length. The jump-like changes in the distance between solitons correspond to the detachment of particles, see the discussion in Sec. 3.3.1.

The slowing-down mechanism is also the reason for the repulsive interaction between solitons, since if we put solitons next to each other in the zero-noise limit, the second soliton in the drag force direction would be effectively slowed down by non-relaxed particles from the first soliton, see Fig. 3.17. In the presence of noise, solitons can experience changes in their relative distance due to thermal fluctuations affecting their velocities. However, similar to the zero-noise limit, solitons tend to avoid approaching each other. This behavior also arises from the slowing-down mechanism, which becomes more prominent when solitons are in close proximity. When solitons are near each other, the particles belonging to one soliton do not have sufficient time to relax, thus slowing down the propagation of the subsequent soliton.

In real systems, soliton interactions may also be affected by weak attractive forces, such as the van der Waals interaction. In barrier-free soliton motion, even these small forces may be sufficient to alter the core size of the soliton. Consequently, this may result in adhesion of solitons when they overcome the force of mutual repulsion.

3.4.2 Exchange symmetry effect: application to solitons

The exchange symmetry effect described in Chapter 2 can also justify that solitons occur for $\sigma > 1$. Let us demonstrate this for a system in the zero-noise limit.

We assume that a soliton is present for some drag force f, system length L, particles number $N = L/\lambda + 1$ and particle size $\varsigma < \lambda$. By increasing the particle size by an integer number of wavelengths,

$$\varsigma \to \varsigma + m\lambda, \ m = 1, 2, \ldots, \tag{3.36}$$

we do not change the interaction forces between neighboring particles defined by Eq. (3.18a) due to the λ-periodicity of the external forces. The increase the space between each pair of neighboring particles by $m\lambda$. As a consequence, the system length changes as

$$L \to (L + Nm\lambda) = L(m+1) + m\lambda, \tag{3.37}$$

and for the filling factor $\bar{\rho} = N\lambda/L = 1 + \lambda/L$ the mapping is:

$$\bar{\rho} \to \frac{N\lambda}{L(m+1) + m\lambda} = \frac{\bar{\rho}L}{L(m+1) + m\lambda} = \frac{\bar{\rho}}{m + 1 + (\bar{\rho} - 1)m} = \frac{\bar{\rho}}{1 + m\bar{\rho}}. \tag{3.38}$$

In the mapped system, the soliton velocity is $(m + 1)$ times faster compared to the original system. This relationship arises from the fact that one complete soliton cycle, encompassing the passage of one wavelength in the original system, corresponds to the passage of $(m + 1)$ wavelengths in the mapped system. However, for a single particle to traverse once the entire system, the soliton must propagate through the entire system $(m + 1)$ times. This is due to the fact that a single propagation through the system shifts the particle just by one wavelength, while the distance between neighboring particles is $(m + 1)$ wavelengths. As a result, the mapping of the current in the original system can be described as follows:

$$j_{\mathrm{st}} \to \frac{(m+1)v_{\mathrm{sol}}}{(m+1)(L(m+1) + m\lambda)} = \frac{j_{\mathrm{st}}L}{L(m+1) + m\lambda} = \frac{j_{\mathrm{st}}}{1 + m\bar{\rho}}. \tag{3.39}$$

Equations (3.38) and (3.39) represent the previously introduced relation (2.38a). This commensurability effect plays a vital role in the experimental study of the BASEP, as it offers the opportunity to investigate the dynamics of the same system using different parameter sets, allowing for a comprehensive understanding of its behavior.

3.4.3 Barrier free motion in other periodic potentials

Here we consider a possibility of a barrier-free motion in the zero-noise limit for an arbitrary chosen λ-periodic potential for single particles. The external force $F(x)$ acting on particles is also λ-periodic:

$$F(x) = F(x+\lambda). \tag{3.40}$$

The Fourier series expansion of the periodic force is expressed as

$$F(x) = \sum_{k=-\infty}^{\infty} c_k e^{2\pi i k x/\lambda} = c_0 + 2\mathrm{Re}\left[\sum_{k=1}^{\infty} c_k e^{2\pi i k x/\lambda}\right], \tag{3.41}$$

where the Fourier coefficients c_k are

$$c_k = \frac{1}{\lambda}\int_0^{\lambda} \mathrm{d}x\, F(x)\, e^{-2\pi i k x/\lambda}. \tag{3.42}$$

We note that $c_0 = 0$ as a consequence of the periodicity of both $F(x)$ and its indefinite integral, which represents the external potential. Inserting Eq. (3.41) into Eqs. (3.21b) and (3.15b), we obtain the Fourier series representation of the n-cluster velocity $u_n(x)$:

$$\begin{aligned} u_n(x) &= \mu f + 2\mu\mathrm{Re}\left[\sum_{k=1}^{\infty} c_k e^{2\pi i k x/\lambda} \sum_{j=1}^{n} e^{2\pi i k j \sigma}\right] \\ &= \mu f + 2\mu\mathrm{Re}\left[\sum_{k=1}^{\infty} \frac{1-e^{2\pi i k n\sigma}}{1-e^{2\pi i k\sigma}} c_k e^{2\pi i k x/\lambda}\right]. \end{aligned} \tag{3.43}$$

The periodic term becomes constant when the factor $(1-e^{2\pi i k n\sigma})/(1-e^{2\pi i k\sigma})$ is zero for all k. This can only occur if $n\sigma$ is an integer. For $\sigma < 1$, $u_n(x)$ can thus be constant only for particle sizes σ that are rational numbers:

$$\sigma_{m,n} = \frac{m}{n}, \quad m = 1, \ldots, n-1, \tag{3.44}$$

However, for the factor $(1-e^{2\pi i k n\sigma})/(1-e^{2\pi i k\sigma})$ to be zero, $k\sigma$ must not be an integer, as otherwise $(1-e^{2\pi i k n\sigma})/(1-e^{2\pi i k\sigma}) \to n \neq 0$ according to L'Hospital's rule. This additional requirement of $k\sigma$ not being an integer number cannot be satisfied for all k if $\sigma = \sigma_{m,n}$. This implies that Fourier coefficients c_k must be zero for those k where $k\sigma_{k,n} = km/n$ is an integer. Hence, for $u_n(x)$ to be constant, σ must be one of the rational numbers $\sigma_{m,n}$,

and all Fourier coefficients c_k, for which km/n is an integer number, must be equal to zero.

To determine the appropriate values of k for a given $\sigma_{m,n}$ (where m and n are given), we express m and n in terms of their greatest common divisor $d(m,n)$, such that $m = d(m,n)m'$ and $n = d(m,n)n'$, where m' and n' are mutually prime. In order for km/n to be an integer, k must be a multiple of $n' = n/d(m,n)$. This leads to the requirement that

$$c_k = 0 \text{ for } k = j\frac{n}{d(m,n)}\,, \quad j = 1, 2, \ldots . \tag{3.45}$$

For non-zero drag force $f > 0$, the barrier-free motion is possible even for particle sizes given by irrational σ, as the presence of this force extends the region of barrier-free motion to some neighborhood near particle sizes $\sigma_{m,n}$, see the discussion in Sec. 3.3.1. Since for any finite neighborhood of an irrational number, we can find some rational number that is within this neighborhood, e.g. using the Farey series [148], barrier-free motion is also possible for particle sizes given by irrational σ. Thus, barrier-free motion in the presence of drag force is possible for any periodic potential and particle size.

4 Driven transport of soft Brownian particles

In this chapter, we investigate how the violation of a single-file motion, when particles have a finite probability of penetrating and passing each other thereby changing their order, impacts the collective transport properties. This chapter is mainly based on work [91].

The finite penetration probability can be of different origin. For example, one can consider the motion of interpenetrating macromolecules like polymers in a channel with diameter of about the radius of gyration [149]. It also applies to the motion of colloidal hard-sphere particles in a channel with diameter slightly larger than the particle size [150]. If the penetration depth l_{D} is larger than the difference between channel diameter d and doubled particle size ς,

$$l_{\mathrm{D}} > d - 2\varsigma, \tag{4.1}$$

particles are able to pass each other, see also the illustration in Fig. 4.1.

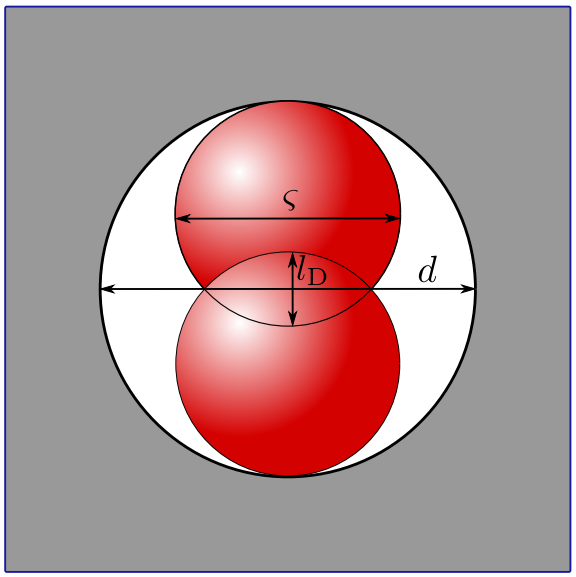

Figure 4.1: The illustration of the prerequisite condition for the penetration depth for particles in a narrow channel to pass each other, corresponding to Eq. (4.1).

To analyze penetration and passing effects, we introduce the concept of the particle *softness*, which would allow us to tune the passing rate. Specifically, the particles interact via the interaction potential

$$V(r) = \frac{V_0}{\varepsilon[1 + \mathrm{erf}(\varsigma/\sqrt{2}\lambda\varepsilon)]} \,\mathrm{erfc}\left(\frac{r-\varsigma}{\sqrt{2}\lambda\varepsilon}\right), \tag{4.2}$$

where r is the distance between center positions of two particles, ς is the (effective) particle size, and $\varepsilon > 0$ is dimensionless softness parameter; erf(.) and erfc(.) are error function and complementary error function, respectively, defined as:

$$\mathrm{erf}(z) = \frac{2}{\sqrt{\pi}} \int_0^z e^{-t^2} \mathrm{d}t, \tag{4.3a}$$

$$\mathrm{erfc}(z) = 1 - \mathrm{erf}(z). \tag{4.3b}$$

Potential set by Eq. 4.2 resembles a smoothened rectangular potential barrier with amplitude V_0/ε. With decreasing ε, this barrier edges become sharper and also steeper, which is illustrated in Fig. 4.2. In the limit $\varepsilon \to 0$, the hard-sphere potential for particles with diameter ς is recovered. Also, unlike other interaction potentials when particle can

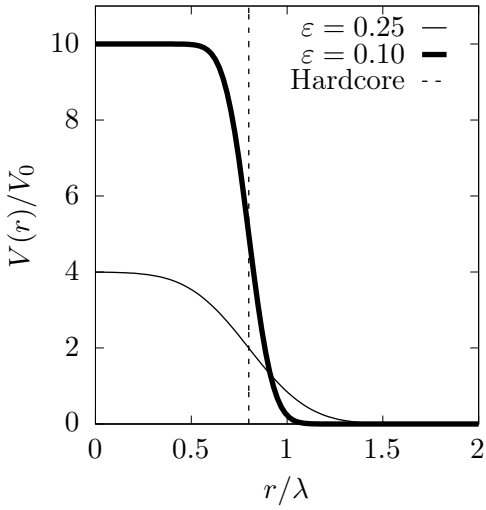

Figure 4.2: Potential of soft interacting particles for $\sigma = 0.8$. The thin solid line corresponds to potential for high passing rate set by softness parameter $\varepsilon = 0.25$, and thick solid line − to low passing rate set by softness parameter $\varepsilon = 0.1$. The dashed line represents the hardcore potential (limit $\varepsilon \to 0$).

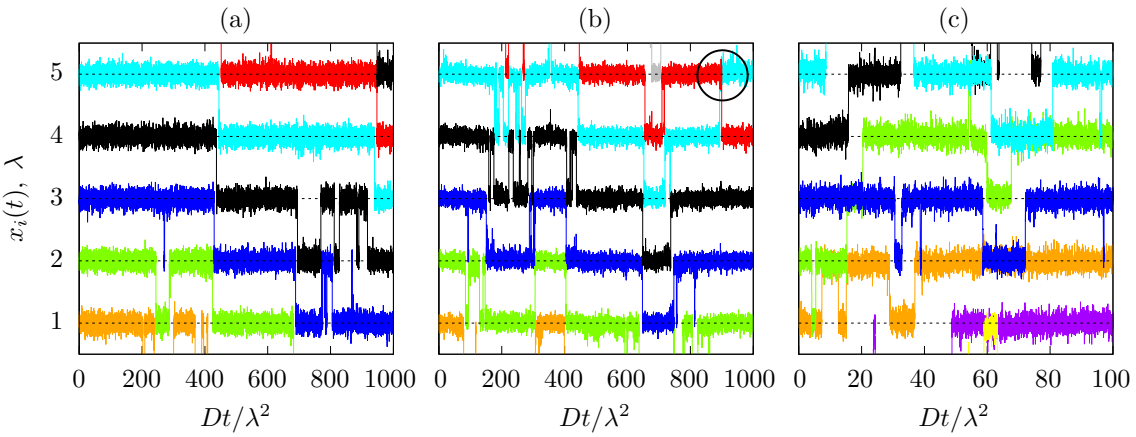

Figure 4.3: Trajectories of the driven Brownian motion for various values of the softness parameter. Panel (a) is for hard particles (BASEP, $\varepsilon \to 0$), (b) is for soft particles with $\varepsilon = 0.1$ (low passing rate), and (c) is for soft particles with $\varepsilon = 0.25$ (high passing rate). The circle in panel (b) marks a crossing of two particles.

penetrate each other, e.g. Lennard-Jones or Coloumb potentials, the suggested potential does not possess a long-range tail, which can play a significant role in collective phenomena. Its presence would have made the comparison with hardcore case less transparent.

Langevin equations describing the driven Brownian motion of particles with interacting potential $V(.)$ are of form

$$\frac{\mathrm{d}x_i}{\mathrm{d}t} = \mu\left(f - U'(x_i) + f_i^{\mathrm{int}}\right) + \sqrt{2D}\,\xi_i(t),\ \ i = 1, \ldots, N, \tag{4.4a}$$

where the total interaction force f_i^{int} acting on particle i can be written explicitly, as the potential $V(x)$ is given by the continuously differentiable function:

$$f_i^{\mathrm{int}} = -\sum_{j \neq i} \frac{\partial V(|x_i - x_j|)}{\partial x_i}. \tag{4.4b}$$

Our main focus in this chapter are fundamental diagrams and their comparison with corresponding results for the case of hard particles. In this chapter, we use the potential amplitude and drag force as in Chapters 2-3, i.e. $U_0/k_{\mathrm{B}}T = 6$, $f\lambda/k_{\mathrm{B}}T = 0.2$, and the amplitude of the interaction potential is $V_0/k_{\mathrm{B}}T = 1$.

4.1 General results

In Figs. 4.3(a)-(c) we show typical particle trajectories for hard particles and soft particles with low and high passing rates, respectively. In all trajectories, we see hopping transitions between neighboring potential wells, since the potential barrier is much larger than the thermal energy. In Fig. 4.3(a), which refers to the BASEP, particles keep their order, while in a slightly softer potential set by $\varepsilon = 0.1$, one crossing between particles can be seen in a probe period of time $1000\lambda^2/D$ in Fig. 4.3(b). For even softer potential given by $\varepsilon = 0.25$, many more crossings between particles and even particle overlaps are observed in a ten times smaller time period $100\lambda^2/D$ in Fig. 4.3(c). These specified features of the trajectories motivate our choice of $\varepsilon = 0.1$ and $\varepsilon = 0.25$ as representative potentials with small and large degrees of softness, respectively.

In Fig. 4.4 we show fundamental diagrams (current-density relations) for these parameters $\varepsilon = 0.1$ and $\varepsilon = 0.25$. The previously used Fig. 2.2 for hard particles, i.e. $\varepsilon \to 0$, is shown here in Fig. 4.4(a) for visual comparison.

4.1.1 Soft particles: low passing rate

As it can be seen from Fig. 4.4(b), the current-density relations for small and intermediate particle sizes are very similar to the BASEP ones in Fig. 4.4(a) if particle size ς is shifted

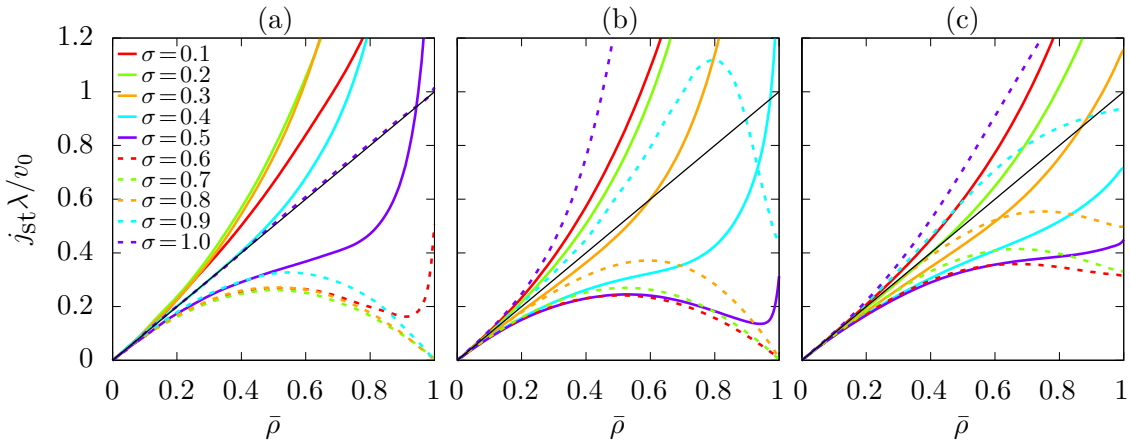

Figure 4.4: Simulated current-density relations for various particle sizes. Panel (a) is for hard particles ($\varepsilon \to 0$) and is identical to Fig. 2.2; panels (b) and (c) are for soft particles with $\varepsilon = 0.1$ and $\varepsilon = 0.25$, respectively. The legend in (a) applies to all panels. The current is normalized to the mean velocity v_0 of a single particle given by Eq. (2.36) and the thin solid line with slope one represents the behavior of independent or point particles in all panels.

by 0.1λ, i.e. lines in Fig. 4.4(b) for $\sigma = 0.1$-0.8 correspond to lines in Fig. 4.4(a) for $\sigma = 0.2$-0.9, respectively. This gives rise to the idea that the currents of soft particles can be described by that of hard particles with an effective particle size. This idea is developed and elaborated in Sec. 4.2.

4.1.2 Soft particles: high passing rate

The current-density relations in case of high passing rate in Fig. 4.4(c) still resemble features analogous to those in Fig. 4.4(a) and (b), but the sensitivity to particle size is much weaker, since the higher passing probability leads to reduction of both barrier enhancement and blocking effect. As a result, the particle current does not have large deviations from the current of independent particles. In particular, parabolic ASEP-like curves do not appear at large particle sizes due to weakening of the blocking effect. The curve shapes themselves for large particle sizes, shown as dashed lines in Fig. 4.4(c), are unique and have no counterparts in Fig. 4.4(a) and (b).

4.2 Theoretical approaches

4.2.1 AZMIF

The AZMIF described in Sec. 2.3 for hard particles can be also implemented in the case of soft ones. Equation (2.40b) remains unchanged for the soft particles; however, a non-trivial point in this case is the derivation of equilibrium density profile, since the exact density functional for soft particles is unknown in this case. Here we calculate it in the grand canonical ensemble by applying the density functional theory [110], see also the corresponding discussion for hard particles in Sec. 2.2.1. Following this theory, we minimize the corresponding functional of the density profile:

$$\Omega[\varrho] = F_{\mathrm{id}}[\varrho] + F_{\mathrm{exc}}[\varrho] + \int \mathrm{d}x \varrho(x)[U(x) - \mu_{\mathrm{ch}}], \tag{4.5}$$

where $F_{\mathrm{id}}[\varrho] = k_{\mathrm{B}}T \int \mathrm{d}x \varrho(x)[\ln[\Lambda\varrho(x)] - 1]$ and $F_{\mathrm{exc}}[\varrho]$ are the ideal and excess part of the free energy functional, Λ is the de Broglie wavelength, and μ_{ch} is the chemical potential. The minimization condition (2.16) for $\Omega[\varrho]$ to be minimal at the equilibrium density yields the equation

$$\varrho_{\mathrm{eq}}(x) = \frac{e^{\beta\mu_{\mathrm{ch}}}}{\Lambda} \exp\left[-\beta U(x) + c^{(1)}(x; [\varrho_{\mathrm{eq}}])\right] \tag{4.6}$$

for calculating $\varrho_{\mathrm{eq}}(x)$. Here

$$-k_{\mathrm{B}}Tc^{(1)}(x;[\varrho_{\mathrm{eq}}]) = \frac{\delta F_{\mathrm{exc}}[\varrho]}{\delta\varrho(x)}\Big|_{\varrho=\varrho_{\mathrm{eq}}} \tag{4.7}$$

is the potential of the mean interaction force in equilibrium. It can be calculated from the direct correlation function $c^{(2)}(r;[\varrho])$, which is given by the second functional derivative of $F_{\mathrm{exc}}[\varrho]$:

$$-k_{\mathrm{B}}Tc^{(2)}(|x-x'|;[\varrho_{\mathrm{eq}}]) = \frac{\delta^2 F_{\mathrm{exc}}[\varrho]}{\delta\varrho(x)\delta\varrho(x')}. \tag{4.8}$$

By Taylor expansion of $F_{\mathrm{exc}}[\varrho]$ around $\bar{\varrho}$ up to first order, we obtain the approximation:

$$c^{(1)}(x;[\varrho]) = \int \mathrm{d}x' c^{(2)}(|x-x'|;\bar{\varrho})\,(\varrho(x)-\bar{\varrho})\,. \tag{4.9}$$

The direct correlation function $c^{(2)}(r;[\varrho])$ is related to the pair correlation function $g(r) = 1 + h(r)$ in the homogeneous system ($U_0 = 0$) with density $\bar{\varrho}$ via the Ornstein-Zernike relation:

$$h(|x|) = c^{(2)}(|x|;\bar{\varrho}) + \bar{\varrho}\int \mathrm{d}x' c^{(2)}(|x-x'|;\bar{\varrho})h(|x'|). \tag{4.10}$$

For determining $c^{(2)}(|x-x'|;\bar{\varrho})$ and thus $c^{(1)}(x;[\varrho])$ from Eq. (4.9), a further equation between $c^{(2)}(r,\bar{\varrho})$ and $g(r)$ is needed. As we deal with short-range interactions, we use the approximate Percus-Yevick closure relation there [151],

$$c^{(2)}(r,\bar{\varrho}) = g(r)\left[1-\exp\left(\frac{V(r)}{k_{\mathrm{B}}T}\right)\right]. \tag{4.11}$$

Using Eqs. (4.6)-(4.11), we can determine $\varrho_{\mathrm{eq}}(x)$ numerically for a given σ and $\bar{\varrho}$. To this end, we first solve Eqs. (4.10) and (4.11) for $c^{(2)}(r,\bar{\varrho})$. Equation (4.9) then gives $c^{(1)}(x;[\varrho])$ for any profile $\varrho(x)$. The equilibrium profile must satisfy Eq. (4.6). By inserting $c^{(1)}(x;[\varrho])$ into Eq. (4.6), we thus can calculate $\varrho_{\mathrm{eq}}(x)$ by iterative procedure. Specifically, we fix the value of σ and determine $\rho_{\mathrm{eq}}(x) = \lambda\varrho_{\mathrm{eq}}(x)$ in a series of calculations for increasing values of $0 < \bar{\rho}_1 < \bar{\rho}_2 < \ldots < \bar{\rho}_n$, where $\bar{\rho} = \bar{\varrho}\lambda$. As starting profile for determining the profile for $\bar{\rho}_{n+1}$, we used the profile already calculated for $\bar{\rho}_n$. For the smallest $\bar{\rho}_1$, the equilibrium density for independent particles given by Boltzmann distribution is used as the starting profile.

Figure 4.5 shows various representative density profiles for the equilibrium state and nonequilibrium steady state. As for the equilibrium profiles, we determined the profiles both from the procedure described above and from Brownian dynamics simulations. For

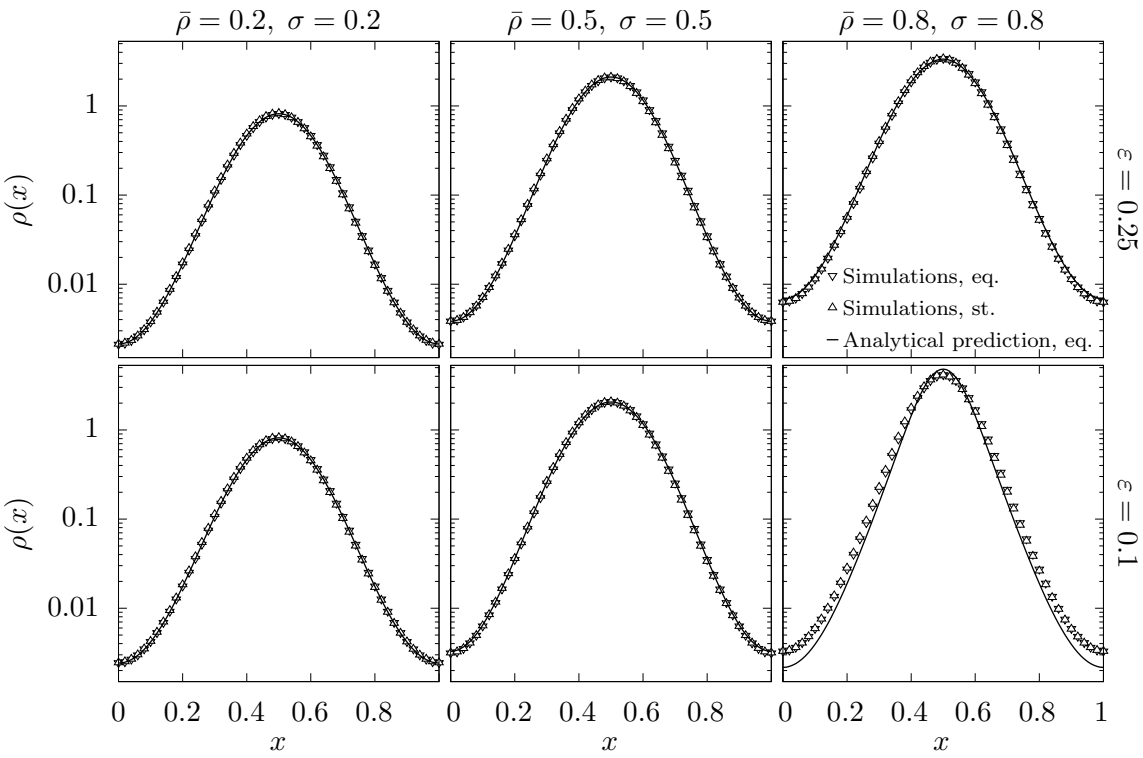

Figure 4.5: Comparison of density profiles: equilibrium profiles obtained from Brownian dynamics simulations (down-pointing triangles) and from numerical calculations using Eqs. (4.6)-(4.11) (solid lines), and nonequilibrium steady state profiles for $f = 0.2\lambda/k_{\mathrm{B}}T$ obtained from Brownian dynamics simulations (up-pointing triangles). Densities are plotted on a logarithmic scale to be sensitive to relative deviations. Noticeable deviations can be seen only between simulated and calculated equilibrium profiles for large $\bar{\rho}$ and low passing rate, and deviations between equilibrium and nonequlibrium simulated profiles are negligible.

the case of high passing rate $\varepsilon = 0.25$, we always find excellent agreement. In the case of low passing rate $\varepsilon = 0.1$, the agreement is still good for small and intermediate densities, but becomes less satisfying at higher density. This can be seen from the rightmost graph in the lower row of the figure. The main cause of the deviation is explained by the fact that the Percus-Yevick closure relation (4.11) is no longer a good approximation. Since it is beyond the scope of the present thesis to address this issue, we provide possible ways to improve this procedure in the Summary notes.

The nonequilibrium steady state profiles are almost indistinguishable from the equilibrium ones for the weak drag force $f = 0.2\lambda/k_{\mathrm{B}}T$. This suggests that, similarly to the

case of hard particles, the AZMIF provides a good description of the transport behavior as long as the mean interaction force $\overline{f^{\mathrm{int}}}$ is negligible.

4.2.2 Effective size method

The main idea of the effective size method is to use the BASEP as a reference model, so that the current of soft particles is set by the BASEP with the same particle density and effective particle size σ'. The idea itself is not novel and is most frequently mentioned in the context of the method proposed by Weeks, Chandler, and Anderson [152]. However, the new approach for determining the effective particle size, which we propose in this chapter, is significantly different from the previously proposed ones. Its essence is that we match equilibrium profiles for soft and hard particles as closely as possible.

To find the best match, we substitute the equilibrium profile $\varrho_{\mathrm{eq}}(x)$ of soft particles into the exact functional of the density profile for hard rods,

$$\Omega_{\mathrm{HC}}(\sigma_{\mathrm{HC}},\bar{\rho}) = \int_0^\lambda \mathrm{d}x\varrho(x)\left(U(x)-\mu_{\mathrm{ch}}-k_{\mathrm{B}}T\left[1-\ln\left(\frac{\varrho(x)}{1-\eta(x,\sigma_{\mathrm{HC}})}\right)\right]\right) \tag{4.12}$$

and vary the effective size σ_{HC} until the measure $\delta\Omega_{\mathrm{HC}}(\sigma_{\mathrm{HC}},[\varrho_{\mathrm{eq}}])/\delta\varrho_{\mathrm{eq}}$ has the smallest deviation from zero within $0\leq x\leq\lambda$ at $\sigma_{\mathrm{HC}}=\sigma'$. This procedure reads as follows:

$$\sigma'(\bar{\rho},\sigma) = \underset{\sigma_{\mathrm{HC}}}{\mathrm{argmin}}\left\{\sup_{0\leq x\leq\lambda}\left|\frac{\delta\Omega_{\mathrm{HC}}(\sigma_{\mathrm{HC}};[\varrho_{\mathrm{eq}}])}{\delta\varrho_{\mathrm{eq}}(x)}\right|\right\}, \tag{4.13}$$

and the current is determined by the relation

$$j_{\mathrm{st}}(\bar{\rho},\sigma) = j_{\mathrm{st}}^{\mathrm{BASEP}}(\bar{\rho},\sigma'), \tag{4.14}$$

with $j_{\mathrm{st}}^{\mathrm{BASEP}}$ the stationary current for the BASEP.

4.3 Application of theoretical approaches

Let us now compare the introduced theoretical approaches for cases of both low and high passing rates with corresponding simulation results.

4.3.1 Low passing rate

In Fig. 4.6(a), we present fundamental diagrams, obtained by Brownian dynamics simulations (symbols), in comparison with those obtained by AZMIF (thin dashed lines) and effective size method (thick dashed lines) for the low passing rate $\varepsilon = 0.1$. It can be noted at once that the newly introduced effective size method provides good description for all particles sizes, while the application of AZMIF shows pronounced deviations at $\sigma = 0.5$ similarly as in the BASEP, see the discussion in Sec. 2.3. In addition to more accurate description, the effective particle size σ' plotted in Fig. 4.6(b) also provides a clear explanation for various physical effects observed in current-density curves.

For $\sigma \lesssim 0.8$, as one could expect from the discussion in Sec. 4.1.1, the effective particle size is about 0.1 wavelength larger than the real size of a soft particle. Interestingly, the dependence of $\sigma'(\sigma, \bar{\rho})$ on $\bar{\rho}$ is weak, except for $\bar{\rho} = 1$ at large σ. Due to the fact that $\bar{\rho}$ takes on discrete values, the significant change of σ' in the inset of Fig. 4.6(b) appears as a step from $\bar{\rho} = 0.99$ to 1. This change indicates the special behavior of the BASEP at $\bar{\rho} = 1$ for large particle sizes $0.6 \lesssim \sigma \lesssim 1$. In this case of special behavior, transport dynamics

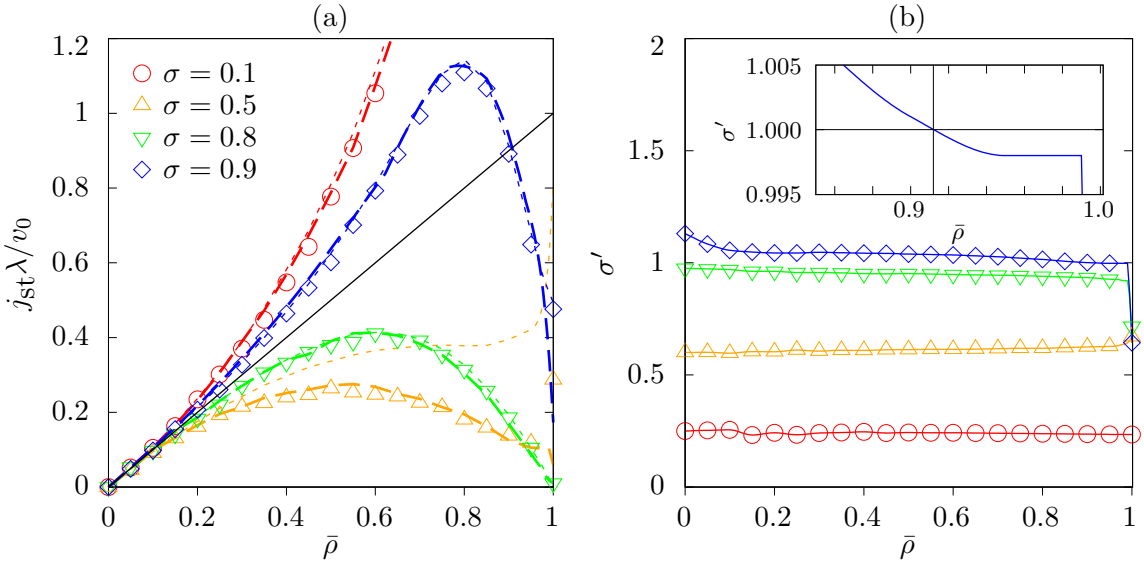

Figure 4.6: (a) Comparison of current-density relations given by the AZMIF (thin dashed lines) and the effective size method (thick dashed line) with the simulated data (symbols) for low passing rate ($\varepsilon = 0.1$) and 4 representative particle sizes. The solid line with slope one indicates the behavior for independent or point particles. (b) Effective particle sizes σ' calculated from Eq. (4.13) for the data shown in (a) [same symbols and line colors, see legend in part (a)]. The inset shows a zoom-in of the curve for $\sigma = 0.9$ and $\bar{\rho}$ close to one.

is governed by the thermally activated Brownian solitons that do not have analogues in non-crowded systems.

Effective size method also allows to explain the behavior of current-density curve at $\sigma = 0.9$ in Fig. 4.4(b), that does not have analogues in the BASEP for any particle size, see Fig. 4.4(a). In the inset of Fig. 4.6(b), the effective size decreases from $\sigma' > 1$ to $\sigma' < 1$, with $\sigma' = 1$ at $\bar{\rho}_\times \approx 0.91$. To understand why this transition causes a dramatic current change, we turn to Eq. (2.38a). From this relation, we can see that for $\sigma' > 1$, which corresponds in Fig. 4.6(a) to $\bar{\rho} < \bar{\rho}_\times$, the system is equivalent to one with particles size $(\sigma' - 1)$, where the barrier reduction effect prevails. For $\sigma' < 1$ corresponding to $\bar{\rho} > \bar{\rho}_\times$ in Fig. 4.6(a), the blocking effect is dominant. All of the above mentioned effects occur in the corresponding current-density curve, and the soft particle current at $\bar{\rho} = 1$ does not approach zero on the contrary to BASEP, since the blocking effect is weaker in the case of soft particles. This feature is observed in the effective size method via significant change of σ' at $\bar{\rho} = 1$, but in general, due to above mentioned specific behavior of the current in the BASEP, effective size method is beyond its applicability at $\bar{\rho} = 1$ for large σ'.

4.3.2 High passing rate

One could assume that the effective size method should not describe well the case where the probability of particles overtaking each other is significant, that can be observed in the representative example in Fig. 4.3(c)). Indeed, in such case the physical interpretation of effective size becomes ambiguous and may not provide meaningful insights into the system behavior. However, as we can see from Fig. 4.7(a), the effective size method is still able to predict many features of current-density curve behavior. In fact, at $\sigma = 0.1$ and $\sigma = 0.9$ the method gives a correct description for $\bar{\rho} \lesssim 0.7$, at $\sigma = 0.5$ for $\bar{\rho} \lesssim 0.5$, and the case $\sigma = 0.8$ is described exactly at any $\bar{\rho}$ except for the special case of $\bar{\rho} = 1$. At the same time, the AZMIF yields discrepancies for $\bar{\rho} \gtrsim 0.7$ at all considered particle sizes σ.

More detailed analysis of particle trajectories in equilibrium in Fig. 4.8, however, shows that the current-density curves do not in any way contradict the stated assumption that the effective size method should exhibit worse results at high passing rates. Indeed, particle overlappings, marked by rounded rectangles, occur much more frequent for $\sigma = 0.5$ where the effective size method fails, than for $\sigma = 0.8$ where the effective size method has en excellent agreement, in spite of fact that the total overlapping time is longer in the latter case.

This seemingly paradoxical situation has a fairly simple explanation. For large $\sigma = 0.8$ or $\sigma = 0.9$, the probability of a potential well to be occupied by two particles becomes

significant only at high densities $\bar{\rho}$, therefore the passing rate is relatively low, and the agreement between the currents predicted by the effective size method with the simulated ones is thereby sufficiently good. On the contrary, for $\sigma = 0.5$ the probability of a potential well to be doubly occupied is high, which subsequently leads to the high passing rate. The blocking effect for the effective particle size σ' given in Fig. 4.7(b) is thus overestimated compared to the system of soft particles, thereby predicting lower currents than those from simulations. Finally, for $\sigma = 0.1$, σ' is small as well, see Fig. 4.7(b), so the barrier reduction effect dominates the current behavior in the corresponding BASEP. Thus, the high passing rate of soft particles for $\sigma = 0.1$ is irrelevant and the effective size method provides a good description of the current-density relation.

4.4 Summary notes

The goal of this chapter was to investigate how the softness of particle interactions affects collective transport properties. To facilitate a systematic comparison with hardcore inter-

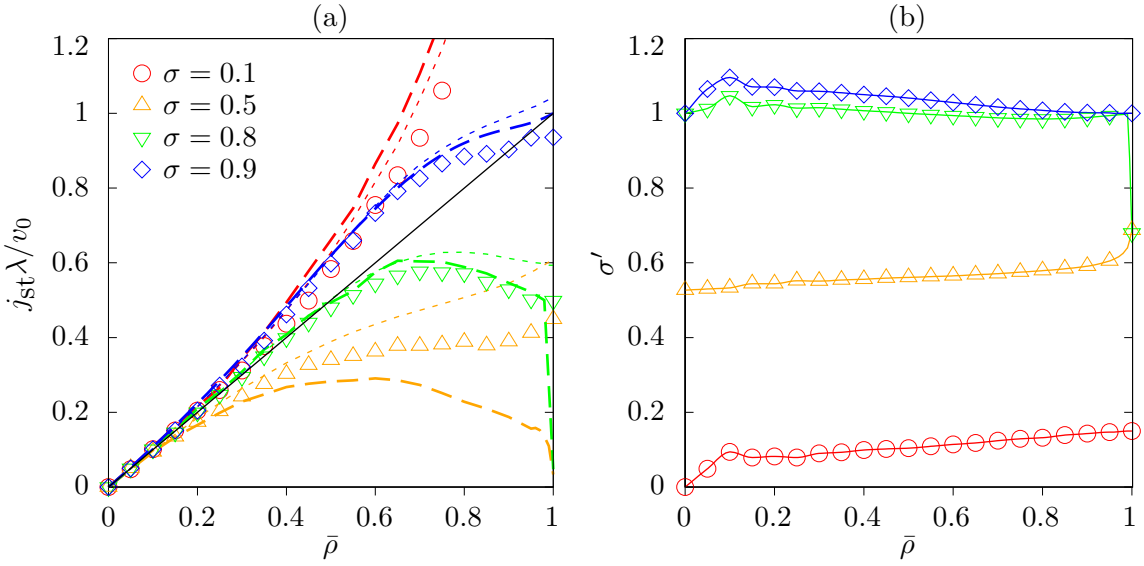

Figure 4.7: (a) Comparison of current-density relations given by the AZMIF (thin dashed lines) and the effective size method (thick dashed line) with the simulated data (symbols) for high passing rate ($\varepsilon = 0.25$) and 4 representative particle sizes. The solid line with slope one indicates the behavior for independent or point particles. (b) Effective particle sizes σ' calculated from Eq. (4.13) for the data shown in (a) [same symbols and line colors, see legend in part (a)].

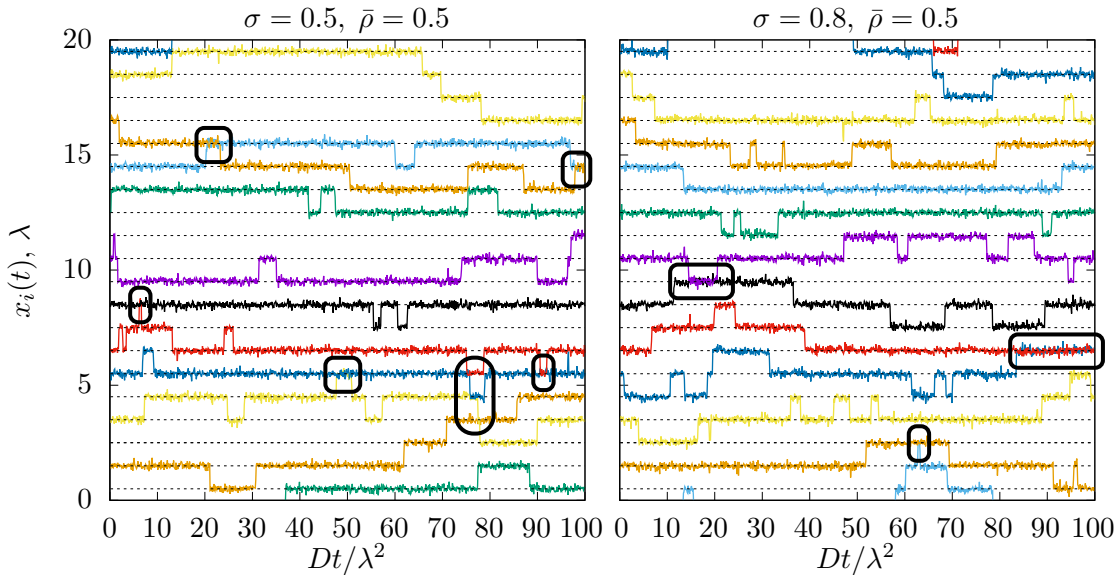

Figure 4.8: A representative example of trajectories for $\bar{\rho} = 0.5$ and two different particle sizes $\sigma = 0.5$ and $\sigma = 0.8$ in equilibrium, $f = 0$. Black rounded rectangles mark particle overlappings, and dashed lines denote potential minima.

acting particles, we considered a smoothed rectangular barrier potential as the interaction potential, which can be tuned by a single parameter to control its softness.

The softness of this potential introduces two key features: a smoothed barrier step and a finite height of the barrier. The smoothed step allows particles to partially penetrate each other, resulting in a penetration effect, while the finite barrier height allows particles to pass each other, leading to a passing effect. We focused our analysis on two cases with low and high passing rates, respectively. In the case of a low passing rate, only the penetration effect is significantly present.

Interestingly, even when the passing rate is negligible, we observed peculiar current-density relations that do not have counterparts in a hardcore interacting system. To explain this phenomenon, we introduced the effective particle size method. This method maps a system of soft particles with a system of hard particles at the same density, using an effective particle size that is determined based on the equilibrium density functional of hard spheres. The effective particle size depends on both the size and density of soft particles, and this dependence allows for a successful description of the peculiar current-density relations. Therefore, we concluded that the effective size method accurately accounts for the impact of the penetration effect on transport behavior, and also provides a way

to interpret the dynamics based on the knowledge of the hardcore interacting reference system.

When the potential barrier is low, the passing rate of particles can become significant. In such cases, there are two distinct regimes: one at low density where the penetration effect dominates, and another at high density where the passing effect is more prominent. In the low-density regime, our effective size method is able to accurately describe the current-density relation. However, in the high-density regime, the effective size method no longer provides a satisfactory quantitative description. Thus, a different or modified theoretical approach is required to effectively capture the collective dynamics in this regime.

We have also elaborated the analytical procedure of calculating the equilibrium density profile for the case of soft particles where the exact functional of the density profile is unknown. The suggested approach has a good agreement with the simulation results except for the case of high system coverage, where the implemented Percus-Yevick closure relation is no longer a valid approximation. A possible way to improve this treatment is implementing the weighted density functionals, see e.g. [153–155].

The effective size method has been employed here to describe current-density relations. However, we anticipate that this method could also be applied to other nonequilibrium properties, and may be particularly valuable in studying soft particles with long-range attractive interactions [156]. Determining the effective size in such cases could benefit from advancements in equilibrium density functional theory for corresponding hardcore interacting systems [157, 158]. Additionally, mixtures of soft particles could be treated using density functionals for hard sphere mixtures [159, 160]. It is important to conduct experimental verification of the findings presented here, as the notable impacts observed in collective transport can be detected not only in currents but also in the local kinetics of tagged particles [161, 162].

5 Computational methods

5.1 Introduction

Since the early stages of computational physics, simulating hard spheres has been a problem that has garnered attention [163, 164]. The main advantage of applying hardcore interactions is the ability to perform analytical calculations. For instance, in the one-dimensional model of hard rods, Percus obtained analytical results that proved pivotal in the field of equilibrium statistical physics [115, 165]. In the present thesis, we have utilized these results in Chapters 2-3.

Algorithm development took a major step forward with the introduction of dynamic simulations, which allowed for the study of nonequilibrium properties in addition to equilibrium. The first dynamic algorithm was still similar to standard Monte Carlo simulations and was based on rejecting movements violating the hardcore condition [166]. A modification to this approach was made by placing collided particles in contact instead of rejecting these movements [167]. Nevertheless, these methods exhibit poor performance at high system coverage. An alternative procedure based on the decomposition of particle motion into a part in agreement with the hardcore condition and a part violating it yields good results also for non-zero external potentials, however, the computation time grows exponentially with the collision frequency/system coverage [168].

In the present thesis, we implement the *event-driven dynamics* as a solution, which completely avoids overlapping particles and is consistent with Brownian dynamics governed by the system of Langevin equations. The concept of this approach is based on the idea of running pure Newtonian simulations within one time step. When during a time step two particles collide, their collision may have some degree of elasticity. The results for single collisions are exact, see e.g. [169], and the overall precision depends on the fineness of time step interval. In one-dimensional system the choice of elasticity is optional because collisions conserve the local momentum regardless of the degree of elasticity [144], and the hardcore constraint set by expression (2.3) is automatically applied for event-driven collisions. Here, the hardcore constraint has an important role because it implicitly sets

the evolution equation for the local density (2.9a), (2.9a) through the imposed boundary conditions on the current [123]:

$$[j_i(x_1,\ldots,x_n,t) - j_{i+1}(x_1,\ldots,x_n,t)]_{x_{i+1}=x_i+\varsigma} = 0,\ i = 1,\ldots,N-1. \tag{5.1}$$

Here j_i are currents of the Smoluchowski equation for joint probability density $\varrho^{(N)}(x_1,\ldots,x_N,t)$ of finding N particles at positions $x_1,\ldots,x_N$ at time t:

$$\frac{\partial \varrho^{(N)}(x_1,\ldots,x_N,t)}{\partial t} = \sum_{i=1}^{N} \frac{\partial j_i}{\partial x_i}, \tag{5.2a}$$

$$j_i = j_i(x_1,\ldots,x_N) = \mu\left[f - U'(x_i) + f_i^{\mathrm{int}}(x_1,\ldots,x_N)\right]\varrho^{(N)} - D\frac{\partial \varrho^{(N)}}{\partial x_i}. \tag{5.2b}$$

The numbering of particles follows the same order as for clusters, ascending in the bias direction, with the N^{th} particle also considered as the 0^{th} (and vice versa) due to periodic boundary conditions.

Equations (5.1), (5.2a) and (5.2b) were given earlier for dynamics of two particles in Sec. 2.4, see Eqs. (2.55), (2.56b) and comments to them. Integrating Eq. (5.2a) over $x_2,\ldots,x_N$ with respect to the hardcore constraint (2.3), boundary conditions (5.1), and periodic boundary conditions yields the Fokker-Plank equation (2.9a) corresponding to the described Langevin dynamics. The details of the Fokker-Planck equation derivation were thoroughly described in [85] in Supplemental Material.

For a small enough time step, the simulation results will be identical regardless of elasticity, but the choice of such a step is not optimal in terms of computational time. Thus, the choice of elasticity for a finite time step is due to its characteristic features. For example, in systems with zero or low thermal noise, clusters of particles in contact with each other play an important role, making an algorithm with inelastic collisions preferable. In systems with strong thermal noise, particles are unlikely to be in direct contact, so an algorithm with elastic collisions is more suitable.

In system with more than one dimension, multiparticle collisions are allowed, which are difficult to implement in Brownian dynamics simulations. This problem can be resolved by considering elastic collisions, where the multiparticle collision is nothing else but a sequence of binary collisions separated by small time intervals [170, 171]. For inelastic particles, most of approaches to deal with multiparticle collisions also imply that such collision can be replaced by the sequence of binary collisions [172–174]. However, in many cases multicontact should be allowed, because it is often found in real systems [175–177]. In such systems, particles can also be grouped into clusters similar to those reported in

Chapter 3. The presence of these clusters can be justified by kinetic theory, thereby establishing the limits of applicability of the binary collision approach (inelastic or elastic) [178]. Aggregation of such clusters in Brownian dynamics simulation, analogous to the attachment-detachment mechanism introduced in Sec. 3.3.1, was described in [179].

In this final chapter, we first introduce the general mechanism of Langevin dynamics simulation that is relevant for both soft and hard particle dynamics. After that, we describe in detail the algorithm for hard particles with totally elastic collisions implemented in Chapter 2 and Sec. 3.2, and the algorithm for hard particles with totally inelastic collisions implemented in Sec. 3.3. Additionally, we also provide a detailed description of the procedures, which we implemented in order to measure certain quantities in the performed simulation.

5.2 Langevin dynamics simulation

We start with Langevin equations for independent particles:

$$\frac{\mathrm{d}x_i}{\mathrm{d}t} = \mu\left(f - U'(x_i)\right) + \sqrt{2D}\,\xi_i(t), \quad i = 1, \ldots, N. \tag{5.3}$$

Integrating it from t to $t + \Delta t$ yields

$$x_i(t + \Delta t) - x_i(t) = \int_t^{t+\Delta t} \left[\mu\left(f - U'(x_i)\right) + \xi_i(\tau)\right] \mathrm{d}\tau. \tag{5.4}$$

For a small time step Δt we can set $x_i = x_i(t)$ and $\xi_i = \xi_i(t)$ within the time interval $[t, t + \Delta t[$. In order to do this for the stochastic term ξ_i, we also need to perform the time discretization of the Gaussian white noise correlations,

$$\xi_i(t) \propto \mathcal{N}_i, \tag{5.5}$$

where $\mathcal{N}_i$ are Gauss distributed numbers with normal standard distribution (zero mean, unit variance). By turning Dirac delta into Kronecker delta,

$$\langle \xi_i(t)\xi_j(t')\rangle = \delta_{ij}\delta(t - t') \quad \rightarrow \quad \frac{\delta_{tt'}\delta_{ij}}{\Delta t} \tag{5.6}$$

and given that if the variance is scaled by a constant, the values are scaled by the square root of that constant, we obtain the proportionality factor in (5.5) as $\Delta t^{-1/2}$. Thus, after the integration we obtain [114]:

$$x_i(t+\Delta t) = x_i(t) + \mu\left(f - U'(x_i)\right)\Delta t + \sqrt{2D\Delta t}\,\mathcal{N}_i, \quad i = 1, \ldots, N, \tag{5.7}$$

where the particle (pseudo)velocity $u_i = u_i(x_i(t))$ is fixed within the time interval $[t, t+\Delta t[$:

$$u_i = \mu\left(f - U'(x_i)\right) + \sqrt{\frac{2D}{\Delta t}}\,\mathcal{N}_i, \quad i = 1, \ldots, N. \tag{5.8}$$

Equation (5.7) is nothing else but the evolution equation based on the standard Euler method expanded with a stochastic term. For an explicitly defined interaction force, such as for the case of soft particles, this evolution equation is analogous to Eq. (5.7):

$$x_i(t+\Delta t) = x_i(t) + \mu\left(f - U'(x_i) + f_i^{\text{int}}\right)\Delta t + \sqrt{2D\Delta t}\,\mathcal{N}_i, \quad i = 1, \ldots, N \tag{5.9}$$

The dynamics simulation in the case of explicitly defined interaction force is straightforward: we evolve the system state with a time step Δt, updating positions of particles for the subsequent step according to Eq. (5.7) for independent particles and to Eq. (5.9) for soft particles.

5.3 Totally elastic collisions

Since the explicit analytical calculation of the interaction force is impossible for hard particles due to δ-singularity at the contact point between interacting particles, we need to take interaction forces into account via event-driven dynamics from a collision at time t_{coll} to a next collision at time t'_{coll}. For the simulation within time interval $[t, t+\Delta t[$ we first set $t_{\text{coll}} = t$ and calculate particle velocities as for independent particles via Eq. (5.8). Knowing these velocities, we can determine whether a collision occurs within the time interval $[t_{\text{coll}}, t+\Delta t[$. A collision can be possible if velocities of neighboring particles satisfy

$$u_i(t_{\text{coll}}) > u_{i+1}(t_{\text{coll}}), \tag{5.10}$$

with time point of the possible collision between i-th and $(i+1)$-th particles:

$$t_{i,i+1} = t_{\text{coll}} + \frac{x_{i+1}(t_{\text{coll}}) - x_i(t_{\text{coll}}) - \varsigma}{u_i(t_{\text{coll}}) - u_{i+1}(t_{\text{coll}})} \tag{5.11}$$

The next collision that occurs at time t'_{coll} is the one with the smallest time in the set $\{t_{i,i+1}\}$,

$$t'_{\text{coll}} = \min_i \{t_{i,i+1}\} \tag{5.12}$$

In case $t'_{\text{coll}} \geq t + \Delta t$, particles can be considered as independent within the time interval $[t_{\text{coll}}, t + \Delta t[$, so that their velocities calculated at time t_{coll} remain unchanged. Otherwise, we determine the left particle i_{coll} participating in this collision:

$$i_{\text{coll}} = \operatorname{argmin}_i \{t_{i,i+1}\} \tag{5.13}$$

In case of totally elastic collisions in one dimensional space, collided particles exchange their velocities [180]:

$$\begin{aligned} u_i(t'_{\text{coll}}) &= u_{i+1}(t_{\text{coll}}), \\ u_{i+1}(t'_{\text{coll}}) &= u_i(t_{\text{coll}}). \end{aligned} \tag{5.14}$$

Correspondingly, positions of all particles are updated at time t'_{coll},

$$x_i(t'_{\text{coll}}) = x_i(t_{\text{coll}}) + u_i(t_{\text{coll}})(t'_{\text{coll}} - t_{\text{coll}}). \tag{5.15}$$

The event-driven procedure given by Eqs. (5.10)-(5.15) is repeated until $t'_{\text{coll}} \geq t + \Delta t$. After that, positions of all particles at time $t + \Delta t$ are calculated using the expression

$$x_i(t + \Delta t) = x_i(t_{\text{coll}}) + u_i(t_{\text{coll}})(t + \Delta t - t_{\text{coll}}). \tag{5.16}$$

Afterward, updated velocities $u_i(t + \Delta t)$ at time $t + \Delta t$ are calculated, and the event-driven procedure is carried out for the next time step. A flow diagram that illustrates the algorithm is provided in Fig. 5.1.

This algorithm is in fact identical to the approximate Green's function dynamics introduced in [171, 181].

5.4 Totally inelastic collisions

This section is partially based on [89].

After the totally inelastic collision of two particles takes place, the corresponding velocities change has the form [180]:

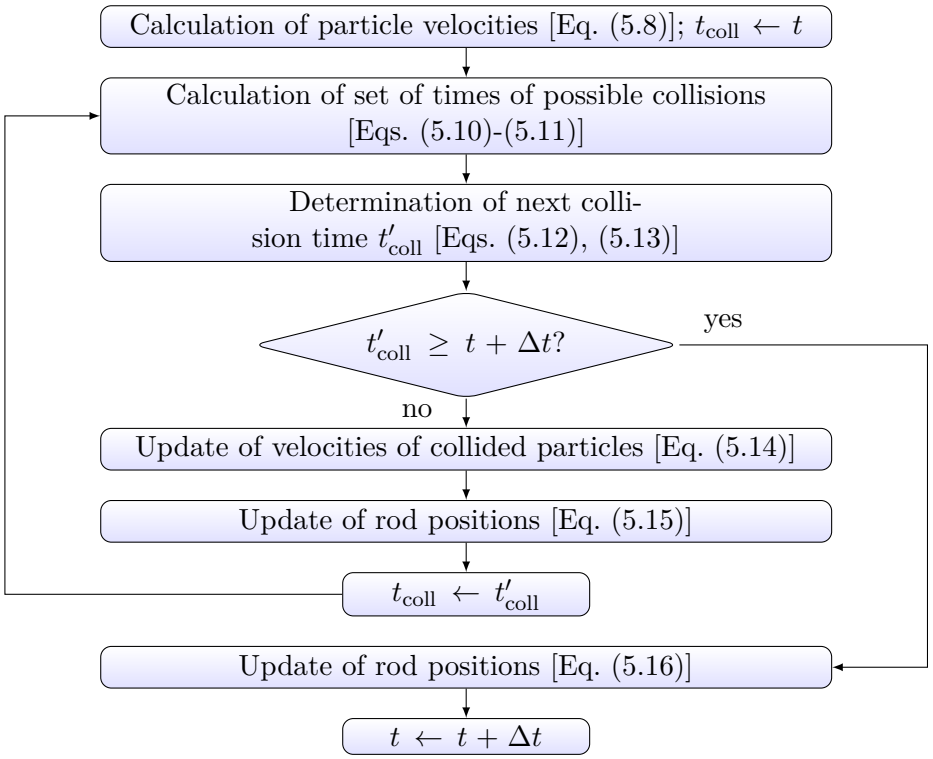

Figure 5.1: The event-driven algorithm for hard particles based on totally elastic collisions.

$$u_i(t'_{\text{coll}}) = u_{i+1}(t'_{\text{coll}}) = \frac{u_i(t_{\text{coll}}) + u_{i+1}(t_{\text{coll}})}{2}, \tag{5.17}$$

and the algorithm for elastic collisions can be thus adapted for the inelastic ones, see Fig. 5.2. However, in the case of inelastic collisions this algorithm can be substantially improved with respect to the computational time by using the principles of cluster dynamics, described in the Sec. 3.3.1. Here we also generalize these principles for the case of non-zero noise, with the particle (pseudo)velocity given by Eq. (5.8) as a generalization of the zero-noise particle velocity given by Eq. (3.15b). In what follows, we use the notation from Sec. 3.3.1.

To implement the principles of cluster dynamics, we consider all particles in the system as clusters, as illustrated in Fig. 5.3. Cluster identification can change and therefore needs to be updated either due to collisions within the time step or due to recalculation of particle velocities at the beginning of each time step. In other words, during the time

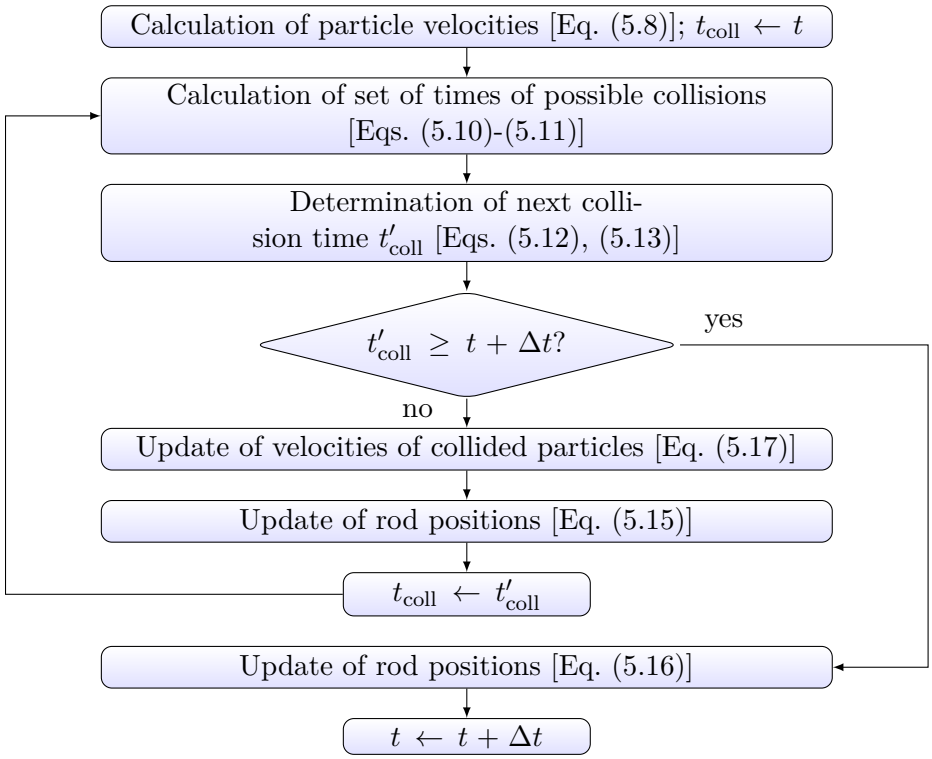

Figure 5.2: The simplest version of the event-driven algorithm for hard particles based on totally inelastic collisions.

step, clusters can only collide with each other, while at the beginning of a new time step, all clusters from the previous time step are guaranteed to be particles in contact, but not necessarily clusters. Thus, cluster fragmentation can occur only at the beginning of the time step, and cluster merging can occur only during the rest of the time interval. However, in the simplest version of the algorithm depicted in Fig. 5.2, this fragmentation is obviously ineffective in terms of computational time, as it does not utilize information about particles being in contact from the previous time step and requires recalculating cluster identification from scratch at each time step.

To perform the fragmentation in a more efficient way, we suggest the following procedure. Each n-cluster consisting of n particles, where $n > 1$, is divided into two fragments, n_1 and n_2, where $n_1 + n_2 = n$. From all possible fragmentations, we choose that one which satisfies the following condition:

$$n_1 = \underset{1 \leq \tilde{n}_1 \leq n-1}{\operatorname{argmax}} \{\bar{u}_{\tilde{n}_2} - \bar{u}_{\tilde{n}_1}\}, \tag{5.18}$$

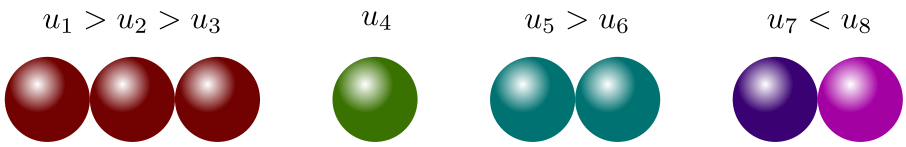

Figure 5.3: An example of cluster identification for 8 particles. The conditions on velocities u_1, u_2, u_3 and u_5, u_6 of particles being in contact correspond to the conditions (3.17a), (3.18) of cluster formation. The condition on velocities u_7, u_8 of particles being in contact corresponds to the condition (3.19) of fragmentation, or independent propagation. Single particle with velocity u_4 is the 1-cluster. The particles belonging to the same cluster are marked with the same color.

with $\bar{u}_{n_1}$, $\bar{u}_{n_2}$ determined by Eq. (3.18b). If $\bar{u}_{n_2} - \bar{u}_{n_1} > 0$, the fragmentation is accepted. If the choice of maximum in Eq. (5.18) is not unique, we arbitrarily select one of the possible values for n_1. The fragmentation procedure is repeated for the cluster fragments until no further fragmentation can be achieved. Velocities of clusters and their particles are calculated directly by Eq. (3.18b).

If the suggested procedure is valid, it should lead to the correct unique cluster identification that satisfies conditions (3.17a), (3.18) and (3.19). To prove the procedure validity, we use mathematical induction. In what follows we consider the fragmentation of a single n-cluster, as fragmentation of multiple independent clusters is performed in the same way.

Base case of cluster size $n = 2$. As fragmentation with $n_1 = 1$ is the only possible one, the fragmentation condition (5.18) is nothing else but Eq. (3.19), so that the fragmentation is performed correctly.

Induction step: if the introduced procedure gives the correct fragmentation for an n-cluster, then it gives the correct fragmentation for the $(n+1)$-cluster.

Let us consider an $(n+1)$-cluster and divide it into two fragments, n_1 and n_2, with $n_1 + n_2 = n + 1$. If $\bar{u}_{n_2} - \bar{u}_{n_1} \leq 0$, then there is no fragmentation, which satisfies the conditions (3.17a), (3.18) and (3.19). Otherwise, both n_1 and n_2 have size less than or equal to n, so their further fragmentation is performed correctly due to the assumption of the induction step. To complete the proof, we need to show that the original split of the $(n+1)$-cluster into an n_1-cluster and n_2-cluster is correct with respect to conditions (3.17a), (3.18) and (3.19).

Four scenarios are possible:

1. No further fragmentation.

Similar to the base case, the required conditions (3.17a), (3.18) and (3.19) are satisfied.

2. n_1-cluster splits further into n_{11}-, …, n_{1s}-clusters; n_2-cluster does not split.

From (3.19) we obtain the condition

$$\bar{u}_{n_{1s}} > u_L, \tag{5.19}$$

where u_L denotes the weighted velocity of cluster group n_{11}, …, $n_{1(s-1)}$:

$$u_L \equiv \frac{1}{n_1 - n_{1s}} \sum_{j=1}^{s-1} \bar{u}_{n_{1j}}. \tag{5.20}$$

From Eq. (5.18), we have

$$\bar{u}_{n_2} - \bar{u}_{n_1} \geq \frac{\bar{u}_{n_{1s}} n_{1s} + \bar{u}_{n_2} n_2}{n_2 + n_{1s}} - u_L, \tag{5.21}$$

where $(\bar{u}_{n_{1s}} n_{1s} + \bar{u}_{n_2} n_2)/(n_2 + n_{1s})$ is the weighted velocity of cluster group n_{1s}, n_2. The left part of the inequality corresponds to the partition according to Eq. (5.18), and the right part corresponds to the choice $\tilde{n}_1 = n_1 - n_{1s}$ in the subargument expression of Eq. (5.18).

The weighted velocity of cluster group $n_{11}, \ldots, n_{1s}$ (former n_1-cluster) can be rewritten analogous to Eq. (5.20):

$$\bar{u}_{n_1} = \frac{u_L(n_1 - n_{1s}) + \bar{u}_{n_{1s}} n_{1s}}{n_1}. \tag{5.22}$$

By using this relation and relation (5.20), we rewrite Eq. (5.21) as

$$\frac{\bar{u}_{n_2} - \bar{u}_{n_{1s}}}{n_2 + n_{1s}} - \frac{\bar{u}_{n_{1s}} - u_L}{n_1} \geq 0, \tag{5.23}$$

which, together with (5.19), reads

$$u_L < \bar{u}_{n_{1s}} \leq \frac{\bar{u}_{n_2} n_1 + u_L(n_2 + n_{1s})}{n_1 + n_2 + n_{1s}}. \tag{5.24}$$

Using the inequality (5.19),

$$\bar{u}_{n_{1s}} \leq \frac{\bar{u}_{n_2} n_1 + u_L(n_2 + n_{1s})}{n_1 + n_2 + n_{1s}} < \frac{\bar{u}_{n_2} n_1 + \bar{u}_{n_{1s}}(n_2 + n_{1s})}{n_1 + n_2 + n_{1s}}, \tag{5.25}$$

$$0 < \frac{n_1(\bar{u}_{n_2} - \bar{u}_{n_{1s}})}{n_1 + n_2 + n_{1s}}, \tag{5.26}$$

we obtain that condition $\bar{u}_{n_{1s}} < \bar{u}_{n_2}$ is fulfilled, so the initial split as well as all the following fragmentations are performed in a correct way.

3. n_2-cluster splits further into n_{21}-, ..., n_{2t}-clusters; n_1-cluster does not split.

The proof is analogous to that in the preceding case.

From (3.19) we obtain the condition

$$\bar{u}_{n_{21}} < u_R, \tag{5.27}$$

where u_R denotes the weighted velocity of cluster group $n_{21}, \ldots, n_{2t}$:

$$u_R \equiv \frac{1}{n_2 - n_{21}} \sum_{j=2}^{t} \bar{u}_{n_{2j}}. \tag{5.28}$$

From Eq. (5.18) we obtain the condition

$$\bar{u}_{n_2} - \bar{u}_{n_1} \geq u_R - \frac{\bar{u}_{n_1} n_1 + \bar{u}_{n_{21}} n_{21}}{n_1 + n_{21}}, \tag{5.29}$$

where $(\bar{u}_{n_1} n_1 + \bar{u}_{n_{21}} n_{21})/(n_1 + n_{21})$ is the weighted velocity of cluster group n_1, n_{21}. The left part of the inequality corresponds to the partition according to Eq. (5.18), and the right part corresponds to the choice $\tilde{n}_2 = n_2 - n_{21}$ in the subargument expression of Eq. (5.18).

The weighted velocity of cluster group n_{21}, n_{2t} (former cluster n_2) can be rewritten analogous to Eq. (5.28):

$$\bar{u}_{n_2} = \frac{\bar{u}_{n_{21}} n_{21} + u_R (n_2 - n_{21})}{n_2}. \tag{5.30}$$

By using this relation and relation (5.28), we rewrite Eq. (5.29) as

$$\frac{\bar{u}_{n_{21}} - u_R}{n_2} - \frac{\bar{u}_{n_1} - \bar{u}_{n_{21}}}{n_1 + n_{21}} \geq 0, \tag{5.31}$$

which, together with (5.27), reads

$$\bar{u}_{n_{21}} \geq \frac{\bar{u}_{n_1} n_2 + u_R (n_1 + n_{21})}{n_1 + n_2 + n_{21}} > \frac{\bar{u}_{n_1} n_2 + \bar{u}_{n_{21}} (n_1 + n_{21})}{n_1 + n_2 + n_{21}}, \tag{5.32}$$

$$0 > \frac{(\bar{u}_{n_1} - \bar{u}_{n_{21}}) n_2}{n_1 + n_2 + n_{21}}. \tag{5.33}$$

Accordingly, condition $\bar{u}_{n_1} < \bar{u}_{n_{21}}$, is fulfilled and the first split is performed correctly.

4. Both clusters are split further. Here the notation from cases 2-3 is used.

Inequalities analogous to those in cases 2 and 3 read:

$$u_L < \bar{u}_{n_{1s}}, \tag{5.34a}$$

$$u_R > \bar{u}_{n_{21}}, \tag{5.34b}$$

$$\left(\frac{\bar{u}_{n_{21}} n_{21} + u_R(n_2 - n_{21})}{n_2} - \frac{\bar{u}_{n_{1s}} n_{1s} + u_L(n_1 - n_{1s})}{n_1}\right) \geq \left(\frac{\bar{u}_{n_{21}} n_{21} + u_R(n_2 - n_{21}) + \bar{u}_{n_{1s}} n_{1s}}{n_2 + n_{1s}} - u_L\right). \tag{5.34c}$$

The inequality (5.34c) can be rewritten as

$$\frac{(u_R - \bar{u}_{n_{21}})(n_2 - n_{21})}{n_2} - \frac{\bar{u}_{n_{21}}(n_{21} - n_{1s} - n_2) + u_R(n_2 - n_{21})}{n_2 + n_{1s}} + \frac{u_L n_{1s}}{n_1} \geq \frac{\bar{u}_{n_{1s}} n_{1s}(n_1 + n_2 + n_{1s})}{n_1(n_2 + n_{1s})}. \tag{5.35}$$

By applying to it inequalities (5.34a),

$$\frac{(u_R - \bar{u}_{n_{21}})(n_2 - n_{21})}{n_2} - \frac{\bar{u}_{n_{21}}(n_{21} - n_{1s} - n_2) + u_R(n_2 - n_{21})}{n_2 + n_{1s}} + \frac{\bar{u}_{n_{1s}} n_{1s}}{n_1} > \frac{\bar{u}_{n_{1s}} n_{1s}(n_2 + n_{1s} + n_1)}{n_1(n_2 + n_{1s})}, \tag{5.36}$$

and (5.34b),

$$\frac{\bar{u}_{n_{21}} n_{1s}}{n_2 + n_{1s}} + \frac{\bar{u}_{n_{1s}} n_{1s}}{n_1} > \frac{\bar{u}_{n_{1s}} n_{1s}(n_1 + n_2 + n_{1s})}{n_1(n_2 + n_{1s})}, \tag{5.37}$$

we obtain

$$\frac{\bar{u}_{n_{21}}}{n_2 + n_{1s}} + \frac{\bar{u}_{n_{1s}}}{n_1} > \frac{\bar{u}_{n_{1s}}(n_2 + n_{1s} + n_1)}{n_1(n_2 + n_{1s})} = \frac{\bar{u}_{n_{1s}}}{n_2 + n_{1s}} + \frac{\bar{u}_{n_{1s}}}{n_1}, \tag{5.38}$$

Hence the condition $\bar{u}_{n_{1s}} < \bar{u}_{n_{21}}$ is fulfilled and the first split is performed correctly. This completes the proof by induction.

The flow diagram of algorithm based on this fragmentation procedure is shown in Fig. 5.4.

In all algorithms presented and implemented in this thesis, we utilize a time step of $D\Delta t/\lambda^2 = 10^{-5}$-$10^{-4}$ in the Euler scheme. This time step has an optimal balance between computational efficiency and accuracy since a further decrease does not significantly affect the results presented.

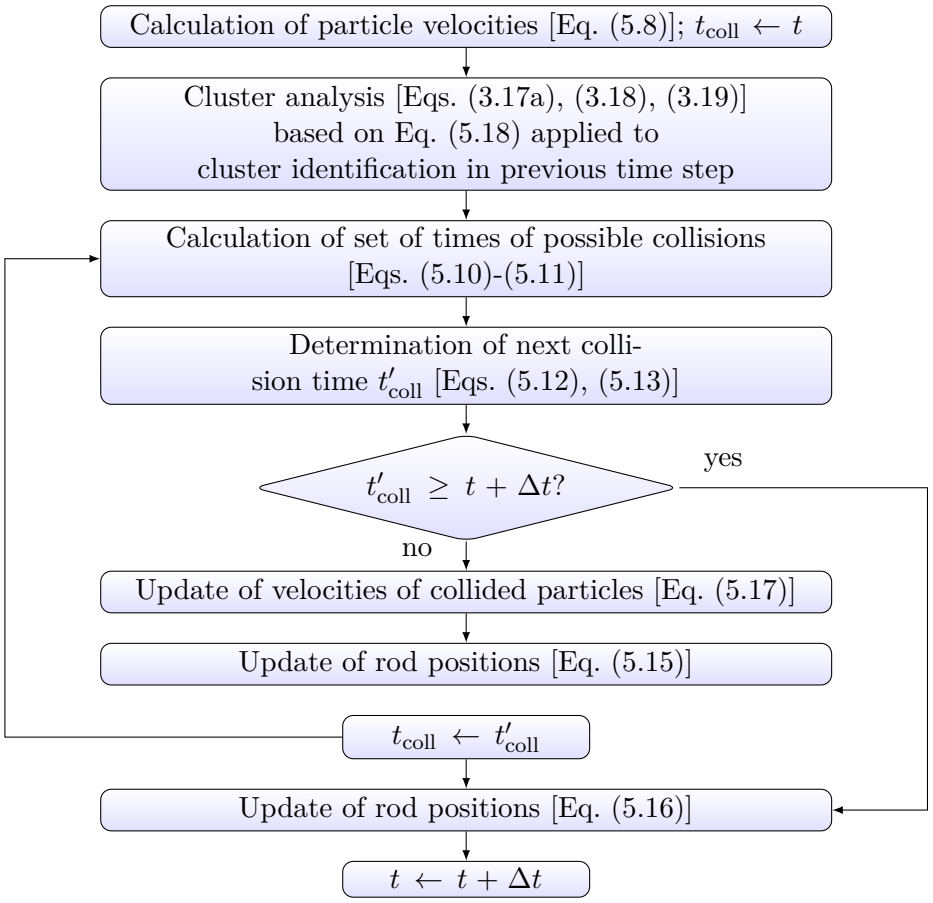

Figure 5.4: Cluster dynamics-based event-driven algorithm for hard particles with completely inelastic collisions.

5.5 Extracting quantities from simulations

Density profile

To calculate the density profile, we implement Eq. (2.8) by discretization of the space domain and turning Dirac delta into Kronecker delta as has been done in Sec. 5.2:

$$\varrho(x_a) = \frac{1}{\Delta_x} \left\langle \sum_{i=1}^{N} \delta_{\mathcal{X},x_i} \right\rangle_{\tau}, \tag{5.39}$$

where Δ_x is a spatial resolution, x_α is a dicretized coordinate,

$$x_a = a\Delta_x,\ a \in \mathbb{N}, \tag{5.40}$$

and $\mathcal{X}$ is a space interval $[x_a - \Delta_x/2, x_a + \Delta_x/2[$. Thus, the Kronecker delta $\delta_{\mathcal{X},x_i}$ is equal to 1 in case $x_i \in \mathcal{X}$, and equal to 0 otherwise. Here, the ensemble average $\langle \ldots \rangle_\tau$ is an average over all time-discretized states between the initial system state at time 0 and the final system state at time τ.

Equation (5.39) thus reads:

$$\varrho(x_a, \tau) = \frac{\Delta t}{(\tau + \Delta t)\Delta_x} \sum_{j=0}^{\tau/\Delta t} \sum_{i=1}^{N} \delta_{\mathcal{X},x_i(j\Delta t)}. \tag{5.41}$$

In the limit of large τ, the system reaches a steady-state density profile. Therefore, Equation (5.41) enables us to determine the density at position $x = x_a + \Delta_x/2$ with a predetermined level of accuracy. In the present thesis, we use $\Delta_x = 10^{-3}\lambda$, $\tau = 10^{11}\Delta t$, and average the density profile over all spatial periods, thus exploiting its periodicity in the steady-state, where $\varrho(x) = \varrho(x + \lambda)$.

An analogous procedure is also applicable for densities of higher order, like the two particle density $\varrho^{(2)}(x, y, t)$.

Mean interaction force

The mean interaction force is

$$f^{\text{int}}(x) = \left\langle \sum_{i=1}^{N} \delta(x - x_i) f^{\text{int}}(x_i) \right\rangle_\tau \tag{5.42}$$

Knowing the particle position $x_i(t)$ at time t, we can predict the particle position at time $t + \Delta t$, if no interaction would occur within time interval $[t, t + \Delta t[$:

$$\tilde{x}_i(t + \Delta t) = x_i(t) + u_i \Delta t. \tag{5.43}$$

Here, u_i is given by Eq. (5.8). However, due to the interaction force the real position at time $t + \Delta t$ can be different. By taking the interaction force $f_i^{\text{int}} = f_i^{\text{int}}(t)$ into account as it is done in Eq. (5.9), we obtain:

$$x_i(t + \Delta t) = x_i(t) + u_i \Delta t + \mu f_i^{\text{int}}(t) \Delta t \tag{5.44}$$

Accordingly, we can determine the interaction force at position x_i in time interval $[t; t+\Delta t[$ from the particle configuration at the end of a time step:

$$f_i^{\text{int}}(t) = \frac{x_i(t+\Delta t) - \tilde{x}_i(t+\Delta t)}{\mu \Delta t}. \tag{5.45}$$

We substitute this expression into Eq. (5.42) for the mean interaction force and perform the average $\langle \ldots \rangle_\tau$ analogous to the procedure described for the density in Eqs. (5.39)-(5.41). This yields

$$f^{\text{int}}(x_a, \tau) = \frac{\Delta t}{(\tau + \Delta t)\Delta_x} \sum_{j=0}^{\tau/\Delta t} \sum_{i=1}^{N} \delta_{\mathcal{X}, x_i(j\Delta t)} f_i^{\text{int}}(j\Delta t). \tag{5.46}$$

Current

To calculate the current $j(x_a)$ at the discrete coordinate position x_a, we measure the rate of particle flow. This rate refers to the number of particles passing through the corresponding position per unit of time. The counting process at each time step is as follows: for each particle i that was located at position $x_i(t - \Delta t) < x_a$ in the previous time step and has now moved to a position $x_i(t) \geq x_a$, we increment the particle counter by one. Conversely, for each particle that was at position $x_i(t - \Delta t) \geq x_a$ in the previous time step and has now moved to a position $x_i(t) < x_a$, we decrement the particle counter by one. An indication of the establishment of a steady-state regime is the homogeneity of the current throughout the system.

Soliton velocity

We define soliton position as the position of the leftmost particle in a cluster in the zero-noise limit, or as the position of the leftmost particle in a doubly occupied potential well for non-zero noise. Based on this information, we determine the soliton velocity using the standard method of calculating the ratio of the distance traveled to the time required to pass this distance.

5.6 Summary notes

This chapter presents various methods for simulating Brownian dynamics of particles interacting through hardcore or softcore potentials in one dimensional space. These methods can be applied to particles in arbitrary external force fields, including random forces from

fluid environments. The proposed algorithms for hard particles are based on event-driven dynamics, which involve either totally elastic or totally inelastic collisions. Limits of applicability are provided for both algorithms, with the inelastic collision algorithm being particularly important for studying Brownian solitons based on cluster dynamics. Particle interactions beyond hardcore can be included if the corresponding interaction forces are continuous functions of the particle coordinates. However, additional considerations are required for other types of interactions, such as the Baxter's sticky hard-sphere interaction [89], which is important for describing adhesive forces. For such potentials an algorithm based on inelastic collisions is preferable due to the natural formation of clusters.

5.6.1 Binary collision merging

Further improvement of the suggested algorithm based on totally inelastic collisions can be achieved by exploiting the fact that collided particles propagate as the whole, i.e. as a cluster, and by taking into account the momentum conservation during the inelastic collisions. Here we demonstrate the possibility of such improvement for a case where only two clusters n_1, n_2 collide within the time step interval $[t, t + \Delta t[$.

We put these clusters in the initial configuration at time t in contact, i.e. merge them. The velocity $\bar{u}$ of the merged cluster is

$$\bar{u} = \frac{\bar{u}_1 n_1 + \bar{u}_2 n_2}{n_1 + n_2}, \tag{5.47}$$

and the position x at time t of the merged cluster is

$$x = \frac{x_1 n_1 + x_2 n_2}{n_1 + n_2}, \tag{5.48}$$

where x_1 and x_2 are the positions of the clusters at time t. The illustration of this *binary collision merging* procedure is shown in Fig. 5.5.

The binary collision merging procedure conserves both the center of mass and momentum of the merged clusters. As a result, this procedure does not affect the cluster configuration *after* the collision time but only alters the history of the cluster *before* the collision, see the illustration in Fig. 5.5.

The advantage of this procedure is that it eliminates the necessity to recalculate the particle configuration after each collision within the time step. This can significantly reduces the simulation time, particularly in systems with large coverage $\bar{\rho}\sigma$ and a high rate of collisions. However, the implementation of the algorithm require a future development of a generalized version of the binary collision merging procedure. This extended procedure

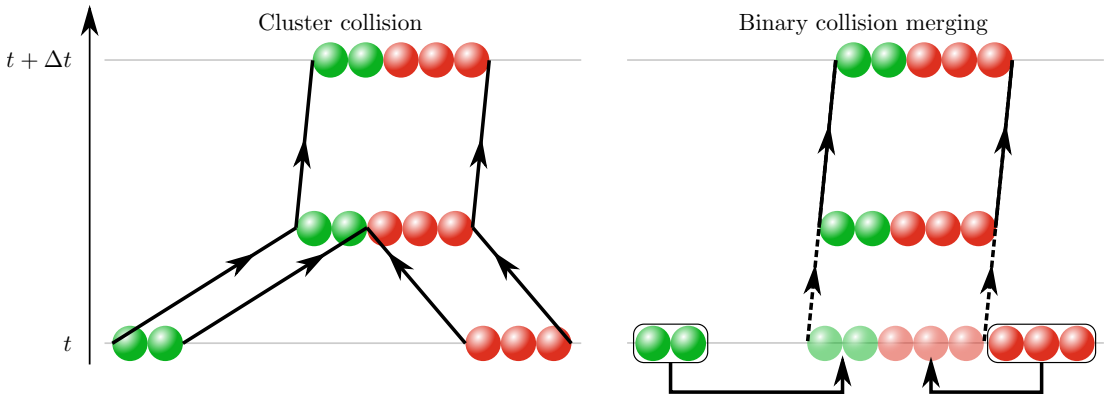

Figure 5.5: Illustration of the real cluster collision and illustration of the binary collision merging. The trajectories of the left and right cluster borders are marked by arrows in the time interval between t and $t + \Delta t$. The merging procedure in the right panel is indicated by shaped arrows at the initial time. In the right panel, particles of the merged cluster at time t are indicated with pale colors, and the trajectories of the left and right borders of the merged cluster before the collision are shown by dashed arrows. Both procedures result in the same particle configuration.

should accommodate scenarios where more than two clusters collide within a single time step.

6 Conclusion and outlook

In this thesis, we have investigated crowding effects at high densities within spatial confinement based on Brownian asymmetric simple exclusion process (BASEP), where particles are modeled as hard spheres. A key finding was that solitons emerge in such systems, which are thermally activated or persistent for overcrowded systems. These solitons manifest themselves as solitary cluster waves hat propagate wihtout dispersion. When examining types of particle interactions other than hardcore, it can be expected that qualitative changes of the overall transport behavior may occur when particles stick to or partially penetrate each other. Examples of such particle interactions in real systems are interpenetrating polymers or protein fragments with attractive forces arising from van der Waals interactions or hydrogen bonding.

As a first step, we have developed and investigated a model with particles exhibiting softness, therefore allowing the particles to interpenetrate or even pass each other. We have demonstrated that the passage of particles reveals new features that do not have counterparts in the BASEP. To account for stickiness by attractive forces, we have started studies recently [89, 90] based on Baxter's model of adhesive hard spheres [88].

An open question is whether Brownian solitons occur in particle systems with interactions other than hardcore. For adhesive hard spheres, one can expect that cluster formations of Brownian solitons would even be facilitated, thus expanding the range of conditions under which propagating solitons can emerge compared to that for the hardcore interaction. The presence of adhesive interactions can also have an impact on the repulsive interaction between solitons in the BASEP. It is probable that under certain circumstances, two solitons may overcome the repulsive barrier between them and adhere to each other. This is overall a compelling and challenging topic for future studies, given that the interaction between solitons has a complex many-body nature.

Brownian solitons have been experimentally observed when driving colloidal particles through a vortex of optical traps by a traveling wave [108]. In these systems, it has been demonstrated that hydrodynamic interactions play a significant role at lower densities [75]. Thus, it is reasonable to expect that these hydrodynamic interactions become less relevant in crowded systems. It is also of practical interest to determine whether solitons would

occur in higher dimensions, such as 2D or 3D, when particles experience reduced spatial confinement. For instance, in the experiment described in Ref. [108], the particle motion is not strictly one-dimensional, but may exhibit fluctuations in the radial direction. Further investigations of this question are running and include numerical simulations of particle dynamics with hydrodynamic interactions in a 2D geometry [182].

The experiment confirming soliton existence in real systems described in Ref. [108] has also demonstrated the relevance and applicability of the seemingly artificial constant external drag force, as employed in BASEP, to real-world systems. In this experiment, the external drag force is generated by the viscous friction exerted on colloidal particles suspended in highly deionized water and manipulated using optical tweezers. The particles experience resistance from the surrounding fluid, resulting in the drag force that influences their motion. Regarding the drag force itself, it would be intriguing to explore the case where this force is varying. In the experimental realization, such force variation can be implemented as e.g. an amplitude modulation of the beam used to generate the optical tweezers.

In summary, we would like to emphasize that the simulation and theoretical approaches developed and implemented in this thesis, along with the corresponding consistent experimental realizations, constitute a powerful toolbox for investigating dynamics in crowded systems. These tools have the potential to be applied to a wide range of problems, including but not limited to microfluidics, polymer and protein dynamics in confined geometries such as channels, pores, and nanotubes.

Appendix

Here we provide scaling factors for basic quantities shown in figures of the present thesis to be dimensionless.

Length

As unit of length, we use the wavelength λ of the external potential (2.4). This applies to the parameters x, L, r and ς.

Energy

We use thermal energy $k_{\mathrm{B}}T$ as unit of energy. This applies to potential amplitudes U_0 and V_0.

Time

As is evident from the Langevin equation (5.7), $\mu U_0 t/\lambda$ should be the unit of length. Since $[U_0] = [k_{\mathrm{B}}T]$, time can be measured either in units of $\lambda^2/\mu k_{\mathrm{B}}T = \lambda^2/D$, or in the zero-noise limit $D = 0$ it can be measured in units of $\lambda^2/\mu U_0$.

Once we establish measurement units for length, energy, and time, we can subsequently derive measurement units for various other quantities. For example, we obtain U_0/λ or alternatively, $k_{\mathrm{B}}T/\lambda$ as the measurement units for force, and D/λ or $\mu U_0/\lambda$ as the measurement units for velocity. As for particle current, if we compare it with that for independent particles, from Eq. (2.27) we obtain the current measurement unit v_0/λ or $v_0\bar{\rho}/\lambda$ if we study the current for the fixed filling factor $\bar{\rho}$. If we are not interested in comparing the particle current with that for independent particles, we obtain $\mu U_0/\lambda^2$ as the current unit measure. Here, the temperature-independent measurement unit is preferable since the current is compared between the non-zero and zero-noise limit, i.e. for various temperature regimes.

References

[1] G. Chirico and J. Langowski, Biopolymers **34**, 415 (1994).

[2] J.-F. Mercier and G. W. Slater, Biophys. J. **89**, 32 (2005).

[3] H. Pei, S. Allison, B. M. H. Haynes, and D. Augustin, J. Phys. Chem. B **113**, 2564 (2009).

[4] H. Löwen, J.-P. Hansen, and J.-N. Roux, Phys. Rev. A **44**, 1169 (1991).

[5] P. N. Segrè, O. P. Behrend, and P. N. Pusey, Phys. Rev. E **52**, 5070 (1995).

[6] S. H. Northrup and H. P. Erickson, Proc. Natl. Acad. Sci. **89**, 3338 (1992).

[7] R. R. Gabdoulline and R. C. Wade, J. Mol. Biol. **306**, 1139 (2001).

[8] S. Rostek and R. Schöbel, Econ. Model. **30**, 30 (2013).

[9] C. A. Holt and J. K. Goeree, *Stochastic Game Theory: For Playing Games, Not Just for Doing Theory*, Virginia Economics Online Papers 306 (University of Virginia, Department of Economics, 1999).

[10] A. Antonov, A. Leonidov, and A. Semenov, Physica A **561**, 125305 (2021).

[11] A. Antonov, A. Leonidov, and A. Semenov, Phys. Rev. E **108**, 024134 (2023).

[12] E. Ben-Jacob, O. Schochet, A. Tenenbaum, I. Cohen, A. Czirók, and T. Vicsek, Nature **368**, 46 (1994).

[13] T. Vicsek, *Fluctuations and scaling in biology* (Oxford University Press New York, 2001).

[14] J. Kärger and D. M. Ruthven, Ber. Bunsenges. Phys. Chem. **97**, 146 (1993).

[15] K. Hahn, J. Kärger, and V. Kukla, Phys. Rev. Lett. **76**, 2762 (1996).

[16] M. Van de Voorde and B. Sels, eds., *Nanotechnology in Catalysis: Applications in the Chemical Industry, Energy Development, and Environment Protection* (Wiley-VCH, Weinheim, 2017).

[17] C.-Y. Cheng and C. R. Bowers, ChemPhysChem **8**, 2077 (2007).

[18] B. Hille, *Ionic Channels of Excitable Membranes*, 3rd ed. (Sinauer Associates, Sunderland MA, 2001).

[19] R. Lipowsky, S. Klumpp, and T. M. Nieuwenhuizen, Phys. Rev. Lett. **87**, 108101 (2001).

[20] E. Frey and K. Kroy, *Annalen der Physik*, Ann. Phys. **14**, 20 (2005).

[21] C. T. MacDonald, J. H. Gibbs, and A. C. Pipkin, Biopolymers **6**, 1 (1968).

[22] M. Hartmann, Chem. Mater. **17**, 4577 (2005).

[23] H. H. P. Yiu, C. H. Botting, N. P. Botting, and P. A. Wright, Phys. Chem. Chem. Phys. **3**, 2983 (2001).

[24] S. Zeng, J. Chen, X. Wang, G. Zhou, L. Chen, and C. Dai, J. Phys. Chem. C **122**, 27681 (2018).

[25] M. Ma, F. Grey, L. Shen, M. Urbakh, S. Wu, J. Z. Liu, Y. Liu, and Q. Zheng, Nat. Nanotechnol. **10**, 692 (2015).

[26] M. A. Shannon, P. W. Bohn, M. Elimelech, J. G. Georgiadis, B. J. Mariñas, and A. M. Mayes, Nature **452**, 301 (2008).

[27] D. Helbing, P. Molnár, I. J. Farkas, and K. Bolay, Environ. Plann. B: Plann. Des. **28**, 361 (2001).

[28] D. Chowdhury, L. Santen, and A. Schadschneider, Phys. Rep. **329**, 199 (2000).

[29] A. Schadschneider, D. Chowdhury, and K. Nishinari, *Stochastic Transport in Complex Systems: From Molecules to Vehicles*, 3rd ed. (Elsevier Science, Amsterdam, 2010).

[30] T. Chou, K. Mallick, and R. K. P. Zia, Rep. Prog. Phys. **74**, 116601 (2011).

[31] A. B. Kolomeisky, J. Phys.: Condens. Matter **25**, 463101 (2013).

[32] C. Appert-Rolland, M. Ebbinghaus, and L. Santen, Phys. Rep. **593**, 1 (2015).

[33] A. Jindal, A. B. Kolomeisky, and A. K. Gupta, J. Stat. Mech.: Theory Exp. **2020**, 043206 (2020).

[34] G. Shen, X. Fan, and Z. Ruan, Chaos **30**, 023103 (2020).

[35] R. A. Blythe and M. R. Evans, J. Phys. A: Math. Theor. **40**, R333 (2007).

[36] M. R. Evans, EPL (Europhysics Letters) **36**, 13 (1996).

[37] R. J. Concannon and R. A. Blythe, Phys. Rev. Lett. **112**, 050603 (2014).

[38] J. Krug, Phys. Rev. Lett. **67**, 1882 (1991).

[39] A. Parmeggiani, T. Franosch, and E. Frey, Phys. Rev. Lett. **90**, 086601 (2003).

[40] L. Bertini, A. De Sole, D. Gabrielli, G. Jona-Lasinio, and C. Landim, Phys. Rev. Lett. **94**, 030601 (2005).

[41] A. Lazarescu, J. Phys. A: Math. Theor. **48**, 503001 (2015).

[42] Y. Baek, Y. Kafri, and V. Lecomte, Phys. Rev. Lett. **118**, 030604 (2017).

[43] V. Popkov, A. Schadschneider, J. Schmidt, and G. M. Schütz, PNAS **112**, 12645 (2015).

[44] Z. Chen, J. de Gier, I. Hiki, and T. Sasamoto, Phys. Rev. Lett. **120**, 240601 (2018).

[45] K. K. Mon and J. K. Percus, J. Phys. Chem. C **111**, 15995 (2007).

[46] P. S. Burada, P. Hänggi, F. Marchesoni, G. Schmid, and P. Talkner, ChemPhysChem **10**, 45 (2009).

[47] M. Mangeat, T. Guérin, and D. S. Dean, J. Chem. Phys. **149**, 124105 (2018).

[48] C. Hilty and M. Winterhalter, Phys. Rev. Lett. **86**, 5624 (2001).

[49] J. J. Kasianowicz, T. L. Nguyen, and V. M. Stanford, PNAS **103**, 11431 (2006).

[50] S. D. Goldt and E. M. Terentjev, J. Chem. Phys. **141**, 224901 (2014).

[51] A. Ashkin, Phys. Rev. Lett. **24**, 156 (1970).

[52] A. Ashkin, Science **210**, 1081 (1980).

[53] A. Ashkin, J. M. Dziedzic, J. E. Bjorkholm, and S. Chu, Opt. Lett. **11**, 288 (1986).

[54] A. Ashkin, J. M. Dziedzic, and T. Yamane, Nature **330**, 769 (1987).

[55] A. Ashkin, Proc. Natl. Acad. Sci. **94**, 4853 (1997).

[56] A. V. Arzola, M. Villasante-Barahona, K. Volke-Sepúlveda, P. Jákl, and P. Zemánek, Phys. Rev. Lett. **118**, 138002 (2017).

[57] M. J. Skaug, C. Schwemmer, S. Fringes, C. D. Rawlings, and A. W. Knoll, Science **359**, 1505 (2018).

[58] C. Schwemmer, S. Fringes, U. Duerig, Y. K. Ryu, and A. W. Knoll, Phys. Rev. Lett. **121**, 104102 (2018).

[59] R. Stoop, A. Straube, and P. Tierno, Nano Lett. **19**, 433 (2019).

[60] K. Misiunas and U. F. Keyser, Phys. Rev. Lett. **122**, 214501 (2019).

[61] T. Tsuji, R. Nakatsuka, K. Nakajima, K. Doi, and S. Kawano, Nanoscale **12**, 6673 (2020).

[62] R. Nakatsuka, S. Yanai, K. Nakajima, K. Doi, and S. Kawano, J. Phys. Chem. C **125**, 9507 (2021).

[63] T. Tsuji, K. Doi, and S. Kawano, J. Photochem. Photobiol. C **52**, 100533 (2022).

[64] M. Tassieri, R. M. L. Evans, R. L. Warren, N. J. Bailey, and J. M. Cooper, New J. Phys. **14**, 115032 (2012).

[65] R. M. Robertson-Anderson, ACS Macro Lett. **7**, 968 (2018).

[66] E. Townes-Anderson, R. St Jules, D. Sherry, J. Lichtenberger, and M. Hassanain, Mol. Vis. **4**, 12 (1998).

[67] I. C. D. Lenton, E. K. Scott, H. Rubinsztein-Dunlop, and I. A. Favre-Bulle, Front. Bioeng. Biotechnol. **8**, (2020).

[68] M. Wang, H. Yin, R. Landick, J. Gelles, and S. Block, Biophys. J. **72**, 1335 (1997).

[69] T. Strick, J.-F. Allemand, V. Croquette, and D. Bensimon, Prog. Biophys. **74**, 115 (2000) .

[70] C. Renaut, J. Dellinger, B. Cluzel, T. Honegger, D. Peyrade, E. Picard, F. de Fornel, and E. Hadji, Appl. Phys. Lett. **100**, 101103 (2012).

[71] D. G. Grier, Curr. Opin. Colloid Interface Sci. **2**, 264 (1997).

[72] A. Magazzú, D. Spadaro, M. G. Donato, R. Sayed, E. Messina, C. D'Andrea, A. Foti, B. Fazio, M. A. Iatí, A. Irrera, R. Saija, P. G. Gucciardi, and O. M. Maragó, Rend. Lincei **26**, 203 (2015).

[73] K. Niu, S. Zhao, S. Tao, and F. Wang, Sens. Actuator A Phys. **333**, 113223 (2022).

[74] E. Cereceda-López, D. Lips, A. Ortiz-Ambriz, A. Ryabov, P. Maass, and P. Tierno, Phys. Rev. Lett. **127**, 214501 (2021).

[75] D. Lips, E. Cereceda-López, A. Ortiz-Ambriz, P. Tierno, A. Ryabov, and P. Maass, Soft Matter **18**, 8983 (2022).

[76] K. Saito, S. Okubo, and Y. Kimura, Soft Matter **14**, 6037 (2018).

[77] T. Miyamoto, M. Imai, and N. Uchida, Phys. Rev. E **100**, 032607 (2019).

[78] A. Villada-Balbuena, A. Ortiz-Ambriz, P. Castro-Villarreal, P. Tierno, R. Castañeda Priego, and J. M. Méndez-Alcaraz, Phys. Rev. Res. **3**, 033246 (2021).

[79] W. R. Bauer and W. Nadler, Proc. Natl. Acad. Sci. **103**, 11446 (2006).

[80] M. Kahms, P. Lehrich, J. Hüve, N. Sanetra, and R. Peters, Traffic **10**, 1228 (2009).

[81] P. C. Bressloff and J. M. Newby, Rev. Mod. Phys. **85**, 135 (2013).

[82] N. C. X. Stuhlmüller, T. M. Fischer, and D. de las Heras, Phys. Rev. E **106**, 034601 (2022).

[83] K. Brandner and K. Saito, Phys. Rev. Lett. **124**, 040602 (2020).

[84] V. Holubec and A. Ryabov, J. Phys. A **55**, 013001 (2021).

[85] D. Lips, A. Ryabov, and P. Maass, Phys. Rev. Lett. **121**, 160601 (2018).

[86] D. Lips, A. Ryabov, and P. Maass, Phys. Rev. E **100**, 052121 (2019).

[87] D. Lips, A. Ryabov, and P. Maass, Z. Naturforsch. A **75**, 449 (2020).

[88] R. J. Baxter, J. Chem. Phys. **49**, 2770 (1968).

[89] A. P. Antonov, S. Schweers, A. Ryabov, and P. Maass, Phys. Rev. E **106**, 054606 (2022).

[90] S. Schweers, A. P. Antonov, A. Ryabov, and P. Maass, Phys. Rev. E **107**, L042102 (2023).

[91] A. P. Antonov, A. Ryabov, and P. Maass, J. Chem. Phys. **155**, 184102 (2021).

[92] R. J. Ellis and A. P. Minton, Biol. Chem. **387**, 485 (2006).

[93] A. Soranno, I. Koenig, M. B. Borgia, H. Hofmann, F. Zosel, D. Nettels, and B. Schuler, Biophys. J. **106**, 268a (2014).

[94] Y. Wang, M. Sarkar, A. E. Smith, A. S. Krois, and G. J. Pielak, J. Am. Chem. Soc. **134**, 16614 (2012).

[95] M. Senske, L. Törk, B. Born, M. Havenith, C. Herrmann, and S. Ebbinghaus, J. Am. Chem. Soc. **136**, 9036 (2014).

[96] S. L. Speer, C. J. Stewart, L. Sapir, D. Harries, and G. J. Pielak, Annu. Rev. Biophys. **51**, 267 (2022).

[97] W. M. Aumiller Jr., B. W. Davis, E. Hatzakis, and C. D. Keating, J. Phys. Chem. B **118**, 10624 (2014).

[98] I. Alshareedah, M. M. Moosa, M. Raju, D. A. Potoyan, and P. R. Banerjee, Proc. Natl. Acad. Sci. **117**, 15650 (2020).

[99] T. Skóra, M. N. Popescu, and S. Kondrat, Phys. Chem. Chem. Phys. **23**, 9065 (2021).

[100] J. Poon, M. Bailey, D. Winzor, B. Davidson, and W. Sawyer, Biophys. J. **73**, 3257 (1997).

[101] K. Frykholm, L. K. Nyberg, and F. Westerlund, Integr. Biol. **9**, 650 (2017).

[102] F. Tan, Y. Chen, and N. Zhao, Soft Matter **17**, 1940 (2021).

[103] F. Yao, X. Peng, Z. Su, L. Tian, Y. Guo, and X.-f. Kang, Anal. Chem. **92**, 3827 (2020).

[104] E. Pronina and A. B. Kolomeisky, J. Stat. Mech.: Theory Exp. **2005**, P07010 (2005).

[105] X. Song, C. Jiu-Ju, and L. Fei, Chin. Phys. B **18**, 4613 (2009).

[106] A. G. Thompson, J. Tailleur, M. E. Cates, and R. A. Blythe, J. Stat. Mech.: Theory Exp. **2011**, P02029 (2011).

[107] M. Galanti, D. Fanelli, and F. Piazza, arXiv (2023).

[108] E. Cereceda-López, A. P. Antonov, A. Ryabov, P. Maass, and P. Tierno, preprint (2023).

[109] H. A. Kramers, Physica **7**, 284 (1940).

[110] D. W. Oxtoby, *Crystallization of liquids: a density functional approach* (Elsevier Science Publishers B.V., 1991).

[111] L. Landau and E. Lifshitz, *Fluid Mechanics, Second Edition: Volume 6 (Course of Theoretical Physics)*, Vol. 6 (Butterworth-Heinemann, 1987).

[112] L. Landau and E. Lifshitz, *Statistical Physics, Third Edition: Volume 5 (Course of Theoretical Physics)*, Vol. 5 (Oxford: Pergamon Press, 1980).

[113] N. Laurendeau, *Statistical Thermodynamics: Fundamentals and Applications* (Cambridge University Press, 2005).

[114] H. Risken, *The Fokker-Planck Equation: Methods of Solution and Applications* (Springer-Verlag Berlin, 1985).

[115] J. K. Percus, J. Stat. Phys. **15**, 505 (1976).

[116] D. de las Heras and M. Schmidt, Phys. Rev. Lett. **113**, 238304 (2014).

[117] R. G. Parr and W. Yang, *Density Functional Theory of Atoms and Molecules* (Oxford University Press, 1989).

[118] U. M. B. Marconi and P. Tarazona, J. Chem. Phys. **110**, 8032 (1999).

[119] M. Rauscher, J. Phys.: Condens. Matter **22**, 364109 (2010).

[120] S. van Teeffelen, H. Löwen, and C. N. Likos, J. Phys. Condens. Matter **20**, 404217 (2008).

[121] M. te Vrugt, H. Löwen, and R. Wittkowski, Advances in Physics **69**, 121 (2020).

[122] U. M. B. Marconi and P. Tarazona, J. Phys.: Condens. Matter **12**, A413 (2000).

[123] A. Ryabov, *Stochastic Dynamics and Energetics of Biomolecular Systems*, dissertation, Charles University, Prague (2016).

[124] B. Derrida, Phys. Rep. **301**, 65 (1998).

[125] G. M. Schütz, in *Phase Transitions and Critical Phenomena*, Vol. 19, edited by C. Domb and J. Lebowitz (Academic Press, London, 2001) pp. 1–251.

[126] M. Schmidt and J. M. Brader, J. Chem. Phys. **138**, 214101 (2013).

[127] A. Fortini, D. de las Heras, J. M. Brader, and M. Schmidt, Phys. Rev. Lett. **113**, 167801 (2014).

[128] S. M. Tschopp, S. Hermann, M. Schmidt, and J. M. Brader, Phys. Rev. E **106**, 014115 (2022).

[129] S. M. Tschopp and J. M. Brader, J. Chem. Phys. **157**, 234108 (2022).

[130] F. Sammüller, S. Hermann, and M. Schmidt, Phys. Rev. E **107**, 034109 (2023).

[131] S. M. Tschopp, H. D. Vuijk, and J. M. Brader, arXiv (2023).

[132] A. V. Ivlev, J. Bartnick, M. Heinen, C.-R. Du, V. Nosenko, and H. Löwen, Phys. Rev. X **5**, 011035 (2015).

[133] P. R. Buenzli and R. Soto, Phys. Rev. E **78**, 020102 (2008).

[134] S. Steffenoni, K. Kroy, and G. Falasco, Phys. Rev. E **94**, 062139 (2016).

[135] M. H. Jacobs, Diffusion processes, in *Ergebnisse der Biologie*, edited by K. v. Frisch, R. Goldschmidt, W. Ruhland, and H. Winterstein (Springer Berlin Heidelberg, Berlin, Heidelberg, 1935) pp. 1–160.

[136] R. Zwanzig, J. Phys. Chem. **96**, 3926 (1992).

[137] P. Kalinay and J. K. Percus, J. Chem. Phys. **122**, 204701 (2005).

[138] A. P. Antonov, D. Voráč, A. Ryabov, and P. Maass, New J. Phys. **24**, 093020 (2022).

[139] C. Scalliet, L. Berthier, and F. Zamponi, Nature Communications **10**, 5102 (2019).

[140] D. Lips, R. L. Stoop, P. Maass, and P. Tierno, Commun. Phys. **4**, 224 (2021).

[141] O. M. Braun and Y. S. Kivshar, *The Frenkel-Kontorova Model: Concepts, Methods, and Applications* (Springer Berlin, Heidelberg, 2013).

[142] M. R. Evans, D. P. Foster, C. Godrèche, and D. Mukamel, J. Stat. Phys. **80**, 69 (1995).

[143] P. Bonnin, I. Stansfield, M. C. Romano, and N. Kern, Phys. Rev. E **105**, 034117 (2022).

[144] L. D. Landau and E. M. Lifshitz, *Mechanics. Vol. 1* (Butterworth-Heinemann, 1976).

[145] A. P. Antonov, A. Ryabov, and P. Maass, Phys. Rev. Lett. **129**, 080601 (2022).

[146] J. Clemmens, H. Hess, J. Howard, and V. Vogel, Langmuir **19**, 1738 (2003).

[147] L. Jia, S. G. Moorjani, T. N. Jackson, and W. O. Hancock, Biomed. Microdevices **6**, 67 (2004).

[148] I. Niven, H. S. Zuckerman, and H. L. Montgomery, *An introduction to the theory of numbers* (John Wiley & Sons, 1991).

[149] D. Stein, F. H. J. van der Heyden, W. J. A. Koopmans, and C. Dekker, Proc. Natl. Acad. Sci. **103**, 15853 (2006).

[150] T. Voigtmann, M. Siebenbürger, C. P. Amann, S. U. Egelhaaf, S. Fritschi, M. Krüger, M. Laurati, K. J. Mutch, and K. H. Samwer, Colloid Polym. Sci. **298**, 681 (2020).

[151] J. K. Percus and G. J. Yevick, Phys. Rev. **110**, 1 (1958).

[152] J. D. Weeks, D. Chandler, and H. C. Andersen, J. Chem. Phys. **54**, 5237 (1971).

[153] W. A. Curtin and N. W. Ashcroft, Phys. Rev. A **32**, 2909 (1985).

[154] A. R. Denton and N. W. Ashcroft, Phys. Rev. A **39**, 4701 (1989).

[155] R. Leidl and H. Wagner, J. Chem. Phys. **98**, 4142 (1993).

[156] C. N. Likos, Phys. Rep. **348**, 267 (2001).

[157] J. F. Lutsko, *Recent developments in classical density functional theory* (Elsevier Ltd., 2013).

[158] R. Wittmann, M. Marechal, and K. Mecke, J. Phys. Condens. Matter **28**, 244003 (2016).

[159] T. K. Vanderlick, H. T. Davis, and J. K. Percus, J. Chem. Phys. **91**, 7136 (1989).

[160] B. Bakhti, S. Schott, and P. Maass, Phys. Rev. E **85**, 042107 (2012).

[161] A. Ryabov, D. Lips, and P. Maass, J. Phys. Chem. C **123**, 5714 (2019).

[162] D. Voráč, P. Maass, and A. Ryabov, J. Phys. Chem. Lett. **11**, 6887 (2020).

[163] M. N. Rosenbluth and A. W. Rosenbluth, J. Chem. Phys. **22**, 881 (1954).

[164] B. J. Alder and T. E. Wainwright, J. Chem. Phys. **27**, 1208 (1957).

[165] J. K. Percus, J. Stat. Phys. **28**, 67 (1982).

[166] B. Cichocki and K. Hinsen, Physica A **166**, 473 (1990).

[167] W. Schaertl and H. Sillescu, J. Stat. Phys. **77**, 1007 (1994).

[168] H. Behringer and R. Eichhorn, J. Chem. Phys. **137**, 164108 (2012).

[169] T. Pöschel and T. Schwager, *Computational Granular Dynamics: Models and Algorithms (Scientific Computation)*, 1st ed. (Springer, 2005).

[170] P. Strating, Phys. Rev. E **59**, 2175 (1999).

[171] A. Scala, Phys. Rev. E **86**, 026709 (2012).

[172] T. P. C. van Noije, M. H. Ernst, and R. Brito, Physica A **251**, 266 (1998).

[173] S. Luding, Collisions & contacts between two particles, in *Physics of Dry Granular Media* (Springer Netherlands, Dordrecht, 1998) pp. 285–304.

[174] S. González, D. Risso, and R. Soto, Eur. Phys. J.: Spec. Top. **179**, 33 (2009).

[175] E. Helland, H. Bournot, R. Occelli, and L. Tadrist, Chem. Eng. Sci. **62**, 148 (2007).

[176] J. McMillan, F. Shaffer, B. Gopalan, J. W. Chew, C. Hrenya, R. Hays, S. B. R. Karri, and R. Cocco, Chem. Eng. Sci. **100**, 39 (2013).

[177] A. Cahyadi, A. Anantharaman, S. Yang, S. R. Karri, J. G. Findlay, R. A. Cocco, and J. W. Chew, Chem. Eng. Sci. **158**, 70 (2017).

[178] G. Lois, A. Lemaître, and J. M. Carlson, Europhys. Lett. (EPL) **76**, 318 (2006).

[179] M. Watanabe and D. Tanaka, Comput. Chem. Eng. **54**, 151 (2013).

[180] R. A. Serway and J. W. Jewett, *Physics for scientists and engineers* (Cengage learning, 2018).

[181] A. Scala, T. Voigtmann, and C. De Michele, J. Chem. Phys. **126**, 134109 (2007).

[182] D. Voráč, A. P. Antonov, P. Maass, and A. Ryabov, to be published.

Acknowledgements

First, I would like to thank my doctoral advisor, Professor Philipp Maass, for patiently accompanying and supervising me throughout my work. I am grateful to him for the interesting scientific projects he offered to me, and I highly appreciate his professional interest, numerous discussions and helpful support.

I am also grateful to RNDr. Artem Ryabov for the great collaboration and for evaluating my work as the second examiner, and for kind hospitality during my stays in Charles University in Prague.

Furthermore, I would like to thank all members of our Statistical Physics research group for the enjoyable time we spent together. In particular, I thank Dominik Lips for the initial introduction to the research topic, Marco Bosi for valuable discussions and for our ping-pong matches, So-Kumneth Sim for our language and music conversations.

A big special thanks goes to Sören Schweers from Statistical Physics research group and David Voráč from Charles University for the discussions and publication preparation.

Last but not least, I would like to thank my other colleagues and friends Christoph Schiel, Matthias Gries and Alex Latyshev for our conversations and support during the dissertation process.

Finally, I express my gratitude to my parents and my sister, without whose support I could not have completed my work. And of course, I thank my wife Daria for the wonderful time we have spent together and for her professional and personal support.

Erklärung über die Eigenständigkeit der erbrachten wissenschaftlichen Leistung

Ich erkläre hiermit, dass ich die vorliegende Arbeit ohne unzulässige Hilfe Dritter angefertigt habe. Die aus anderen Quellen direkt oder indirekt übernommenen Daten und Konzepte sind unter Angabe der Quelle gekennzeichnet.

Weitere Personen waren an der inhaltlichen materiellen Erstellung der vorliegenden Arbeit nicht beteiligt. Insbesondere habe ich hierfür nicht die entgeltliche Hilfe von Vermittlungs- bzw. Beratungsdiensten (Promotionsberater oder andere Personen) in Anspruch genommen. Niemand hat von mir unmittelbar oder mittelbar geldwerte Leistungen für Arbeiten erhalten, die im Zusammenhang mit dem Inhalt der vorgelegten Dissertation stehen.

Die Arbeit wurde bisher weder im In- noch im Ausland in gleicher oder ähnlicher Form einer anderen Prüfungsbehörde vorgelegt.

(Ort, Datum) (Unterschrift)

This thesis is based on the following publications

Driven transport of soft Brownian particles through pore-like structures: Effective size method.
A. P. Antonov, A. Ryabov, P. Maass. J. Chem. Phys. **155**, 184102 (2021).

Collective excitations in jammed states: ultrafast defect propagation and finite-size scaling.
A. P. Antonov, D. Voráč, A. Ryabov, P. Maass. New J. Phys. **24**, 093020 (2022)

Solitons in overdamped Brownian dynamics
A. P. Antonov, A. Ryabov, P. Maass. Phys. Rev. Lett. **129**, 080601 (2022).

Brownian dynamics simulations of hard rods in external fields and with contact interactions
A. P. Antonov, S. Schweers, A. Ryabov, P. Maass. Phys. Rev. E **106**, 054606 (2022).

Other publications

Scaling laws for single-file diffusion of adhesive particles
S. Schweers, **A. P. Antonov**, A. Ryabov, P. Maass. Phys. Rev. E **107**, L042102 (2023).

Overcrowding induces fast colloidal solitons in a slowly rotating potential landscape
E. Cereceda-López, **A. P. Antonov**, A. Ryabov, P. Maass, P. Tierno, *to be published.*